AN INVESTIGATION OF THE STRUCTURE OF CERTAIN LIGHT NUCLEI USING NUCLEON TRANSFER REACTIONS.

By

Mohammed Khaliquzzaman.

Thesis presented for the degree
of Doctor of Philosophy at the University
of London.

Bedford College, London.

November, 1970.

CONTENTS

ABSTRACT

Studies on (d,d);(^{3}He,^{3}He);(d,^{3}He);(^{3}He,d) and (d,n) reactions are reported in this work. The (d,d) angular distributions were measured at an incident energy of 12.0 MeV on ^{45}Sc, ^{40}Ca and at 13.0 MeV on ^{37}Cl, ^{35}Cl, ^{27}Al and ^{23}Na. The (^{3}He,^{3}He) angular distributions were measured at an incident energy of 14.0 MeV on ^{29}Si and ^{25}Mg. The results of elastic scattering studies were analysed to extract optical potential parameters for the analysis of the transfer reaction experiments.

The (d,^{3}He) angular distributions were measured on targets ^{45}Sc, ^{40}Ca at an incident energy of 12.0 MeV and on ^{37}Cl, ^{35}Cl, ^{27}Al and ^{23}Na at 13.0 MeV. The (^{3}He,d) angular distributions were measured on targets of ^{29}Si and ^{25}Mg at an incident energy of 14.0 MeV. The reaction ^{29}Si(d,n)^{30}P was studied at 3.0 MeV. The results of transfer reaction studies were analysed using DWBA and Hauser-Feshbach theories and discussed in the light of the structure of the nuclear states involved. It has been possible in some cases to assign spins and parities to nuclear levels from these studies. Implications of reaction mechanism in some cases have also been considered. The problem of absolute normalization of DWBA calculations has been investigated using the results from some (d,^{3}He) studies.

ACKNOWLEDGEMENTS

I wish to express my gratitude and indebtedness to Dr. B.W. Hooton for his guidance and help in course of this work. The advice and help of Prof. H.O.W. Richardson throughout my association with the Bedford College is gratefully acknowledged. I wish to thank Mr. D.L. Allan for his supervision and help in the initial stages of this work. It is with sorrow that I recall the premature disability that struck Mr. Allan and wish that he may get back to active life again.

I would like to thank Mr. G.V. Ansell, Dr. J.M. Adams, Mr. B. H. Armitage, Dr. R. Chapman, Dr. C. Clements, Dr. J. Cookson, Dr. W.M. Currie, Dr. P.R. Evans, Dr. P.S. Fisher, Dr. O.N. Jarvis, Mr. M. Knobes, Mr. K.C. Knox, Dr. W.D.N. Pritchard, Miss E.M. Petty, Mr. J.L. Rose, Dr. G.T. Squire, Mr. R.N. Thomas, Mr. S. Waring, Dr. D. Wilmore, the accelerator crew, the staff of H.V. Lab., the scanners, the staff of the A.E.R.E. tracing office and the photographic group and my many friends for their help at various stages of the work.

Thanks are due to Dr. A.T.G. Ferguson, Dr. B. Rose and Dr. J.M. Freeman for providing all the facilities at A.E.R.E., Harwell for this work.

I would also like to thank Miss S.E. Cheswick for typing the manuscript.

CHAPTER I

GENERAL INTRODUCTION

It has been known for a long time that a large amount of information can be obtained about nuclear states by studying transfer reactions. By transfer reaction, a rearrangement collision is meant, in which a nucleon or a cluster of nucleons is directly transferred between two colliding nuclei in a one step process. Such a reaction takes place in time comparable to transit time of the incident particle ($\sim 10^{-23}$ sec) over the dimension of the target nucleus. The distinctive feature of such a reaction is that it shows very strong dependence on direction of emission of the reaction products.

By measuring the angular distributions of the reaction products angular momentum transfers can be deduced. Making use of the angular momentum selection rules information on the relative spins and parities of the nuclear states can be obtained. From the strength of the particular transition it is possible to extract the overlap between the initial and final states of the target nucleus. This is usually done in terms of spectroscopic factors which are defined as the reduced width amplitude for the transferred particle and are directly related to fractional parentage coefficients between the states. These spectroscopic factors

can be used to identify specific configurations of the nuclear states involved. Distorted wave Born approximation (DWBA) calculations are used to evaluate these factors.

It will be shown in later chapters that the differential cross-section for a direct reaction can be factorised in the form

$$\frac{d\sigma}{d\Omega} = R \sum_{j,\ell} S_{j,\ell}\, \sigma_{j,\ell}(\theta)$$

where different allowed values of spin and angular momentum contribute separately to the yield. The spectroscopic factors $S_{j,\ell}$ contain all the nuclear structure information and R is a statistical factor involving spin and iso-spin of the states involved. The reaction mechanism is associated with the term $\sigma_{j,\ell}(\theta)$ which contains the energy and angular dependence of the cross-section evaluated from the DWBA calculation.

In recent years due to the availability of large computing power, shell model calculations including many active nucleons outside the closed core have become feasible. These calculations have succeeded in yielding energy spectra of large number of nuclei in reasonable agreement with the experimental pictures. However, these agreements are only meaningful if the theoretical wave functions of the various levels are also an equivalently good approximation to the physical situation. This relationship between the shell model and actual nuclear wave functions is one of the main concerns of this work. Comparison of the experimental spectroscopic factors to the corresponding theoretical values provides an index of the extent to which the actual nuclear levels are constructed

according to the particular shell model prescription used.

Comparisons with the rotational model predictions have also been made in appropriate cases where there was any previous evidence of the applicability of this model.

The studies reported in this work are on the proton transfer reactions (d,^{3}He), (^{3}He,d) and (d,n). Some elastic scattering studies [(d,d) and (^{3}He, ^{3}He)] have also been reported which were conducted to evaluate the optical potential parameters for use in the DWBA calculations for the transfer reactions.

The scheme of presentation of the main body of information is as follows. In the 2nd chapter theoretical background and the problems associated with the various calculations performed in this work are reported. The 3rd chapter contains the descriptions of the various instrumentation systems and the accelerators used in the experiments. The experimental and data reduction procedures are reported in the 4th chapter. The elastic scattering, pick-up and stripping reaction studies are reported in the 5th, 6th and 7th chapters respectively. The conclusions from the studies are presented in each chapter.

CHAPTER II

2.1 Introduction

One very striking phenomena about nuclear reactions is the presence of a large number of viable competing theories. Some such theories give an exact formula for the scattering amplitude which can apply, in principle, to any reaction. However, in order to apply such a theory to practical cases, it is necessary to assign a central role to some particular physical mechanism. Once such an approximation has been introduced to the exact formula, the results are just good for those cases where this mechanism actually dominates.

Two extreme cases can be distinguished. Firstly, the case of sharp resonances, when we say a compound nucleus is formed and the Breit-Wigner resonances formula applies.

Secondly, the case of direct reactions, a transition takes place directly between initial and final states, which can typically be expressed by some sort of Born approximation. The cross-section varies slowly with energy.

However, this is not to say that they are the only two types of phenomena encountered. In recent years experiment has thrown up a

great variety and subtlety of phenomena which show features intermediate between these two extremes.

This work is mainly concerned with the direct reaction, hence a formalism of the direct reaction theory is included here. The DWBA calculations have been used extensively in this work for the extraction of spectroscopic factors as pointed out in the chapter I. Hence the problems associated with the DWBA calculations are reported in detail in this chapter. Also included in this chapter are some discussions on spectroscopic factors and their relation to the nuclear models.

2.2 Direct Reaction Theory

The direct reaction theory of nuclear reaction can be considered as an extension of the optical model. According to the optical model, the elastic scattering between two nuclei can be described by a complex potential well. The direct reaction theory accepts the optical model as a first approximation, but introduces as a perturbation an additional interaction which gives rise to the non-elastic processes. This additional interaction affects some simple internal degrees of freedom of one or two nuclei involved in the collision.

The simplest and most widely exploited type of internal degree of freedom, used in direct reaction theory, is the case when one nucleus is considered to be composed of two nuclides held together in a bound state by mutual attraction. The other nucleus is allowed to interact directly with one of these two sub-units to produce an inelastic scattering or a rearrangement collision. The process of stripping and pick-up are shown pictorially in figures 2.2.1.

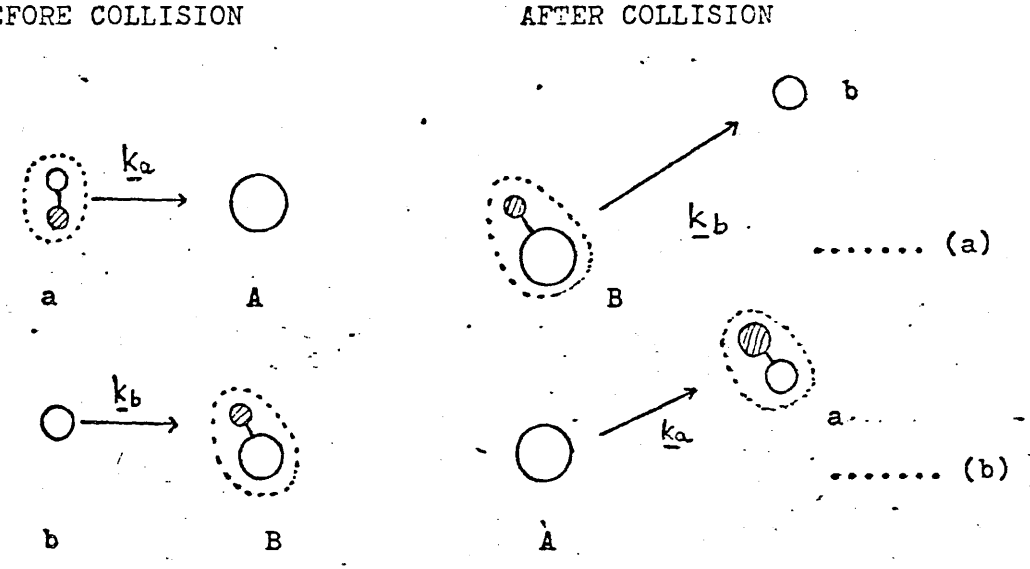

Fig 2.2.1 (a) Stripping A(a,b)B

(b) Pick-up B(b,a)A

This interaction is treated as a perturbation added to the optical potential, which acts between the centre of mass of the incident and the target nuclei. A more sophisticated model would be to regard the target nucleus as consisting of a core with several nucleons bound to it, the core resulting from all the nucleons in the closed shell and the nucleons bound to the core being the nucleons in the incomplete shell.

A third type of interaction which has been used, is the interaction of one nucleus with collective modes of motion of the other. This kind of interaction gives rise to inelastic scattering due to rotational and vibrational states.

Such simple picture of nuclear reaction process represents an over simplification of the true situation. However, this model has proved to be useful to the understanding of many structure problems and has become a very important tool of nuclear spectroscopy.

We give below a description of the formalism of distorted wave Born approximation (DWBA) theory which shows its salient features but not the details of evaluation of the cross-sections. The description is similar to that of Satchler [Sa 64].

The transition amplitude of reaction A(a,b)B can be written in the DW formalism as

$$T_{DW} = J \int d\underline{r}_a \int d\underline{r}_b \; \chi_b^{(-)}(\underline{k}_b, \underline{r}_b) \langle B,b | V | A,a \rangle \; \chi_a^{(+)}(\underline{k}_a, \underline{r}_a) \qquad (2.2.1)$$

Here $\underline{r}_a$ is the relative displacement of "a" from "A" and $\underline{r}_b$ the displacement of 'b' from 'B', where J is the Jacobian of the transformation to these relative coordinates. The functions χ_a and χ_b are the "distorted waves". They are elastic scattering wave functions which describe the relative motion of the pair "a,A" (asymptotically with momentum $\underline{k}_a$) before the collision or the pair "b,B" (with $\underline{k}_b$) after the collision. Asymptotically, the χ's have the form of a plane plus a scattered wave when there is no coulomb field present, χ's can be written as

$$\chi^{+}(\underline{k},\underline{r}) \rightarrow \exp(i\underline{k}\cdot\underline{r}) + f(\theta)\, e^{ikr}/r \qquad (2.2.2)$$

The superscript (+) or (−) denotes the usual out-going or in-going boundary condition, the two are related by time reversal which in the absence of spin has the form

$$\chi^{(+)}(-\underline{k},\underline{r}) = \chi^{(-)*}(\underline{k},\underline{r}) \qquad (2.2.3)$$

In the optical model approximation, the distorted waves are generated from a Schrödinger equation

$$\{\nabla^2 + k^2 - \frac{2\mu}{\hbar^2}\,[U(r) + U_c(r)]\}\,\chi(\underline{k},r) = 0 \qquad (2.2.4)$$

where $U(r)$ is the optical model potential, U_c the coulomb potential and μ is the reduced mass of the pair.

When the particles "a" and "b" have spin, a spin orbit potential is included in $U(r)$ in equation 2.2.4. The function χ then becomes a

matrix in spin space $\chi_{m',m}$ where m is the Z component of spin. Terms $m' \neq m$ allow the possibility of spin-flip during the elastic scattering. The time reversal relation 2.2.3 then becomes

$$\chi^{(-)*}_{m',m}(\underline{k},\underline{r}) = (-)^{m-m'} \chi^{(+)}_{-m',-m}(-\underline{k},\underline{r}) \qquad (2.2.5)$$

In similar way, coupling to the nuclear spin would make χ dependent upon spins also.

The remaining factor in the amplitude 2.2.1 is the matrix element of the interaction causing the non-elastic event, taken between the internal states of the colliding pairs,

$$\langle B,b|V|A,a\rangle = \int \psi^*_B \psi^*_b \; V \; \psi_A \psi_a \; d\xi \qquad (2.2.6)$$

where ξ represents all the coordinates independent of $\underline{r}_a$ and $\underline{r}_b$. This factor is a function of $\underline{r}_a$ and $\underline{r}_b$ and plays the role of an effective interaction between the elastic scattering states χ_a and χ_b. It contains all the information on nuclear structure, angular momentum selection rules and the type of reaction being considered.

This factorization of the integrand of amplitude 2.2.1 has great advantages. It makes it possible to treat the dynamics of elastic scattering while making use of very general (for example rotational) properties of the nuclear matrix elements 2.2.6. The "physics" of the reaction then appears in the magnitude and radial shape of this factor (i.e. eq. 2.2.6).

The matrix elements 2.2.6 can be expanded into terms which correspond to the transfer to the nucleus of a definite angular momentum J, which in turn is comprised of orbital part ℓ and a spin part S. If the particles 'a' and 'b' have spins 'S_a' and 'S_b', and the target and residual nuclear spins are J_A and J_B respectively, we define

$$j = J_B - J_A, \qquad S = S_a - S_b \qquad \ell = J - S \tag{2.2.7}$$

Very often only one value of ℓ, S and j is allowed or is important in a given transition. The multipole series expansion of 2.2.6 may be written with Clebsch-Gordan coefficient corresponding to the vector coupling of the quantities in (2.2.7) as

$$\langle J_B M_B, S_b m_b' | V | J_A M_A, S_a m_a \rangle = \sum i^{-\ell} G_{\ell s j, m}(\underline{Y}_a, \underline{Y}_b, bB, aA)$$

$$\times (-1)^{S_b - m_b} \langle J_A j M_A, M_B - M | j_B M_B \rangle \langle S_a S_b m_a, -m_b | S\ m_a - m_b \rangle$$

$$\times \langle \ell s m, m_a - m_b' | j M_B - M_A \rangle . \tag{2.2.8}$$

where $m = M_B - M_A + m_b - m_a$. The symbol "aA", "bB" as arguments of G denote dependence on the various nuclear quantum numbers (other than Z component of spin). The function G may be defined by the inverted form of expansion 2.2.8.

$$G_{\ell sj,m} = i^{\ell}\left(\frac{2\ell+1}{2j_B+1}\right)\sum \langle j_B M_B, S_b m_b | V | j_A M_A, S_a m_a\rangle$$

$$\times (-1)^{S_a - S_b} \langle j_A j M_A, M_B - M_A | j_B M_B\rangle \langle S_a S_b m_a - m_b | S\ m_a - m_b\rangle$$

$$\times \langle \ell s\ m,\ m_a - m_b | j\ M_B - M_A\rangle \qquad (2.2.9)$$

It is useful to write G as product of two factors

$$G_{\ell sj,m}(\underline{Y}_b, \underline{Y}_a) = A_{\ell sj}\, f_{\ell sj,m}(\underline{Y}_b, \underline{Y}_a) \qquad (2.2.10)$$

This separation into spectroscopic coefficient 'A' and a form factor 'f' is one of convenience, so that, for example, standard type of form factors with simple normalisation may be used in computation. It is natural to choose 'A' to include such quantities as fractional parentage coefficients for the initial or the final nuclear states and the interaction strength.

The amplitude 2.2.1 involves an integration over the space of both $\underline{Y}_a, \underline{Y}_b$ and the numerical evaluation of such a six dimensional integral is quite difficult. For this reason, the so called "zero range" approximation is often introduced. This zero range assumption has the physical meaning that the particle 'b' is emitted at the same point at which particle 'a' is absorbed, so that $\underline{Y}_b = \frac{A}{B}\underline{Y}_a$ (where A and B are the masses of the corresponding nuclei). The form factor 2.2.10 can then be written

$$f^{(zero)}_{\ell sj,m}(\underline{r}_b,\underline{r}_a) = \delta(\underline{r}_b - \frac{A}{B}\underline{r}_a) \int f_{\ell sj,m}(s + \frac{A}{B}\underline{r}_a,\underline{r}_a)\, ds$$

$$= F_{\ell sj}(r_a)\; Y^m_\ell(\theta_a\phi_a)\; \delta(\underline{r}_b - \frac{A}{B}\underline{r}_a) \qquad (2.2.11)$$

As a result, the amplitude 2.2.1 is reduced to a three-dimensional integral which is considerably easier to evaluate. Using expansion coefficient 2.2.8, the transition amplitude can be written as

$$T_{DW} \equiv \langle k_b, j_b M_B, S_b m_b | V | K_a, j_a M_A, S_a m_a \rangle$$

$$= J \sum_{m'_a\, m'_b} \int d\underline{r}_a \int d\underline{r}_b\; \chi^{(-)*}_{m'_b m_b}(\underline{K}_b,\underline{r}_b)\; \langle m'_B M_B | V | m'_a M_A \rangle\; \chi^{(+)}_{m'_a,m_a}(\underline{K}_a,\underline{r}_a)$$

$$= \sum_{\ell sj} (2j+1)^{\frac{1}{2}}\, A_{\ell sj}\, \langle J_A j M_A,\; M_B - M_A | S_B M_B \rangle\; \beta^{\ell m\; m_b S_b}_{S_j}(\underline{K}_b,\underline{K}_a) \qquad (2.2.12)$$

where $m = M_B - M_A + m_b - m_a$. The reduced amplitude β is given by

$$(2j+1)^{\frac{1}{2}}\, \beta^{\ell m\; m_b m_a}_{S_j}(\underline{K}_b,\underline{K}_a) = \sum_{m'_a\, m'_b\, m} \langle \ell s m', m'_a - m'_b \,|\, j\; m - m_b + m_a \rangle$$

$$\times \langle S_a S_b\; m'_a - m'_b \,|\, S\; m'_a - m'_b \rangle\; (-1)^{S_b - m'_b} \int d\underline{r}_a\; d\underline{r}_b$$

$$\times \chi^{(-)*}_{m'_b m_b}(\underline{K}_b,\underline{r}_b)\; f_{\ell sj,m'}(\underline{r}_b,\underline{r}_a)\; \chi^{(+)}_{m'_a,m_a}(\underline{K}_a,\underline{r}_a) \qquad (2.2.13)$$

In the absence of spin orbit coupling, the $\chi_{m,m'}$ becomes diagonal in and independent of the spin components $m \neq m'$. The spin dependence of the reduced amplitude may then be factorised out as

$$(2j+1)^{\frac{1}{2}} \beta_{Sj}^{\ell m\ m_b\ m_a} (\text{No S.O.}) = \langle \ell s m, m_a - m_b | j m - m_b + m_a \rangle .$$

$$\times \langle s_a s_b\ m_a - m_b | S\ m_a - m_b \rangle \times (-1)^{S_a - m_b} (2\ell+1)^{\frac{1}{2}} \beta_{Sj}^{\ell m} \qquad (2.2.14)$$

where now

$$(2\ell+1)\ i^{\ell} \beta_{Sj}^{\ell m} = \int d\underline{\nu}_a \int d\underline{\nu}_b\ \chi_b^{(-)*}(\underline{K}_b, \underline{\nu}_b)$$

$$\times f_{\ell s j, m}(\underline{\nu}_b, \underline{\nu}_a)\ \chi_a^{(+)}(K_a, \nu_a) \qquad (2.2.15)$$

This β will depend upon 'S' and 'j' if the form of 'f' depends upon those quantum numbers.

The differential cross-section for the unpolarised projectiles and unpolarised target nuclei is given by

$$\frac{d\sigma}{d\Omega} = \frac{\mu_a \mu_b}{(2\pi\hbar^2)^2} \frac{K_a}{K_b} \frac{\Sigma |T|^2}{(2j_A+1)(2S_a+1)} \qquad (2.2.16)$$

where μ_a and μ_b are the reduced masses of the respective particles, the sum is over M_A, m_a, M_B, m_b. In terms of reduced amplitude 2.2.13, this becomes

$$\frac{d\sigma}{d\Omega} = \frac{\mu_a\mu_b}{(2\pi\hbar^2)^2} \quad \frac{K_b}{K_a} \quad \frac{2j_B+1}{(2j_A+1)(2S_a+1)} \sum_{jm} \Big| \sum_{\ell s \atop m_b m_a} A_{\ell sj} \beta_{Sj}^{\ell m\, m_b m_a} \Big|^2 \tag{2.2.17}$$

we note that sum over M_A and M_B has made different j values incoherent, but interference between different s and ℓ remains. If only one value of s and ℓ are important or allowed, equation 2.2.17 may be written

$$\frac{d\sigma}{d\Omega} = \frac{2j_B+1}{2j_A+1} \sum_{J} \frac{|A_{\ell sj}|^2}{2S_a+1} \sigma_{\ell sj}(\theta) \tag{2.2.18}$$

where the reduced cross-section is

$$\sigma_{\ell sj}(\theta) = \frac{\mu_a\mu_b}{(2\pi\hbar^2)^2} \quad \frac{K_b}{K_a} \sum_{m\, m_b m_a} |\beta_{Sj}^{\ell m\, m_b m_a}|^2 \tag{2.2.19}$$

When there is no spin-orbit coupling, we use equation 2.2.14 to obtain

$$\frac{d\sigma}{d\Omega}(\text{No S.O.}) = \frac{2j_B+1}{2j_A+1} \sum_{\ell sj} \frac{|A_{\ell sj}|^2}{2S_a+1} \sigma_{\ell sj}(\text{No S.O.}) \tag{2.2.20}$$

where the reduced cross-section now becomes

$$\sigma_{\ell sj}(\text{No S.O.}) = \frac{\mu_a\mu_b}{2j_A+1} \quad \frac{K_b}{K_a} \sum_{m} |\beta_{Sj}^{\ell m}|^2 \tag{2.2.21}$$

In this case, the free sum over m_a and m_b has made, ℓ and s sum incoherent as well. In the next section we shall see explicitly the different quantities in the general formalism outlined above as applied to the reactions reported in this work.

2.3 The (^{3}He,d) (d,^{3}He) reactions and DWBA

In this section special considerations are given to some of the factors in the general formulation of the previous section as applied to the reactions (^{3}He, d) and (d,^{3}He). Figure 2.3.1 shows schematically the situation in the case of A(d,^{3}He)B.

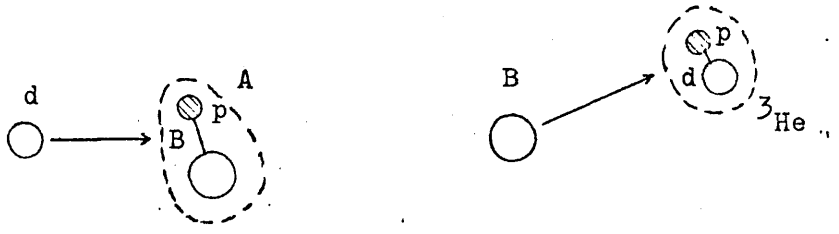

Fig. 2.3.1 Schematic diagram of reaction A(d,^{3}He)B

The hamiltonian of the system can be written as

$$H = T_{B,P} + T_{d,A} + V_{d,B} + V_{B,P} + V_{d,p} \qquad (2.3.1a)$$

$$= T_{B,\,^3He} + T_{d,p} + V_{d,p} + V_{B,p} + V_{B,d} \qquad (2.3.1b)$$

The initial and final state hamiltonians are

$$H_I = T_{d,A} + T_{B,p} + V_{B,p} \qquad (2.3.2)$$

$$H_F = T_{B,\,^3He} + T_{d,p} + V_{d,p} \qquad (2.3.3)$$

So the interaction potential which produces the reaction using prior interaction form would be

$$V = H - H_I - V_{OPT}$$
$$= V_{d,p} + V_{d,B} - V_{OPT} \qquad (2.3.4)$$

where V_{OPT} is the optical potential chosen to describe elastic scattering in the 'd+A' system. Arguing that V_{dB} and V_{OPT} cancell each other, the interaction potential becomes $V_{d,p}$. This approximation seems reasonable enough physically.

With this approximation the nuclear matrix element can be written as

$$\langle B\ {}^3He | V_{dp} | d, A \rangle = \langle B | A \rangle \ \langle {}^3He\ | V_{d,p} | d \rangle \qquad (2.3.5)$$

The first term will be taken up in the section on bound state wave functions and will be shown to be concerned with spectroscopic factors. The second can be written in the form

$$\langle d | V_{d,p} | {}^3He \rangle = \nu^{\frac{1}{2}} C \int d\rho\ \phi_d(\rho)\ V_{dp}\ \phi_{{}^3He}\ (\gamma, \rho)$$
$$= \nu^{\frac{1}{2}} C\ \ D(\gamma) \qquad (2.3.6)$$

where ρ is the internal coordinate of the deuteron and γ is the coordinate of the nucleon relative to deuteron centre of mass. The factor ν arises from anti-symmetrization and is equal to the number of equivalent nucleons

in the three nucleon system, and C is the coefficient of fractional parentage. For decomposition of three nucleon system into triplet deuteron and captured nucleon, the product, $\nu^{\frac{1}{2}}C = \sqrt{\frac{3}{2}}$. It is convenient to factor the integral in 2.3.6 into an amplitude D_o and a range function $f(\gamma)$ with

$$D_o = \int d\gamma \int d\rho \; \phi_d(\rho) \; V_{dx} \; \phi(\gamma,\rho) \qquad (2.3.7)$$

and

$$f(\gamma) = \frac{1}{D_o} \int d\rho \; \phi_d(\rho) \; V_{dx} \; \phi(\gamma,\rho) \qquad (2.3.8)$$

In the zero-range approximation the range function $f(\gamma)$ is taken as a delta function

$$f(\gamma) = \delta(\gamma) \qquad (2.3.9)$$

The zero-range distorted wave cross-section is proportional to 'N' defined as

$$N = \frac{3}{2} \left[\frac{D_o^2}{1.08} \times 10^{-4} \right] \qquad (2.3.10)$$

where D_o is in MeV fm^3.

With this definition of 'N' the differential cross-section for the (^{3}He,d) becomes [Hi 67]

$$\frac{d\sigma_{\ell j}}{d\Omega}\,(^3\mathrm{He},d) = N\left[\frac{2J_f+1}{2J_i+1}\right] C^2S(\ell,j)\;\sigma_{\ell j}(\theta) \qquad (2.3.11)$$

For the inverse reaction one obtains

$$\frac{d\sigma_{\ell j}}{d\Omega}\,(d,\,^3\mathrm{He}) = \frac{2}{3}\,N\,C^2\,S(\ell,j)\;\sigma_{\ell j}\,(\theta) \qquad (2.3.12)$$

where $S(\ell j)$ is the usual spectroscopic factor. 'C' is the isospin Clebsch-Gordan coefficient

$$C = \langle T_B\tfrac{1}{2},\ M-m\ m \,|T_AM\rangle$$

where $M = \frac{1}{2}(N-Z)$ of the target, $m = -\frac{1}{2}$. The reduced cross-section $\sigma_{\ell j}(\theta)$ has already been defined in the equation 2.2.9. The normalization constant has been defined here in such a way [by the inclusion of $\frac{2}{3}$ in the case of $(d,^3\mathrm{He})$] that it is the same for both the $(d,^3\mathrm{He})$ and $(^3\mathrm{He},\,d)$ reactions.

The normalization- constant 'N' has been evaluated both theoretically and experimentally on a number of occasions. There is considerable scatter on the values quoted. The value of 4.42 evaluated by Bassel [Ba66] has been widely used.

One of the aims of this work, in the study of some of the $(d,^3\mathrm{He})$ reactions has been to investigate this variation in 'N'. The problem concerning the variation in 'N' is considered in detail in chapter VI where $(d,^3\mathrm{He})$ work is reported.

The DWBA calculations reported in this work were performed by using the University of Colorado spin orbit version of the programme DWAKE modified to run on the Harwell IBM 360/75 computer (c.f. appendix B).

The calculations were performed in the zero range approximation using local potentials only, because the net effect of non-locality of nuclear potential and the finite range approximation in the DWBA calculations is to increase the magnitude of the cross sections [Hi67]. This is equivalent to a decrease in the value of 'N' and hence is of no consequence in the extraction of the relative spectroscopic factors.

2.4 Bound State Wave Functions and DWBA

In the formulation for direct reaction A(a,b)B where one nucleon is transferred to or from target nucleus, the transition amplitude contains as a factor the overlap of the initial and the final nuclear wave functions (i.e. equation 2.3.5). This factor can be written as

$$\langle \psi_B | \psi_A \rangle = \int \psi_B^* (\xi, x)\ \psi_A(\xi) d\xi$$

$$= \sum_{jm} \langle j_A\ j\ M_A\ m | j_B M_B \rangle\ \phi_{jm}^{BA*}(x) \qquad (2.4.1)$$

In equation 2.4.1 an expansion into states of definite total angular momentum J has been done, $\underline{J}_A$ and $\underline{J}_B$ are the spins of the target and residual nuclei respectively; M_A and M_B are their Z-projections. Clebsch-Gordan coefficients take care of the angular momentum coupling. If the iso-spin formalism is used 2.4.1 will also contain an iso-spin C-G coefficient. The symbol ξ stands for internal coordinates of the

target nucleus, while x stands for spatial, spin and iso-spin coordinates of the captured nucleon. Defined in this way, in general ϕ is not normalised to unity even if ψ_A and ψ_B are. Since ϕ^{BA}_{jm} is a function of the transferred nucleon coordinates alone, it is frequently referred to as the wave function of the captured (picked-up) particle.

The question now arises how do we specify this form factor ϕ? It can be expanded in terms of the 'Shell Model' single particle orbital $\psi_{n\ell j}(x)$ i.e. eigenstates of some single particle potential well. The orbital angular momentum ℓ is restricted to one of the values $\ell=j\pm\frac{1}{2}$ according to the parity change in the transition, since

$$\tau_{BA} = (-1)^{\ell} \qquad (2.4.2)$$

The expansion then is over principal quantum number n and of course continuum states if the well chosen is of finite depth. We would like to think that only one such term is important and it is on this basis that most of the distorted wave calculations of stripping have been made. This approach is very reasonable for closed shell targets. If there is negligible rearrangement of the closed shell case when extra nucleon is added, then equation 2.4.1 defines the shell model single particle wave function. This alone is not of course, sufficient to determine the shell model potential well of which it is an eigenfunction. However we can be guided by optical model analyses of nucleon elastic scattering from the targets and assume that the bound nucleons move in a potential well similar shape with same radius and surface diffuseness.

We then adjust the depth of the well to give binding energy equal to the observed separation energy of the nucleon. One of the properties of the form factor ϕ in equation 2.4.1 of which we are certain is that, asymptotically, it must decrease exponentially as exp $(-Kr)$ with decay length K^{-1} determined by the separation energy ε,

$$\varepsilon_{BA} = E_B - E_A \qquad (2.4.3)$$

$$K^2 = 2M\varepsilon(B,A)/\hbar^2 \qquad (2.4.4)$$

so the usual prescription is to generate ϕ as an eigen function in a potential well with a binding energy equal to separation energy which leads to the correct asymptotic form of tail (but not necessarily with correct normalisation). This prescription is known as the separation energy procedure. But we do not know where and how to match this tail on the model ϕ which we are using in the nuclear interior. This ambiguous transition occurs at surface region from where the most important contribution to stripping comes.

Two aspects of these uncertainties in ϕ may be distinguished. They are shape and magnitude of ϕ in the surface region. The shape of ϕ affects the shape of the stripping angular distribution, because it determines the relative weight with which various partial waves contribute. The dependence is not strong provided the tail falls exponentially with decay, which does not violate equation 2.4.3 and 2.4.4. too violently.

The magnitude of the stripping cross-section is roughly proportional to the value of $|\phi|^2$ in the surface region, (other things being equal) since the usual interpretation of ϕ is as the product of a normalised single particle wave function times a spectroscopic amplitude [Fr60],

$$\phi_{jm}(x) = S^{\frac{1}{2}}(i,j)\ \psi_{n\ell jm}(x) \qquad (2.4.5)$$

It is clear that values of S extracted from experiments depend sensitively upon the model chosen for ψ.

An example of the difficulties which arise with more complicated configurations has been given by Pinkston [Pi65]. It is the case of the addition of a further nucleon to a closed shell plus one nucleon nucleus. If in the shell model sense, it enters the same orbit as the extra closed-shell nucleon of the target, the resulting configuration can form states of spin J_B ranging from 0 to 2j. These will have different energies, that is to say, the separation energy for removing an additional nucleon from B, leaving the target nucleus A in its ground state, depends upon J_B. On the other hand the shell model picture leads us to think of the second nucleon 'in the same orbit', that is, having the same wave function as the first one, irrespective of J_B. The discrepancy, of course, is due to the residual interaction between the two nucleons and to the use of two pictures which take account of this in different orders. Indeed, the usual shell model calculations ignore the effect of this interaction on the radial wave function of the two nucleons, but take account of its effect on their total energy and its dependence on J_B.

Stripping predictions from the separation energy procedure has, in some cases [Sh64, Yn63, Il62], led to results differing strongly from those expected from shell model consideration. This has led to an alternative prescription [Sh64, Yn63, Il62] of fixing well depth so as to give a binding energy equal to the zero-order (or Hartree-Fock) single particle energy for that orbit, irrespective of separation energy. The discrepancies just mentioned then seem to be largely removed. On the other hand there are cases where this second prescription does not seem to give results as good as the first [Bj64].

Recently Prakash [Pr68] has examined the problem of the relationship between different types of form factors. The form factor $\phi_j^{BA}(x)$ in presence of extra core nucleons with residual interactions satisfies the equation

$$[\varepsilon_{BA} - T - U_j^c(x)]\ \phi_j^{BA}(x) = P^{BA}(x) \qquad (2.4.6)$$

where

$$T = \frac{\hbar^2}{2m\ x^2} \left[-\frac{d}{dx}\left(x^2 \frac{d}{dx}\right) + \ell(\ell+1) \right]$$

and

$$P^{BA}(x) = \int\int d\xi'\, dx \left\{ \psi_A(\xi')\, y_i(x) \right\}_{J_B M_B} \times \sum_{i\,=\,\xi'} V_{xi}\ \psi_B(\xi', x)$$

where ξ' stands for coordinates of the extra core nucleons. $U_j^c(x)$ is the effective central field as explained by Prakash and Austern (Pr69). Other quantities have been defined in context of equation 2.4.1.

Equation 2.4.6 can be re-written as

$$[\varepsilon_{BA} - T - U_j^C(x) - U^P(x)] \quad \phi_j^{BA}(x) = 0 \qquad (2.4.7)$$

where $$U^P(x) = \frac{P^{BA}(x)}{\phi^{BA}(x)}$$

is the pseudo-potential whose addition to $U_j^C(x)$ would imitate the effect of the inhomogeneous term $P^{BA}(x)$. Agreement or otherwise of the solutions from equation 2.4.7 with the separation energy procedure depends on the shape of $U^P(x)$ because this prescription assumes that the effect of the inhomogeneous term $P^{BA}(x)$ is to add a pseudo-potential that only alters the depth of $U_J^C(x)$ without altering the Saxon-Wood shape.

So, in principle one can dispense with the empirical prescriptions by solving equation 2.4.6. As this can not be done with the computer programmes available to us, we shall continue to use different empirical prescriptions. The procedure adopted and consequent effects will be pointed out in each case under consideration.

2.5 Elastic Scattering, Optical Potential and DWBA

Elastic scattering of nucleons and various light nuclei from a great number of targets have been studied in great detail in the last decade. It has become customary to analyse elastic scattering data in terms of an optical model.

Optical model analysis is relevant to nuclear structure for two main reasons. Firstly, the optical model potential is simply the shell model potential extended into region of positive energy, and secondly,

knowledge of the optical potential is needed to extract information on the nuclear structure from the direct reaction measurements.

The most frequently used phenomenological optical potential has the form

$$V(\gamma) = V_c(\gamma) + Uf(\gamma) + iWg(\gamma) + U_s h(\gamma)\ \underline{\ell}.\underline{S} \qquad (2.5.1)$$

where V_c is the coulomb potential, U and W are the real and imaginary depths of nuclear central potential, U_s is the spin-orbit potential depth, $f(\gamma)$, $g(\gamma)$ and $h(\gamma)$ their respective form factors, and $\underline{\ell}.\underline{S}$ the spin-orbit operator. There is little phenomenological evidence for an imaginary part of the spin orbit potential so it is usually considered to be absent.

It is a sufficiently good approximation to assume that the charge of the incident nucleon or nuclei is concentrated at a point and nuclear charge is uniformly distributed throughout a sphere of radius R. This gives

$$V_c(\gamma) = \begin{cases} \frac{Zze^2}{2R}\left(3 - \frac{\gamma^2}{R^2}\right) & \text{for } \gamma < R \\ \frac{Zze^2}{\gamma} & \text{for } \gamma > R \end{cases} \qquad (2.5.2)$$

It turns out, however, that the calculated cross-section are very insensitive to the details of the coulomb potential.

The form factor $f(\gamma)$ is generally taken to be Woods-Saxon type

$$f(\gamma) = \frac{1}{1 + \exp\left(\frac{\gamma - R}{a}\right)} \qquad (2.5.3)$$

In this expression R is the radial distance at which $f(\gamma)$ has approximately half its maximum value and also its greatest rate of change. It thus corresponds approximately to the region where nuclear density is likewise falling rapidly and so is referred to as the nuclear radius. The quantity $R = \gamma_0 A^{\frac{1}{3}}$ where A is the mass number and $\gamma_0 \simeq 1.3f$.

The parameter 'a' determines the rate at which the function $f(\gamma)$ falls from its maximum value to zero. If it is small the function falls off sharply around $\gamma=R$ while if it is large, the fall is gradual. It is thus convenient to refer to it as the surface diffuseness parameter and has a value around .5 to 1f. Theoretical arguments [Ho66] suggest that imaginary part of the potential is predominantly peaked in the region of nuclear surface at low energies and progressively spreads through out the nuclear interior as energy increases. The required surface peaking and exponential fall-off can be obtained by allowing $g(\gamma)$ to have the form of the radial derivative $f(\gamma)$ normalised so that $g(R) = 1$. Thus the surface absorbing potential

$$g(\gamma) = \frac{4 \exp[(\gamma - R)/a]}{\{1 + \exp[(\gamma - R)/a]\}^2} \qquad (2.5.4)$$

A Gaussian function peaked at surface given by

$$g_G(\gamma) = \exp \left\{ - \left(\frac{\gamma - R}{a} \right)^2 \right\} \qquad (2.5.5)$$

has also some times been used for $g(\gamma)$.

It is however found that the calculated cross-sections are very insensitive to the form chosen for $g(\gamma)$, providing that in each case all the variable parameters are optimised and indeed many successful calculations have been made using the same Saxon-Woods form for $g(\gamma)$ as $f(\gamma)$. Conversely, this implies that analyses of experimental data can not be used to determine the form of the imaginary part of the potential. The spin dependent terms in the optical potential, arise from the spin orbit and tensor forces in nucleon-nucleon interaction. The spin orbit form factor $h(\gamma)$ has been found to have the Thomas form,

$$h(\gamma) = \frac{1}{\gamma} \frac{df(\gamma)}{d\gamma} \qquad (2.5.6)$$

Deuteron Optical Potential

A great number of studies and reviews have been published about the deuteron optical potential [Ho66, Di65, Ha64]. It has been found that there is a series of depths for the real potential [Ho66, El65] which can be used to fit the elastic scattering angular distribution data. If the wave functions corresponding to different depths of the potential are examined, it is found that for a given partial wave they all have the same asymptotic form and hence the same phase shift, so that they can not be separated by further measurements. They differ in that, the wave function corresponding to each potential, in the series, has

one half wave more inside the nucleus than the next shallow potential [Pe63].

Theoretical considerations [Ro65, Ab66] indicate that to first order the physically appropriate potential is that obtained by adding the contribution from each nucleon. This is indeed what is to be expected since the binding energy of deuteron is very small compared to the nuclear potential.

The deuteron optical potentials show only a few rather ill defined systematic variations and the deviations from them do not correlate with any obvious feature of nuclear structure.

It has been found that the differential cross-section is usually insensitive to the presence of spin dependent terms in the optical potential. The analysis of such data can not be used at all to extract potential depth reliably. It is thus preferable to use a central potential only.

As pointed out earlier, elastic scattering data is determined by the asymptotic form of the wave function. Nuclear reactions involving deuterons depend however on matrix elements that are essentially overlap integrals of the deuteron wave functions, an interaction potential, and the wave function of the other particle involved in the reaction. This integral is evaluated through out the nuclear volume and is therefore sensitive to the deuteron wave function in the interior of the nucleus. This introduces uncertainty in the spectroscopic factors calculated. Effects arising from this source will be pointed out in relevant places.

^{3}He Optical potentials

A review of ^{3}He (helion) optical potential has recently been conducted by Hodgson [HO68]. It has been found, as in the case of deuteron, that a series of potentials are capable of explaining elastic scattering data. To first order, the physically appropriate potential is obtained by adding the three contributing nucleon potentials [Ro65,Ab66]. As pointed out before in deuteron case, this is to be expected since the binding energy of helion is small compared with depth of the nuclear potential.

A few studies of the variation [Gi67, Ha67] of the potential with ^{3}He energy have been made for selected nuclei. The results for ^{3}He scattered by ^{40}Ca and ^{58}Ni show very small variations [Gi67].

Study conducted by Hibert et al. [Hi67] for ^{15}N and ^{39}K with a series of potentials in the DWBA for the (d,^{3}He) reaction show that the shape of angular distribution is unaffected for $\theta < 50^{o}$. However the magnitude of the cross-section has been found to be affected. As in the case of deuteron potential, effects from this source will be discussed in relevant cases.

There has been little evidence for the importance of spin orbit potential in ^{3}He optical potential [Hi67,Ho68]. So, in all our calculations a spin orbit potential was not included.

2.6 The Coefficients of Fractional Parentage and the Spectroscopic Factors.

In this section only the relationship between the coefficients of fractional parentage (cfp) and the spectroscopic factors are shown, and no explicit considerations are given to the shell model or the

schemes of angular momentum coupling apart from a few comments.

The antisymmetrised N-nucleon wave function can be expanded in terms of the states of the first (N-1) particles, the n-th particle being vector coupled to these states. Using thedirect product notation of French and MacFarlane [Fr60] we have

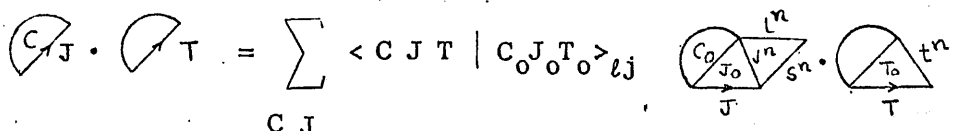

$$= \sum_{\substack{C_o J_o \\ \ell j}} < C\ J\ T \mid C_o J_o T_o >_{\ell j}$$

(2.6.1)

$$= \sum_{\substack{C_o J_o \\ \ell j Z}} (-1)^{Z+S-j-T} < C\ J\ T \mid C_o J_o T_o >_{\ell j} U(J_o S\ J\ell : Z j)_{\ell j} \times$$

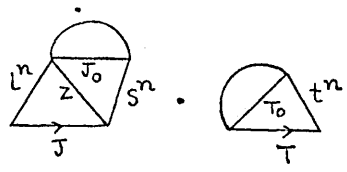

(2.6.2)

If only identical particles are involved or neutrons and protons are antisymmetrised separately, the iso-spins may be ignored. On the left hand side of the equation 2.6.1 the symbol 'C' stands for all the quantum numbers, apart from J and T and their Z-components, necessary to define the state. For example 'C' might define a shell model configuration along with L-S coupling shell model states or it might define the so called seniority or symplectic symmetry if the system is a pure JJ state. Or if the state is not simply described in terms

of some well known scheme, 'C' might stand for an entire set of expansion coefficients giving the state in terms of a complete set. The symbol 'C_o' on the right hand side of equation 2.6.1 does the same thing for the (N-1) particle states. On the RHS the particle numbered 'n' has been separated out and its ℓ,S($=\frac{1}{2}$) and J are specified and of course also the radial quantum number or other such necessary information is to be understood. Each term in the expansion is anti-symmetric in particles 1,2,.....(N-1) but not in general in all 'N' particles, though the sum is. The quantity $\langle C\ J\ T | C_o J_o T_o \rangle_{\ell j}$ is a generalised coefficient of fractional parentage connecting states (CJT) and $(C_o J_o T_o)$. The ℓ value is determined by the parity and the J value.

It is convenient to change from the representation in equation 2.6.1 to that given in equation 2.6.2 using recoupling technique of angular momenta. The spectroscopic factor 'S' for orbitals angular momentum ℓ and channel spin Z is given by

$$S^{\frac{1}{2}}(\ell,Z) = N^{\frac{1}{2}} \sum_{j} (-1)^{Z-S-j-J} U(J_o S\ j\ \ell : ZJ) \langle C\ J\ T | C_o J_o T_o \rangle \qquad (2.6.3)$$

Summing over the channel spin and using the unitarity property of the 'U' function, it can be shown that the interference between different J vanishes and the spectroscopic factor becomes

$$S(\ell) = N \sum_{j} \langle C\ J\ T | C_o J_o T_o \rangle^2_{\ell j} \qquad (2.6.4)$$

The factor 'N' occurs because cfp describes the separation of particle n where as the reaction allows every particle to be emitted on the same footing but of course with no interference.

Usual shell model calculations yield the cfp which can be used to evaluate the spectroscopic factors. The model calculations vary in complexity depending on the numbers of active nucleons considered outside the closed shells. The comparison of the experimental spectroscopic factors with calculated values from the shell model gives an index of the correctness or otherwise of the shell model wave functions from a particular calculation. In the later case the comparison provides guide to future extension of calculations by indicating where and how the existing model begins to fail.

2.7 Rotational Model and Spectroscopic Factors

In the rotational model, the wave function of the nucleus is expressed as a product of a function ϕ, describing the vibration of the nucleus, the function $D^{I}_{M}(\alpha\ \beta\ \gamma)$ describing the rotation of the nucleus, and of the function χ_{Ω}, describing the internal motion in a deformed, axially symmetric potential,

$$\psi(IMK\ \Omega) = \left(\frac{2I+1}{16\pi^2}\right)^{\frac{1}{2}} \phi \left\{ \chi_{\Omega} D^{I}_{MK} + (-)^{I-J} \chi_{-\Omega} D^{I}_{-KM} \right\} \qquad (2.7.1)$$

The internal wave functions χ_{Ω} is the antisymmetrised product of single particle wave function $\chi_{\Omega\omega\alpha}$, with the projection of angular momentum vector on the symmetry axis Ω, the parity ω and the energy α as good quantum numbers.

According to Nilsson [Ni55] the functions $\chi_{\Omega\omega\alpha}$ are the solutions to the Hamiltonian

$$H = H_o + CL.S + D\ell^2 \qquad (2.7.2)$$

with

$$H_o = \tfrac{1}{2}\hbar\omega_o\,(-\Delta + r^2) - \delta\hbar\omega_o^4/3\,(\tfrac{\pi}{3})^{\frac{1}{2}}\,r^2\,Y_{2o} \qquad (2.7.3)$$

The deformation of the potential is expressed here with parameter δ, but more often given in terms of parameter η, which is related to δ as:

$$\eta = \frac{\delta}{K}\,\frac{\omega_o}{\omega_o^o} = \frac{\delta}{K}\,(1 - \tfrac{4}{3}\,\delta^2 - \tfrac{16}{27}\,\delta^3)\,\tfrac{1}{6} \qquad (2.7.4)$$

where $K = \tfrac{1}{2}(C/\hbar\omega_o^o)$ and $\omega_o^o = \omega_o(\delta = 0)$. The numerical value of K, adopted by Nilsson was 0.05.

The functions $\chi_{\Omega\omega\alpha}$ are expressible in terms of wave functions of a spherical potential, $\phi_{NLj\Omega}$

$$\chi_{\Omega\omega\alpha} = \sum_{N\ell j} C_{NLj}\;\phi_{NLj\Omega} \qquad (2.7.5)$$

The summation refers actually only to different orbitals ℓ,j of the same shell (N=constant), since the model neglects the interaction between different shells. The coefficient $C_{NLj}\,(\Omega\omega\alpha)$ are related to

coefficient $A_{NL\Lambda}$, tabulated by Nilsson as

$$C_{NLj}\ (\Omega\omega\alpha) = \sum_{\Lambda} A_{NL\Lambda} \cdot \langle \ell\ \tfrac{1}{2}\ \Lambda L \,|\, j\ \Omega \rangle \qquad (2.7.6)$$

The coefficients $C^2_{NLj}(\Omega\omega\alpha)$ obey the following sum rules

$$\sum_{NLj} C^2_{NLj}\ (\Omega\omega\alpha) = 1$$
$$\Omega\omega\alpha = \text{const.} \qquad (2.7.7)$$

and

$$\sum_{\Omega\omega\alpha} C^2_{NLj}\ (\Omega\omega\alpha) = 2j+1$$
$$NLj = \text{const.} \qquad (2.7.8)$$

In the first case the summation refer to all orbits ℓ,j of particular state N that contribute to certain level $\Omega\omega\alpha$, while in the second it refers to all levels $\Omega\omega\alpha$ that receive some contribution from the unperturbed orbit NLj.

As derived by Satchler [Sa58] the spectroscopic factor expressing the overlap between initial and final nucleus of a stripping reaction is

$$S^{(+)} = g^2\ \frac{2I_i+1}{2I_f+1}\ \langle I_i j\ K\Omega \,|\, I_f K_f \rangle^2\ \langle \phi_f \,|\, \phi_i \rangle^2\ C^2_{NLj}(\Omega\omega\alpha) \qquad (2.7.9)$$

where the quantities with subscript 'i' refer to initial nucleus and those without subscript to transferred particle. The coefficient $g^2=2$, if either $K_i=0$ or $K_f = 0$ and $g^2=1$ otherwise. Another special case where $g^2=2$ is the case of odd-odd of nuclei with $\Omega_1=\Omega_2$, and parallel coupling. 'j' is the angular momentum of the transferred particle. For pick up

$$S^{(-)} = g^2 \quad \frac{2I_f+1}{2I_i+1} \quad \langle I_f j \; K_f \Omega \; | I_i \; K_i \rangle \langle \phi_i | \phi_f \rangle C^2_{NLj}(\Omega\omega\alpha)$$

(2.7.10)

where the quantities have meaning mentioned earlier. The core overlap $\langle \phi_i | \phi_f \rangle$ of the initial and the final nucleus is normally taken to be unity. In calculating the spectroscopic factors from the rotational model quoted in this work the core overlap was assumed to be unity throughout. An incomplete overlap tends to decrease the spectroscopic factors. The values of the '$C_{N\ell j}$' coefficients used in calculations reported here were taken from the tabulation by Chi [Ch66].

CHAPTER III

INSTRUMENTATION

3.1 Introduction

Several distinct types of instrumentation systems have been used in the experiments reported within this work. They are:

1) particle identification system with semiconductor detectors,
2) particle identification system with Buechner magnetic spectrograph using position sensitive detectors,
3) multigap magnetic spectrograph with nuclear emulsion plates
4) time of flight neutron spectrometer with scintillation counters.

The particle identification system using a semiconductor counter telescope, its cooling system and special electronics were designed by the author. The other systems were available as standard Harwell facilities.

In the following sections the instrumentation systems are described in some detail. Brief descriptions of the acclerators used i.e. the Tandem and IBIS Van-de-Graaff are also included.

3.2 Particle Identification

Measurements of the spectra of particles emitted in nuclear reactions constitute one of the principle methods of nuclear spectroscopy. In energy ranges available from machines like the Tandem-Van-de-Graaff, nuclear reactions in general lead to a very many different channels. For example bombardment of ^{27}Al by deuterons (say at 13 MeV) leads to elastic and inelastic scattering, (d,p), (d,^{3}He), (d,alpha) and (d,n) reaction channels. Since the final nucleus can be produced in a series of excited states, the energy of the outgoing particles in each case will have a series of values determined by the levels in the final nucleus. In addition there will be particle groups from impurity and contaminants in the target, specially ^{12}C and ^{16}O.

Interpretation of the energy spectra in such cases is virtually impossible. Peaks due to lower yield reactions may not even be discernible from the back-ground. Unless some means of identification and separation of different particle groups can be achieved, propsects of studying reactions other than elastic scattering and a few specially favoured cases are quite hopeless.

Two types of particle identification systems were used for our experiments; (1) a system made of semiconductor detectors and (2) a system using a magnetic spectrograph. Both systems have advantages and disadvantages. They were used in a complementary way to get maximum advantage.

3.3 Particle Identification with Semiconductor Detectors

Introduction

The semiconductor particle identification systems are based on the fact that different kinds of particles of the same energy loose energy in absorbers at different rates. A thin transmission particle detector (ΔE detector) placed in front of a thick detector (E-detector) allows simultaneous determination of rate of energy loss (signal in ΔE detector) and total energy (signal in ΔE and E detectors added together), for particles passing into counter system. If a suitable calculation using the two signals is carried out it is possible in principle to determine what type of particle has been registered. Early systems based on this concept used scintillation detectors or gas chambers. But with the availability of suitable silicon semiconductor detectors the resolution and energy range of such systems have been tremendously improved and extended.

To achieve its maximum usefulness a particle identifier must produce an output signal whose amplitude determines the type of particle with no ambiguity even though several types of particles each covering a wider range of energies may pass through the counter system. Thus a 5 MeV proton should ideally produce the same identifier signal as a 30 MeV proton while 10 MeV and 50 MeV alpha particles should produce the same output signal as each other but quite different from that produced by protons. This case is a simple one as alpha particles and protons differ greatly in their energy loss rate. However the problems become

quite difficult in other cases, for example, if one wishes to separate ^{3}He and alpha particles for which the rate of loss of energy differ only by 25 per cent. There are two principles for particle identification with semiconductor detectors, one based on Bethe-Livingstone rate of energy loss equation and the other on the emperical range energy relationship. We shall describe the second principle below which was used in our system. This method of particle identification was introduced by Goulding [Go 64].

Principle of particle identification

Empirically it has been found that the range of charged particles in matter can be well approximated by the formula

$$R = a\,E^{b} \qquad (3.3.1)$$

where R = particle range in absorber

a = a constant depending on the particle type

E = incident energy of the particle

b = a constant independent of particle type.

A slight deviation from this relation occurs for helium ions at low energies, but these are only about 2%. Over an energy range of 1 to 30 MeV the gradient is fairly constant at 1.73. In fact a gradient between 1.65 to 1.75 can be fitted fairly well.

In figure 3.3.1 the use of this range-energy relation is illustrated in a particle identifier. The particle passes through a ΔE detector and produces a signal ΔE, then enters and stops in an E detector and

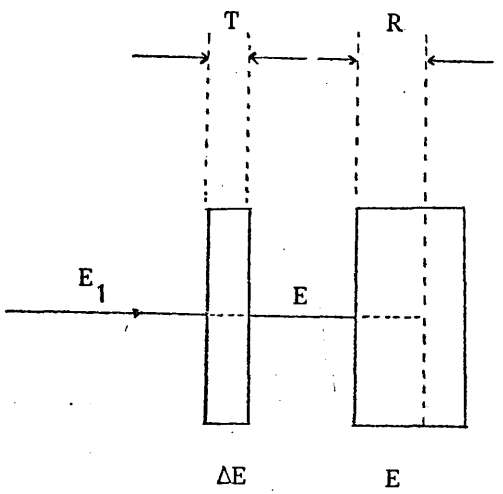

$$R_1 = T+R = a\, E_1^{1.73} \quad \ldots (3.3.2)$$

$$R = a\, E^{1.73} \quad \ldots\ldots (3.3.3)$$

$$T/a = E_1^{1.73} - E^{1.73}$$

$$= (E + \Delta E)^{1.73} - E^{1.73} \quad \ldots (3.3.4)$$

Fig: 3.3.1 Illustration of the use of range energy relationship for particle identification.

produces a signal E. The relation given in equation 3.3.4 shows that the quantity T/a is characteristic of particle type only because 'a' is a function of particle type and 'T' is a constant. So we can see that the identity of a particle can be established by generating the function $(E+\Delta E)^{1.73} - E^{1.73}$ for each particle passing through the system of counters. This function being energy independent has advantage over other methods mentioned earlier. In the following we shall describe principle and working of an identifier based on this principle.

The Identifier

The identifier was based on the principle and design described by Fisher and Scott [Fi67] . A planer field effect transistor has a voltage characteristic of the form [Sh52]

$$i = G\left[V_d - \frac{2}{3}\left\{(V_d+V_g+V_{diff})^{1.5} - (V_g+V_{diff})^{1.5}\right\}/V_o^{\frac{1}{2}}\right] \qquad (3.3.5)$$

where i is the source to drain current, V_{diff} is the diffusion potential for the controlling junction and V_d,V_g are the voltage of the drain and gate terminal measured relative to the source terminal. G is a constant of the particular field effect transistor, essentially source to drain conductance at zero voltage and V_o is the pinch off or saturation voltage. The above voltage current characteristic is obeyed only for voltages below the voltage V_o and varies widely for the type of transistor. For Texas 2N2499 typically the value is about ~ 5V. If V_d is identified with ΔE

and $(V_g + V_{diff})$ with E, it can be seen that $(i-GV_d)$ has approximately the same functional dependence as T/a in equation 3.3.4.

Equation 3.3.5 is for ideal infinite planar device. In practice a power index between 1.6 and 1.7 rather than 1.5 fits the experimental data best. A difficulty arises in identifying the power law unambiguously because the part of the total drain current linearly proportional to the drain voltage must be subtracted to yield the part depending on the power law. The constant, G is also a parameter to be experimentally determined and an uncertainty in G results in quite large uncertainty in estimates of the power index. This difficulty suggests that in practice the power law dependence of $(i-G\,V_d)$ on V_d and V_g may be varied over a small range by selecting different values of G. It is possible to obtain an effective power index of 1.50 to 1.75 for input signal amplitude covering a range 50:1 with only 5% departure from the theoretical formula. Typical values of different parameters for Texas 2N2499 are: $G = 3.3 \times 10^{-3}$ A/V, $V_{diff} = -.32V$, $V_0 = 5.5V$ and power index ~ 1.6. The values are also temperature dependent.

The block diagram of the complete mass analyser is shown in figure 3.3.2. Figure 3.3.3 shows the complete circuit diagram. The FET was chosen so that it had nearest required characteristic among the available sample.

The units were built as single width modules compatible with standard Harwell 2000 series. The counter signals were attenuated to $\frac{2}{3}$ of their amplitude before being applied to the FET, so that the pinch off voltage V_0 is not exceeded and the characteristic equation obeyed for input into 7

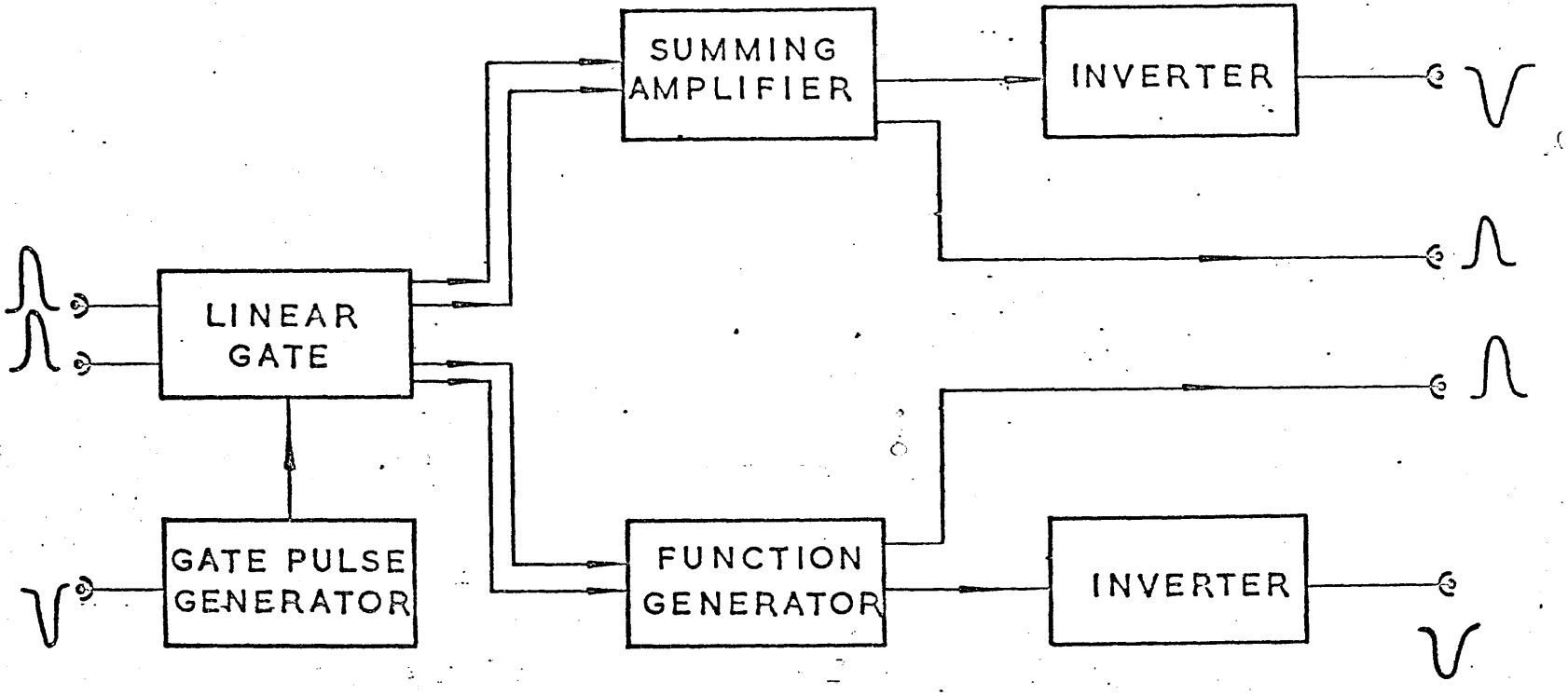

FIG. 3.3.2. BLOCK DIAGRAM OF THE PARTICLE IDENTIFIER

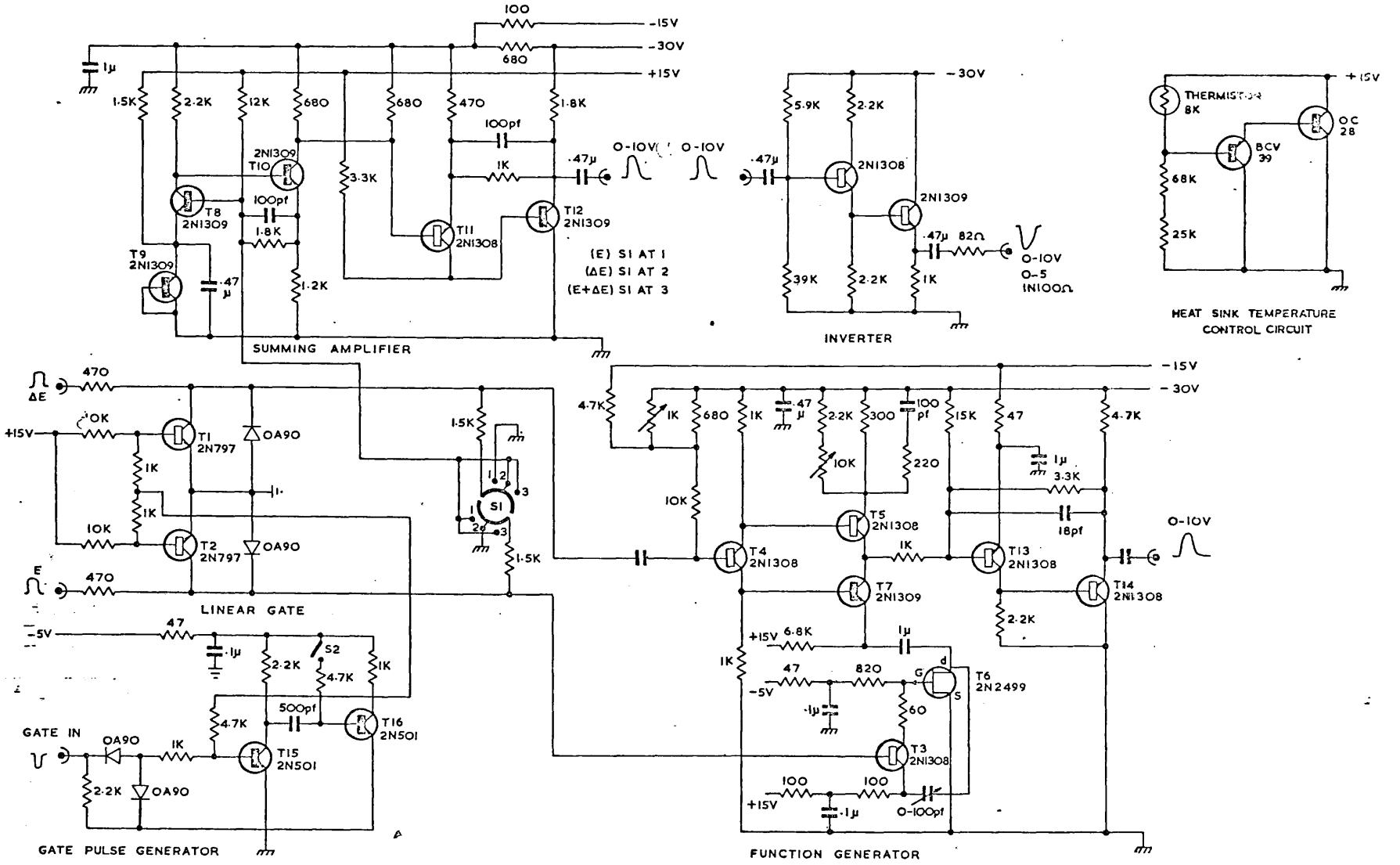

Fig:3.3.3 CIRCUIT OF PARTICLE IDENTIFIER

volts. The FET was mounted on to a brass block kept at a constant temperature of 38^{o}C to ensure that the characteristics of the FET did not vary with the change in the ambient temperature. The short circuit gate in the input was used to gate only the wanted signals.

The summing amplifier combined E and ΔE signals to give a pulse corresponding to total energy. In our case of low energy applications a substantially large fraction of energy was lost in the ΔE counter so it was necessary to add both the signals to get the full energy spectrum.

The gain of the adding circuit had the same value for each input channel. To satisfy the equal gain condition, necessary, for pulses fed to the mass analyser circuit, it was necessary only to set ΔE and E gains such that they give the same output amplitude from the summing amplifier for some energy calibration line (usually an ^{241}Am alpha source).

Set up and Performance of the identifier System

The block diagram of the complete electronic set up for a typical experiment is shown in figure 3.3.4. The monitor counter is used to have a continuous check on the target condition. The power index of the identifier is set up by adjusting G in the identifier circuit and checked using a pulse generator before the start of the experiment.

Figure 3.3.5 shows the identifier spectrum for 12 MeV dueteron bombardment of ^{40}Ca target on carbon. The counters used had a thickness of 25 microns and 1000 microns for the ΔE and E counters respectively.

A not very good separation between the protons and the deuteron was due to the use of a very thin ΔE counter which was necessary so as

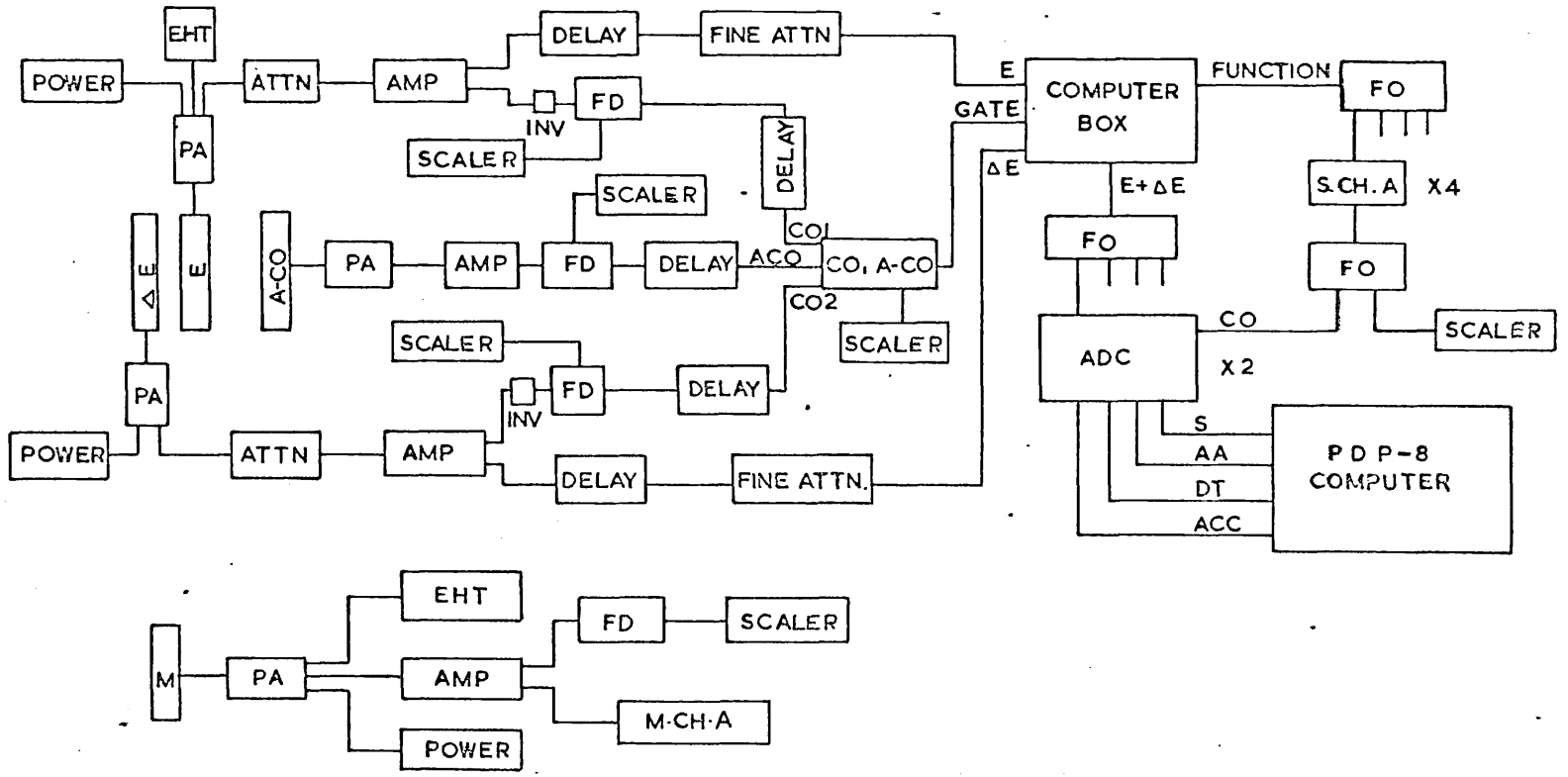

LEGEND

PA	–	PRE AMPLIFIER	CO	–	COINCIDENCE
AMP	–	AMPLIFIER	A-CO	–	ANTI-COINCIDENCE
FD	–	FAST DISCRIMINATOR	S.CH.A.	–	SINGLE CHANNEL ANALYSER
ATTN	–	ATTENUATION	M.CH.A.	–	MULTI CHANNEL ANALYSER
FO	–	FAN OUT	ADC	–	ANALOGUE TO DIGITAL CONVERTER

Fig: 3.3.4 BLOCK DIAGRAM OF COUNTER TELESCOPE SYSTEM.

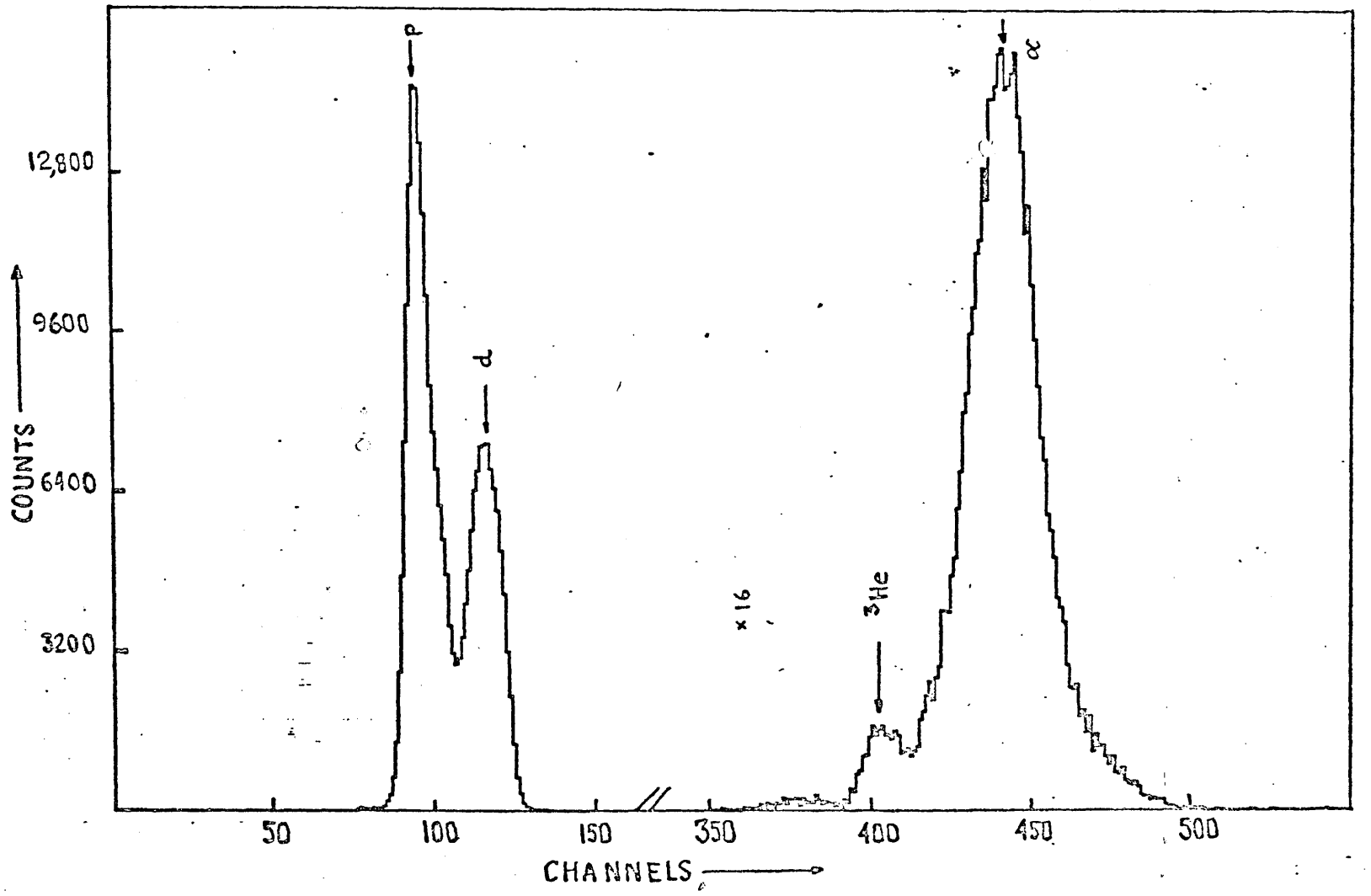

Fig: 3.3.5 An identifier spectrum for deuteron bombardment of ^{40}Ca on carbon at 12.0 MeV.

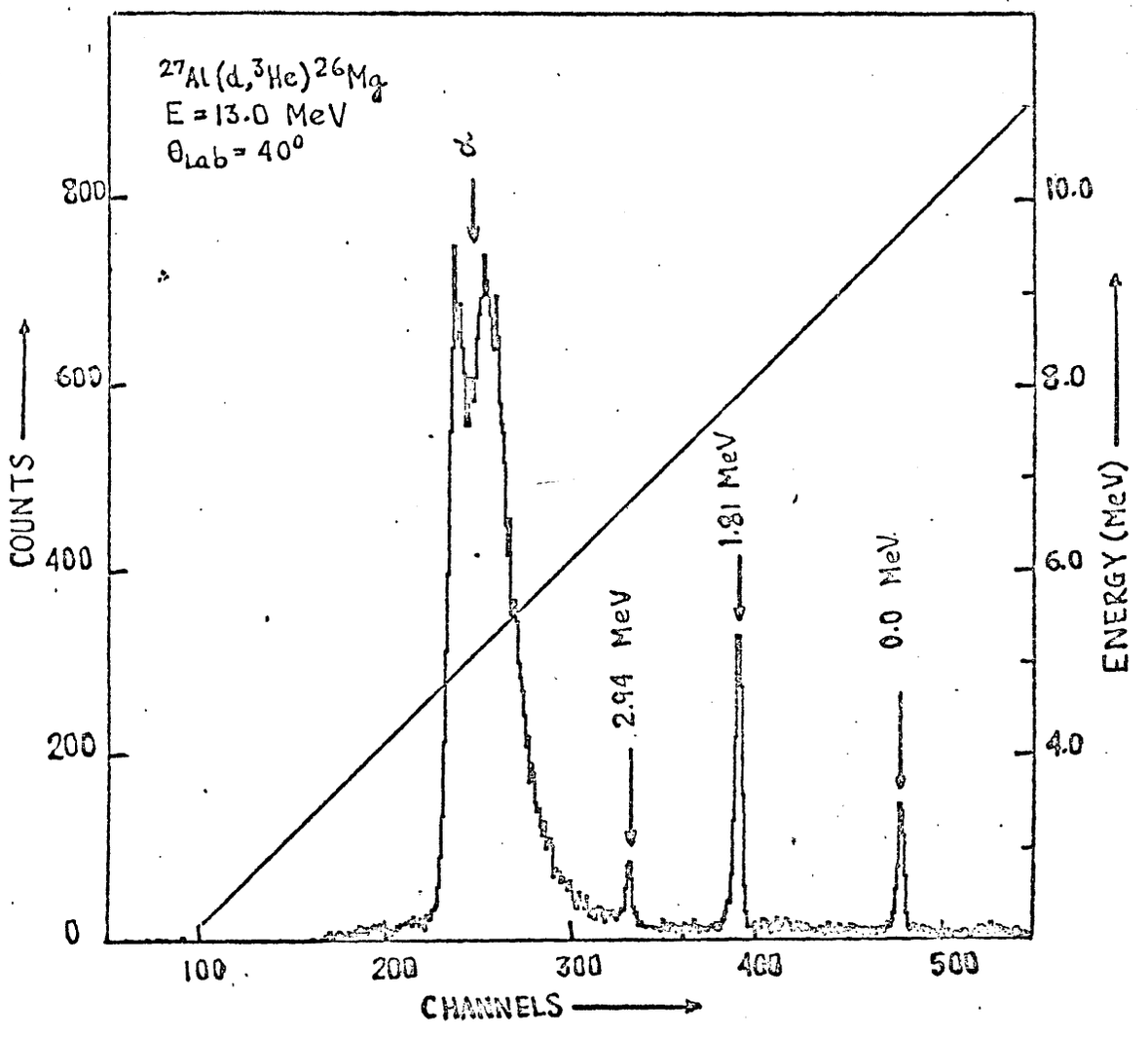

Fig: 3.3.6 A separated ^{3}He spectrum from deuteron bombardment of ^{27}Al at 13.0 MeV.

not to stop the ^{3}He particles in the ΔE detector.

The separation between ^{3}He and alphas was not very good and became worse at forward angles where leaking alpha tail caused serious background problem. Figure 3.3.6 shows a separated spectrum of ^{3}He particles for the deuteron bombardment of ^{27}Al at 13.0 MeV. The large leakage alpha tail was due to wide gate setting for the ^{3}He particles so that none of them was missed.

Overall energy resolution of the system was about ~ 100 KeV and this was one of the limitations which made the system unusable when the levels of the residual nuclei were close together. Another serious limitation of the system was its incapacity to deal with high count rate. This possibly arose due to capacitive couplings in the identifier circuit. This made the system unusable at forward angles further than 20 to 25 degrees due to the large number of elastically scattered particles passing through the system.

3.4 The Scattering Chamber

Figure 3.4.1 shows the photograph of the scattering chamber which is made mostly of aluminium alloy. The side plate fabricated specially for our purpose is shown demounted from the chamber in figure 3.4.2.

The rotating arms were kept vacuum tight by using cylindrical O-ring seals. The two arms formed a concentric assembly and could be moved around independently of each other. For ease of movement under vacuum, the arms were supported on roller bearings. This was specially important for the outer arm because it had considerable area supported against vacuum. Even then it was comparatively stiffer than the central arm.

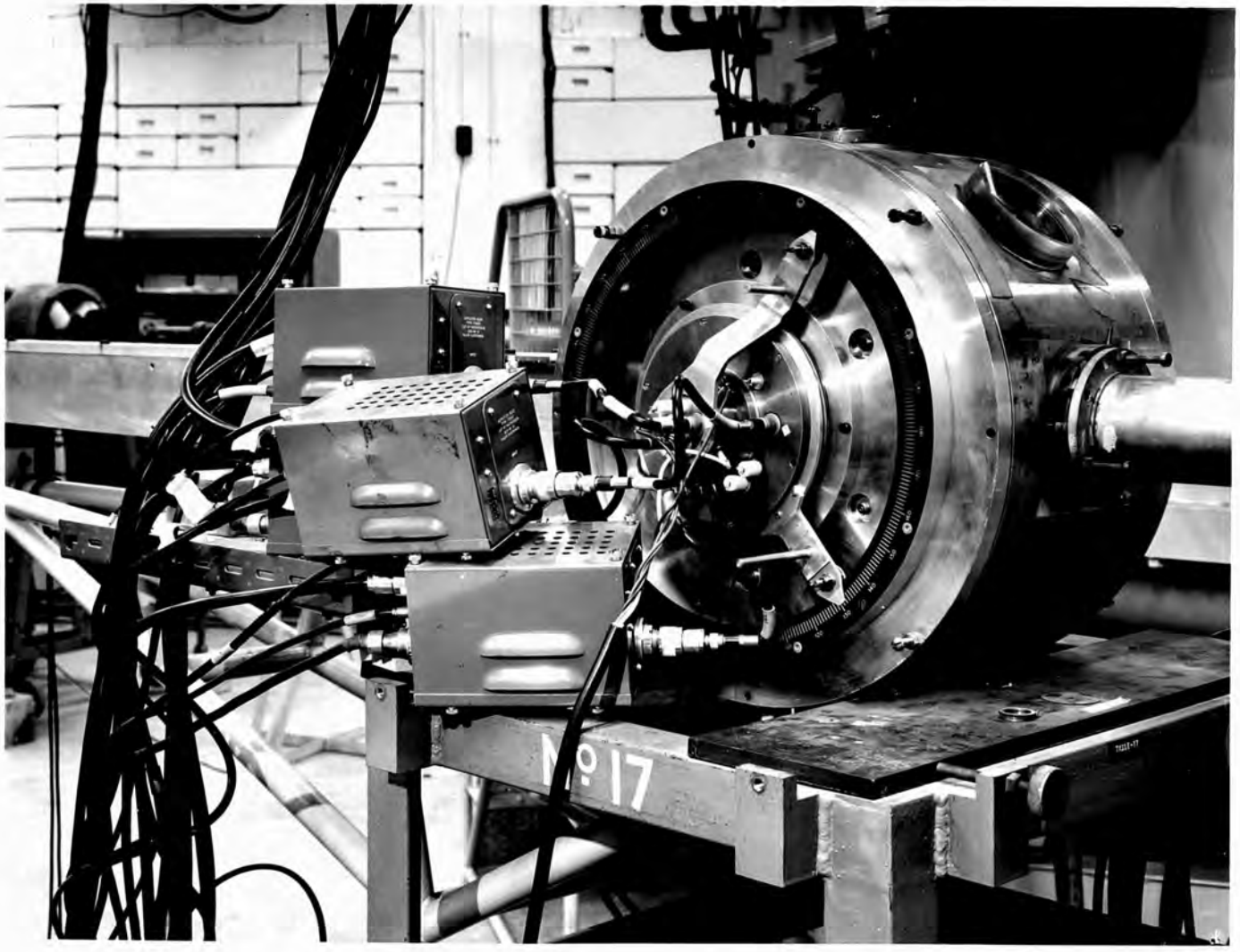

Fig: 3.4.1 The scattering chamber assembly.

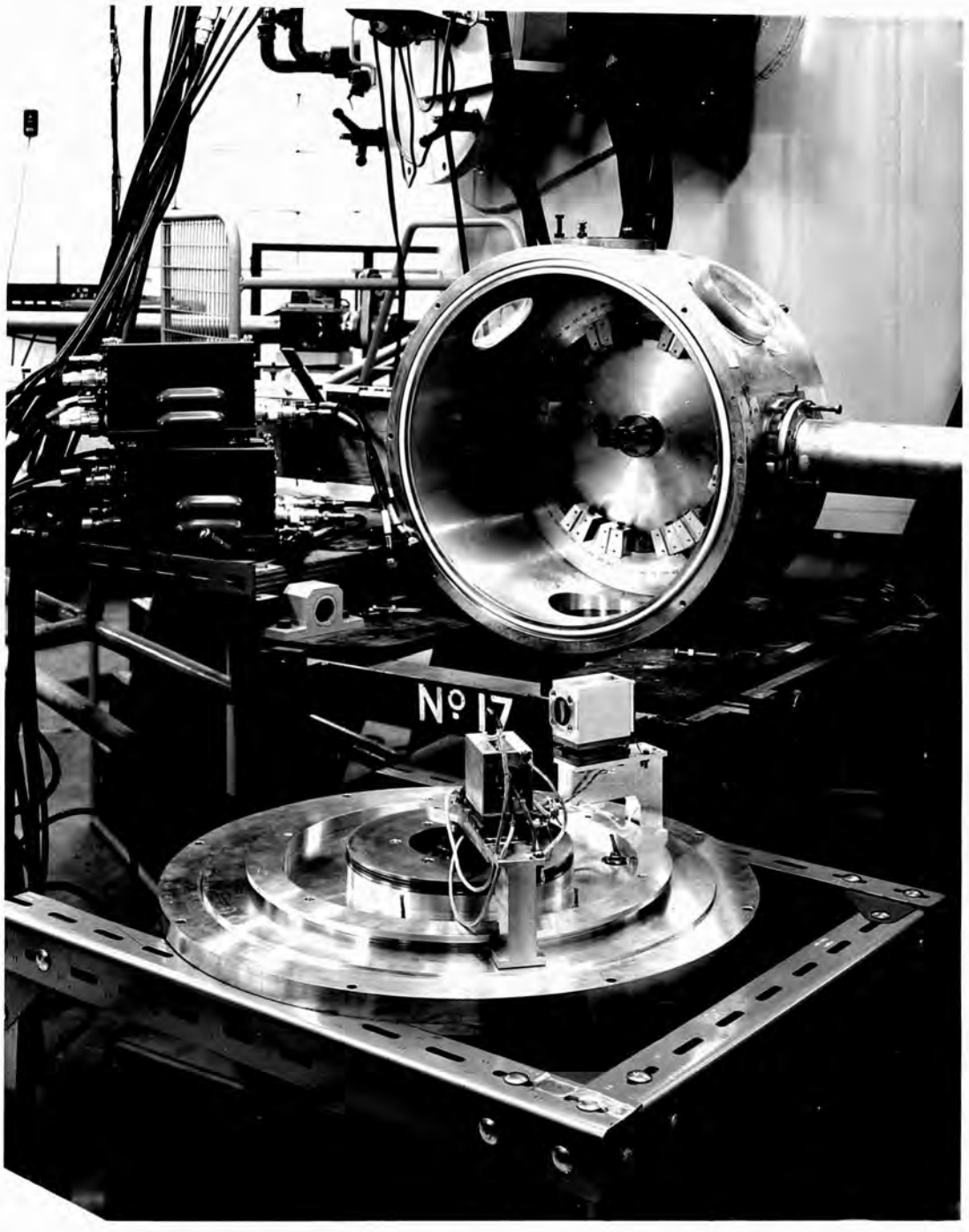

Fig: 3.4.2 The scattering chamber with the side plate demounted.

Figure 3.4.3 shows a sectional view of the side plate. The position of the counter arms are shown by pointers on a circular angular scale on the outer side of the plate. There was some backlash error in the movement of the arms and the angular accuracy of setting was estimated to be ~ 1 degree.

The electrical feed throughs were provided to each of the central bearings of the moving arms so as to avoid entangling of the wires inside. Six feed throughs were available for each arm, two 15 amperes porcelain insulated conductors for the power to the cooling device, two amperes porcelain insulated conductors for the thermistor for temperature control, two co-axial 100 ohm PET connector for signals and EHT supply to the counters. There were also four co-axial feed throughs on the plate itself for the fixed counters.

Facility for cooling the counters was provided by semiconductor thermo-electric devices based on the Peltier effect. The devices used were made by Melcor Ltd (USA) and were of type CP 2-31-10. Their quoted capacity was 51 Bthu/hour for temperature difference of 15°C at 27°C . It required a current of 8.5 amperes at 3.65 volts. Figure 3.4.4 shows a sectional diagram of the counter holder.

Figure 3.4.5 shows the power supply and control electronics for the cooling device. The temperature of the counter holder was sensed by a thermistor which was essentially a negative temperature coefficient resistor. The thermistor formed a part of a resistance bridge. The control circuit could compare the potential at the bridge junction to a preset potential which represents the temperature required. Whenever

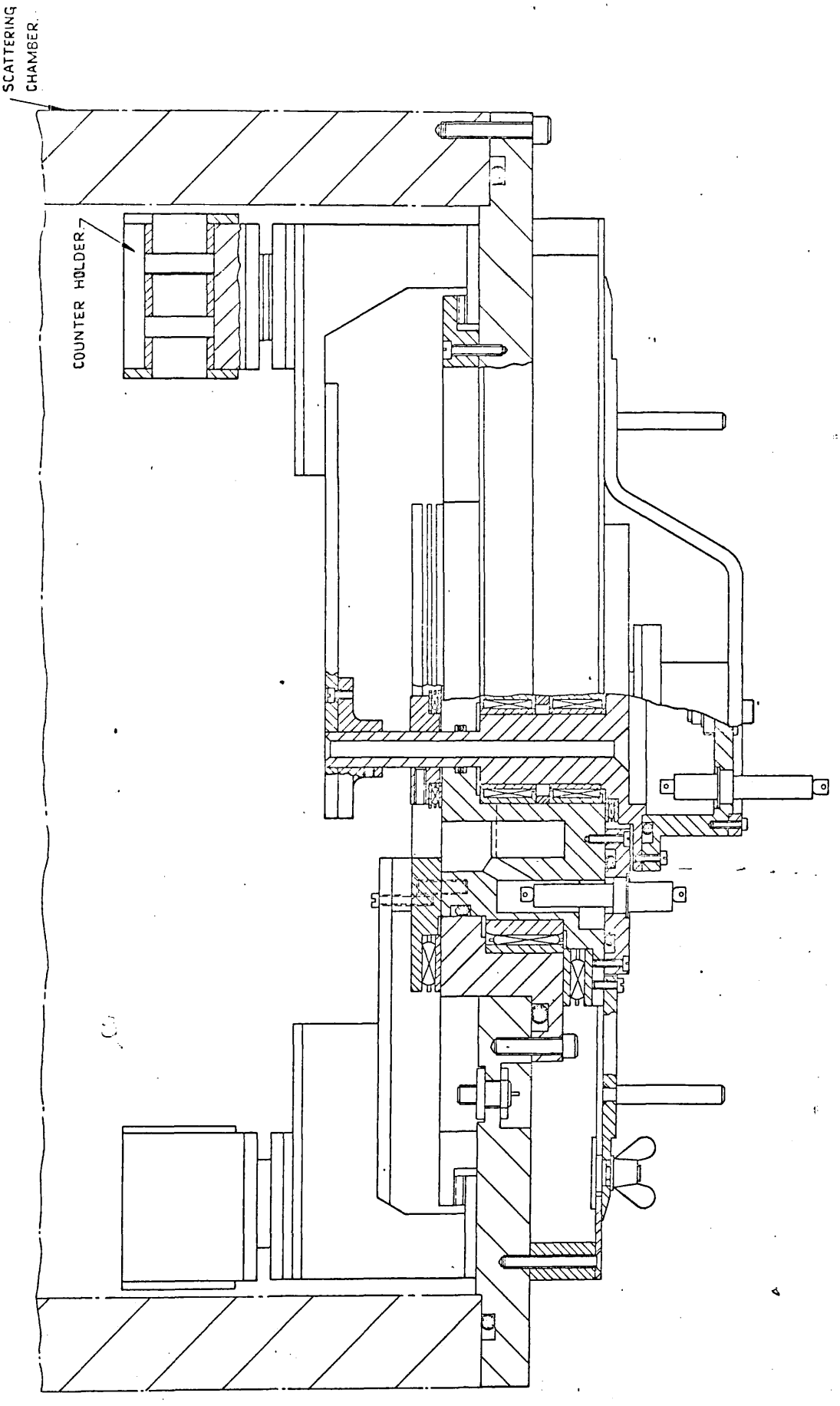

Fig: 3.4.3 A section diagram of the side plate.

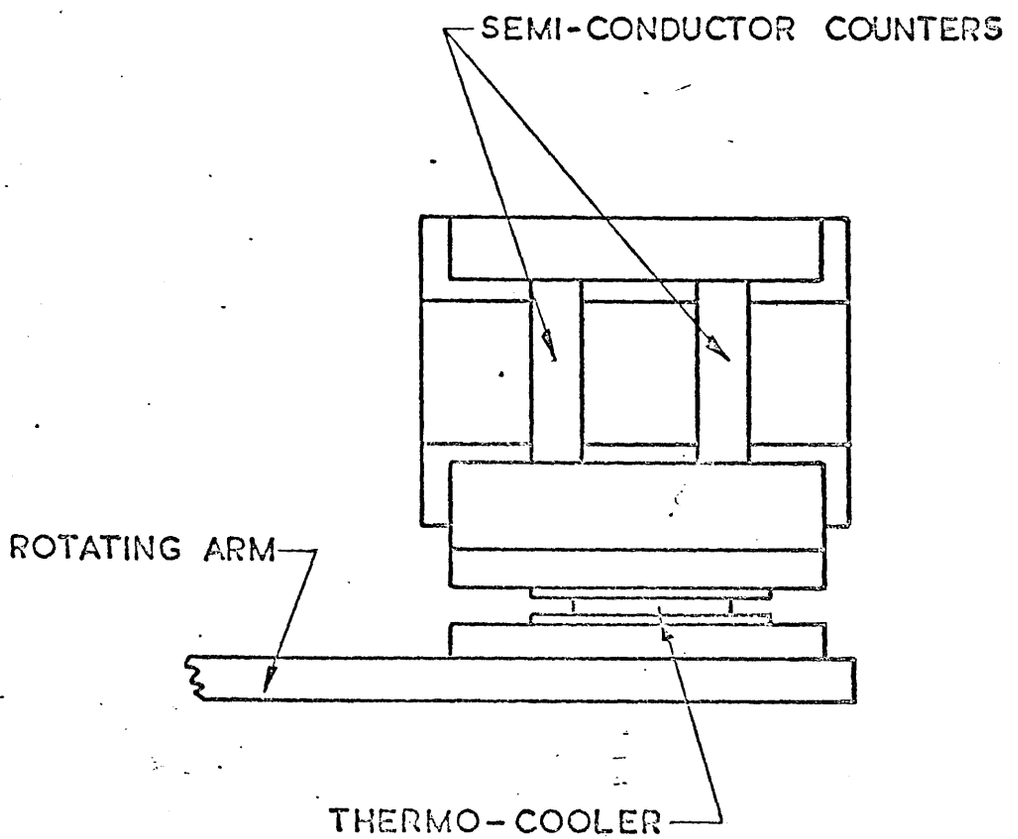

Fig: 3.4.4 A sectional diagram of the cooled counter holder.

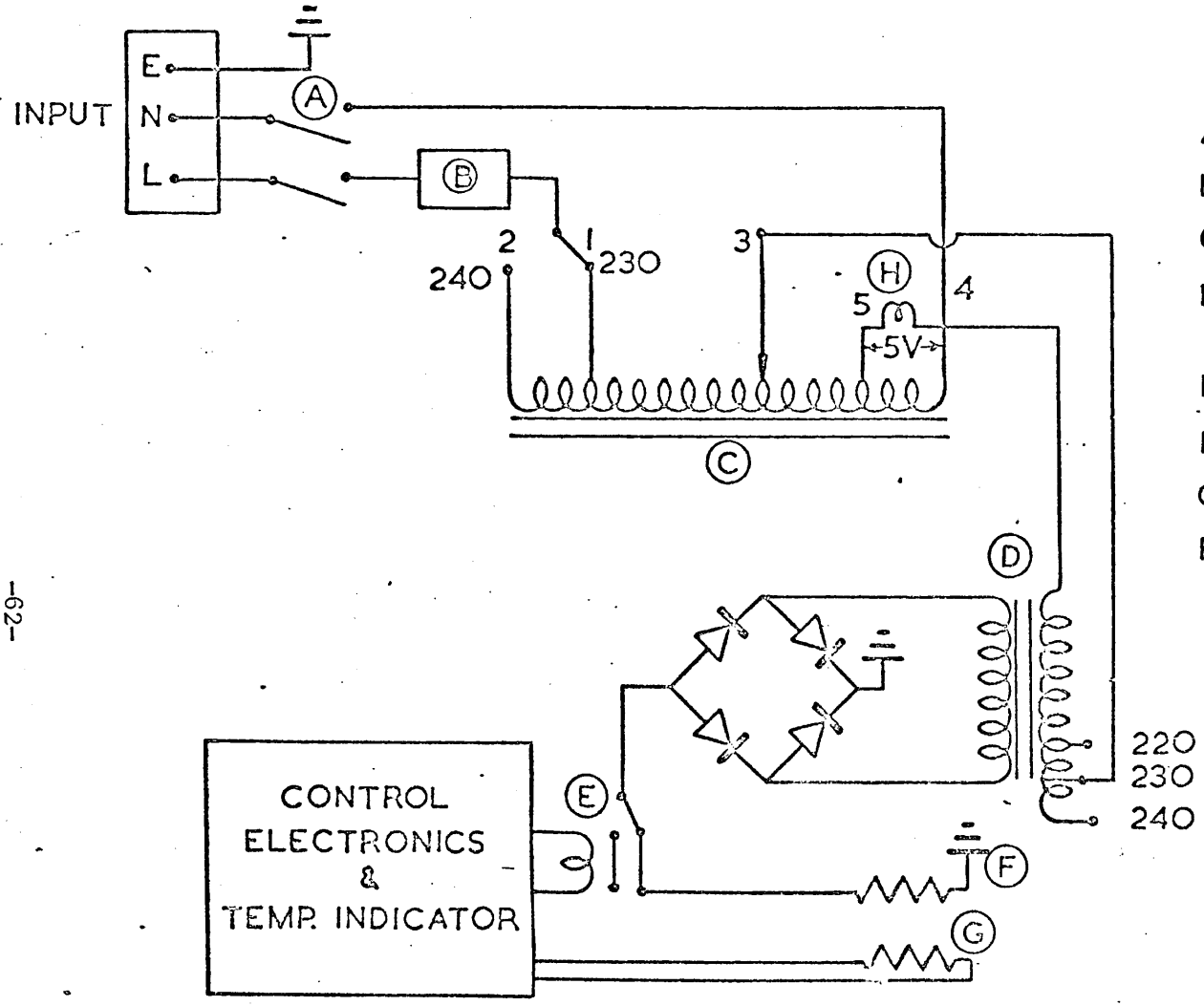

A: TOGGLE SWITCH

B: 2 AMP FUSE

C. 750VA VARIAC

D. LOW VOLTAGE HIGH CURRENT TRANSFORMER

E. 2 WAY 15AMP RELAY

F. THEROELECTRIC DEVICE

G. THERMISTER

H. INDICATOR LAMP

Fig: 3.4.5 COOLING & TEMPERATURE CONTROL SYSTEM

this temperature was reached cooling was switched off and if the temperature had risen again it was turned on by the operation of a relay by the control circuit. The temperature control system was designed by the author.

3.5 Spectrograph System

Introduction

In discussing the limitations of the counter telescope particle identification system, it was pointed out that the system was incapable of dealing with high count rate ($> 10^4$ per second). So the system could not be used at forward angles where the count rate due to elastically scattered particles increased tremendously.

For this reason it became necessary to use the Buechner magnetic spectrograph to get data at angles less than 20 to 25 degrees. It was possible with suitable setting of the magnetic field and detectors to look only at required groups of particles. The main disadvantage of the spectrograph was its poor geometrical efficiency and hence was not used when count rate and resolution permitted the use of the telescope system.

The Magnetic field of the spectrograph is uniform with a circular boundary and is capable of focussing particles from a source outside the field onto a hyperbolic focal surface. Particles of energy varying as much by a factor of 2.5 can be focussed on to the focal plane. Details of the spectrograph have been described elsewhere [Br56]

Until recently the only practical focal plane detector for use with the spectrograph has been nuclear emulsion plates. They suffered

from serious disadvantages that (i) data are not available quickly, (ii) accidents like light fogging and incorrect exposure remain undetected until it is too late to remedy the situation.

But with the availability of the position sensitive detectors, situation has changed and it is now possible to get data 'on line' electronically. The system which we have used was designed by Allan et al. [Al68]. A brief description of the use of position sensitive detectors (PSD) in conjunction with the magnetic spectrograph is given below.

Use of Position Sensitive Detectors (PSD) with the Spectrograph

The method of using a PSD is illustrated in figure 3.5.1. The construction and performance of the PSD's used have been described elsewhere [Ow67]. A PSD is a surface barrier detector with resistive layer coated on one face, one end of which is earthed and the other connected to pre-amplifier (figure 3.5.1). The charge deposited in the detector by a charged particle is divided between the two ends of the resistive layer in such a way that the fraction arriving at the input of the pre-amplifier is proportional to the total energy E deposited multiplied by the distance x between the point of entry of the particle and the earthed end.

The relationship between the energies of the various types of reaction product is given by

$$E_p = E_\alpha = 2E_d = 2E_t = \tfrac{3}{4} E_{^3He} \qquad (3.5.1)$$

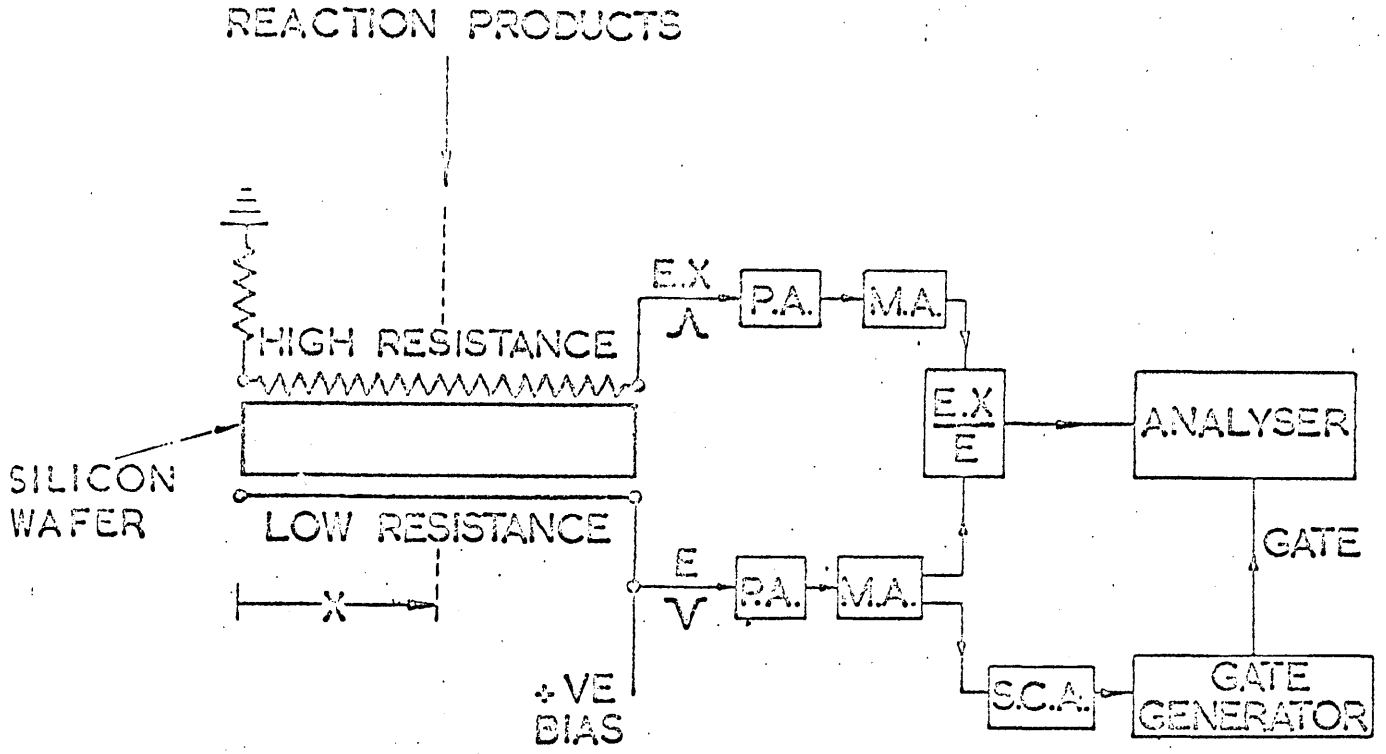

Fig: 3.5.1 Illustration of the use of a position sensitive detector. (Abbreviations are explained in fig. 3.5.3).

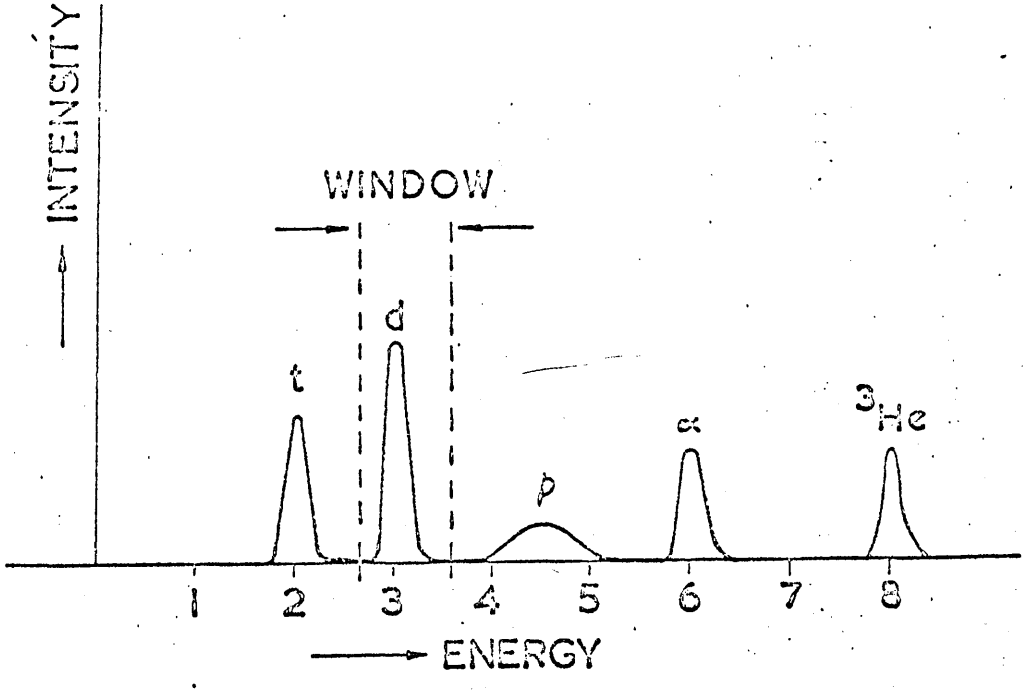

Fig: 3.5.2 Illustration of the energy spectrum from a PSD used in conjunction with a magnetic spectrograph.

for a given magnetic rigidity $B\rho$, of these product the protons will always have the greatest range and if the depletion layer depth is insufficient to stop them while stopping the other particles, the energy spectrum appears as illustrated in the figure 3.5.2. Particle selection can be accomplished by setting a window across the energy group corresponding to the desired particle.

To extract the position information x from the output pulses E.x it was necessary to divide this output signal by the energy signal E. This had the added advantage of eliminating positional inaccuracies caused by spread in the E signal. The spectrum corresponding to chosen reaction product is obtained by analysing the output $\frac{E.x}{E}$ of a divider circuit in coincidence with the window output of the particle selection circuit.

The system was capable of using a maximum of eight detectors. The figure 3.5.3 shows the block diagram of the electronic system used in conjunction with a PDP-8 computer. However in our case it was not necessary to use all eight detectors on any single occasion.

The detectors used were of thickness of one millimeter and had positional resolution of $\sim$ 0.5 mm. They were used with a tantalum mask of 5mm x 44mm dimension.

3.6 Multigap spectrograph

As mentioned earlier, due to non-availability of high enough beam current the multigap spectrograph had to be used for some of our studies. The advantage of the multigap over the other methods is the

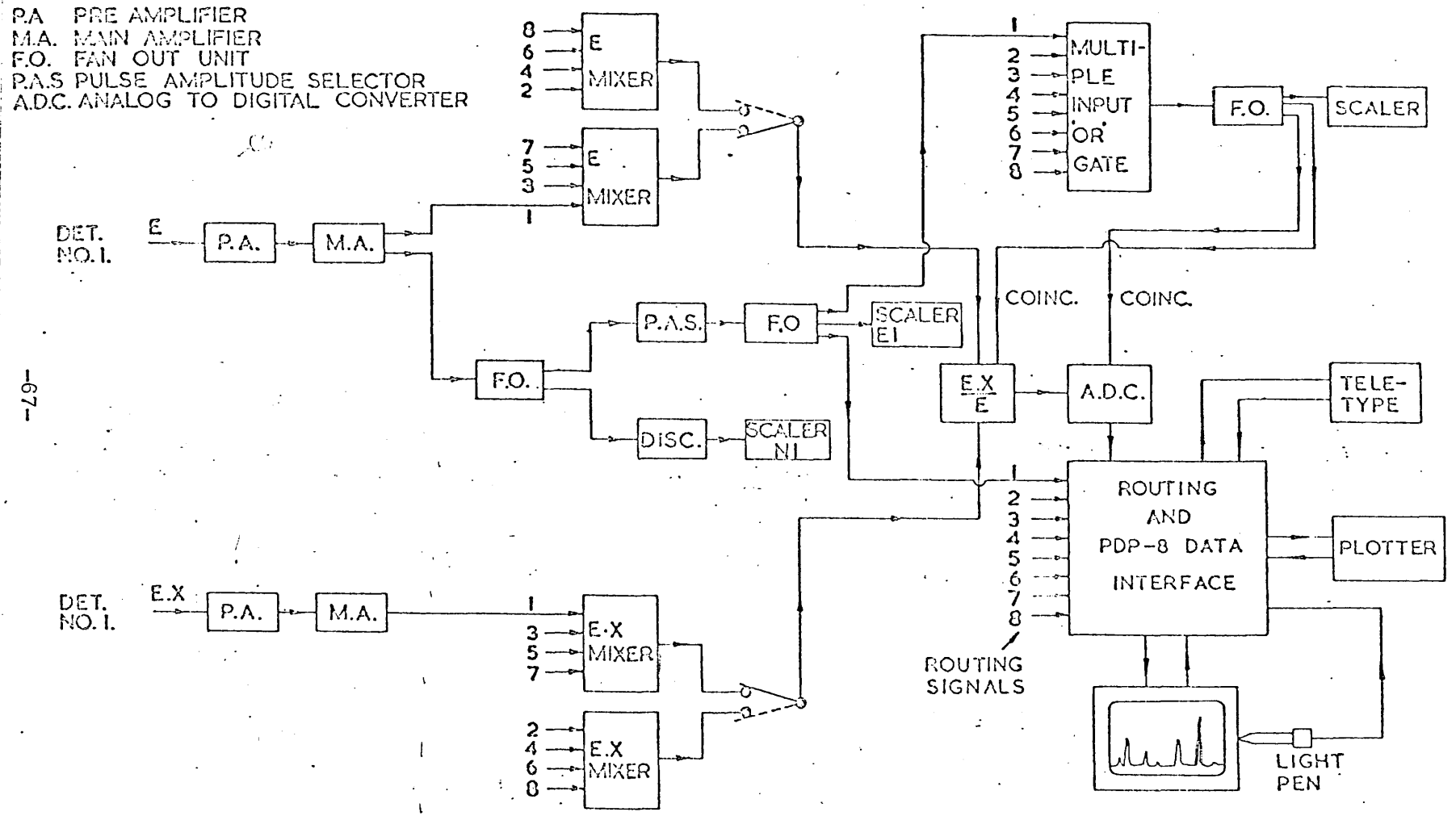

Fig: 3.5.3 Block diagram of the electronics of a typical experiment with Buechner magnetic spectrograph using PSD's.

possibility of observing reaction products at many angles simultaneously and elimination of the target deterioration problem. A brief description of the Harwell multi-gap spectrograph is included here. More detailed description of multi-gap spectrographs can be found in literature [Mi62, En63].

The multigap spectrograph is based on the same principle as the single gap spectrograph described earlier. The Harwell multigap spectrograph (originally of Aldermaston) is essentially a combination of 24 single gap spectrograph arranged around the target in a circle. The separation between the gaps is 7.5^{o} with the exception between the 12th and 13th where it is 2.5^{o}. The angle of the first and the last gaps are 5 and 175 degrees respectively. The solid angles for the gaps is $\sim 3 \cdot 10^{-4}$ str. for 4th to 24th gap.. The first, second and third have magnitudes of ¼, ½, 1/1.33 of the normal value respectively.

The solid angle varies along the focal plane so that correction has to be applied to data on this account.

The length of the focal plane is one meter. The only practical method of detection of particles at the focal plane available at the moment is nuclear emulsion. The maximum and the minimum radii of curvature of the focal plane are 59.08 and 31.26 cm respectively. Contributions of the spectrograph geometry to energy resolution is of the order of ~ 10 KeV.

3.7 Neutron Detection and Time of Flight System

Neutrons being electrically neutral have to be detected indirectly, such as looking at recoil protons in hydrogeneous material due to collision with the neutron or charged particles produced in neutron induced reaction. This makes it very difficult to measure energy of the neutrons precisely.

The most suitable method of energy measurement for neutrons in the energy region of 100 keV to 20 MeV is the time of flight method. In this method time of flight of neutrons between two fixed points and hence the velocity of neutrons is determined. Energy is then deduced from velocity. What is required for this method is a neutron source which should emit neutrons during a short interval, so that time of emission can be determined accurately.

Pulsed Van-de-Graaff at Harwell (IBIS) has a pulse length of ~ 1 nano-second and is very well suited for this technique. Scintillation counters are normally used to detect the neutrons because of their fast response time. In the following we shall give a brief description of the actual detector used and its associated electronics.

The system used for our experiments was constructed by Adams et al [Ad67]. The scintillator used was NE-213 and the photo-multiplier was XP-1040 (AVP-56) which has a rise time of about ~ 2ns. Two pulses were taken from the detector. A fast pulse from a floating anode was used for timing as well as pulse shape discrimination. A linear pulse from the 11th dynode was taken out and was used for energy (noise)

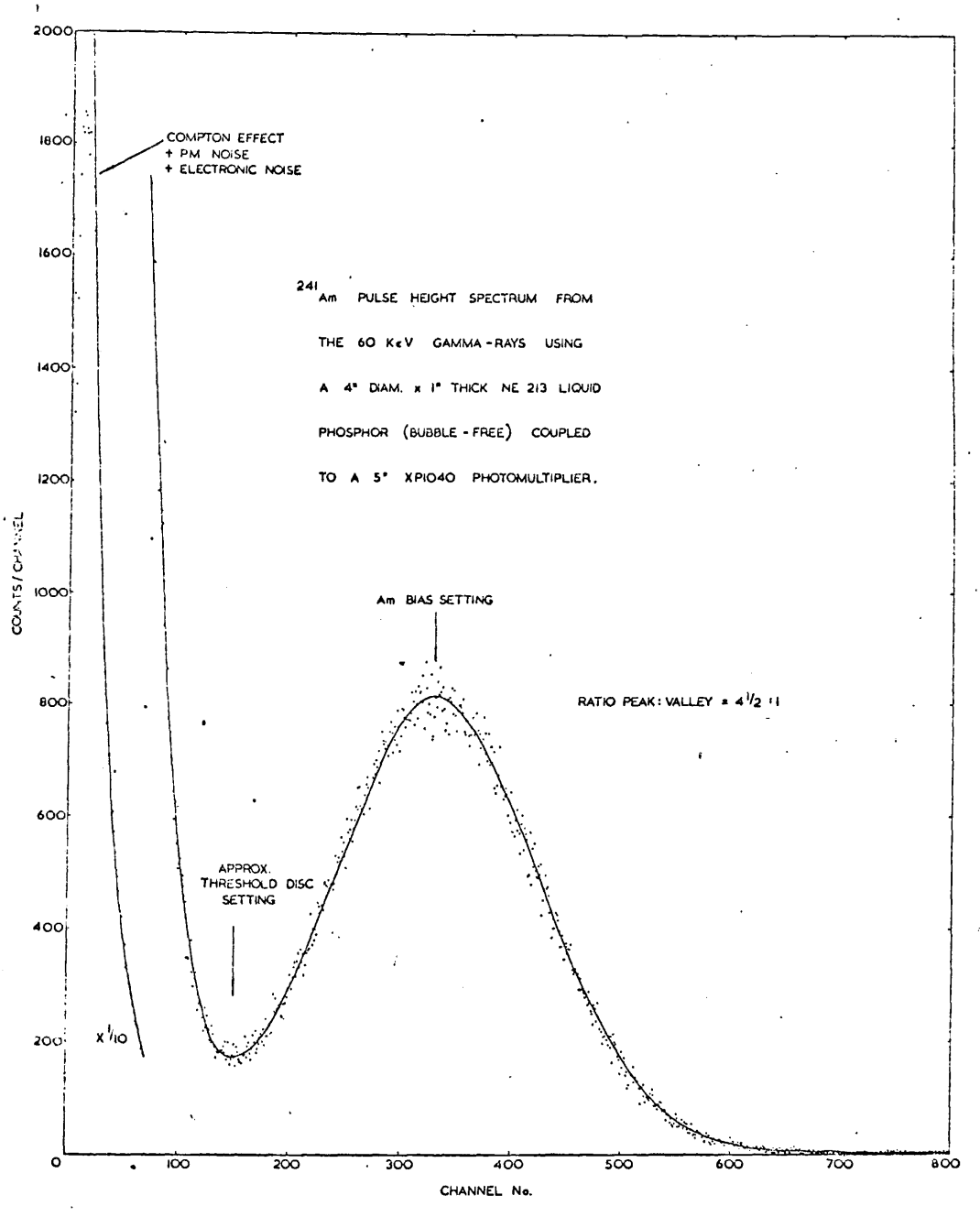

Fig: 3.7.1 Response of scintillator-Photomultiplier assembly to ^{241}Am γ-rays.

discrimination purpose. The energy bias was set by using an ^{241}Am source, which produces 60 KeV γ-rays, which approximately corresponds to 500 KeV neutrons. This is illustrated in figure 3.7.1.

The timing pulse from the detector was used as start pulse of the time to amplitude converter (TAC). The pulse, corresponding to arrival of the charge particle beam at neutron producing target was picked by a hollow copper cylinder placed near the target and was used, with suitable delay, as stop pulse. This reversal of sequence has the advantage that it avoids unnecessary dead time in the TAC. Sensitivity of the scintillator to γ-rays constitutes background problem as γ-rays are invariably present in all experiments. The prompt γ-rays are the fastest arriving particles at the detectors and so give a single peak irrespective of energy. But more troublesome ones are the random γ-rays produced by the decay of the reaction products in the target and other sources which may be present in the vicinity. This gave rise to white background which causes serious problems for low yield experiments.

In order to eliminate this random background a pulse shape discrimination (PSD) system has been developed at Harwell [Wh66, Ad67] which is based on the fact that γ-ray pulses decay faster than neutron pulses. The output of the detector is divided in two parts which are integrated over 30 and 500 nano-seconds respectively. The amplitudes from both the integrators are equal in the case of γ-rays since γ-ray pulses decay within 30 ns and they are unequal for neutrons due to the presence of a long tail in the neutron pulses. Figure 3.7.2 shows the block diagram of the PSD set up. Figure 3.7.3 shows the complete

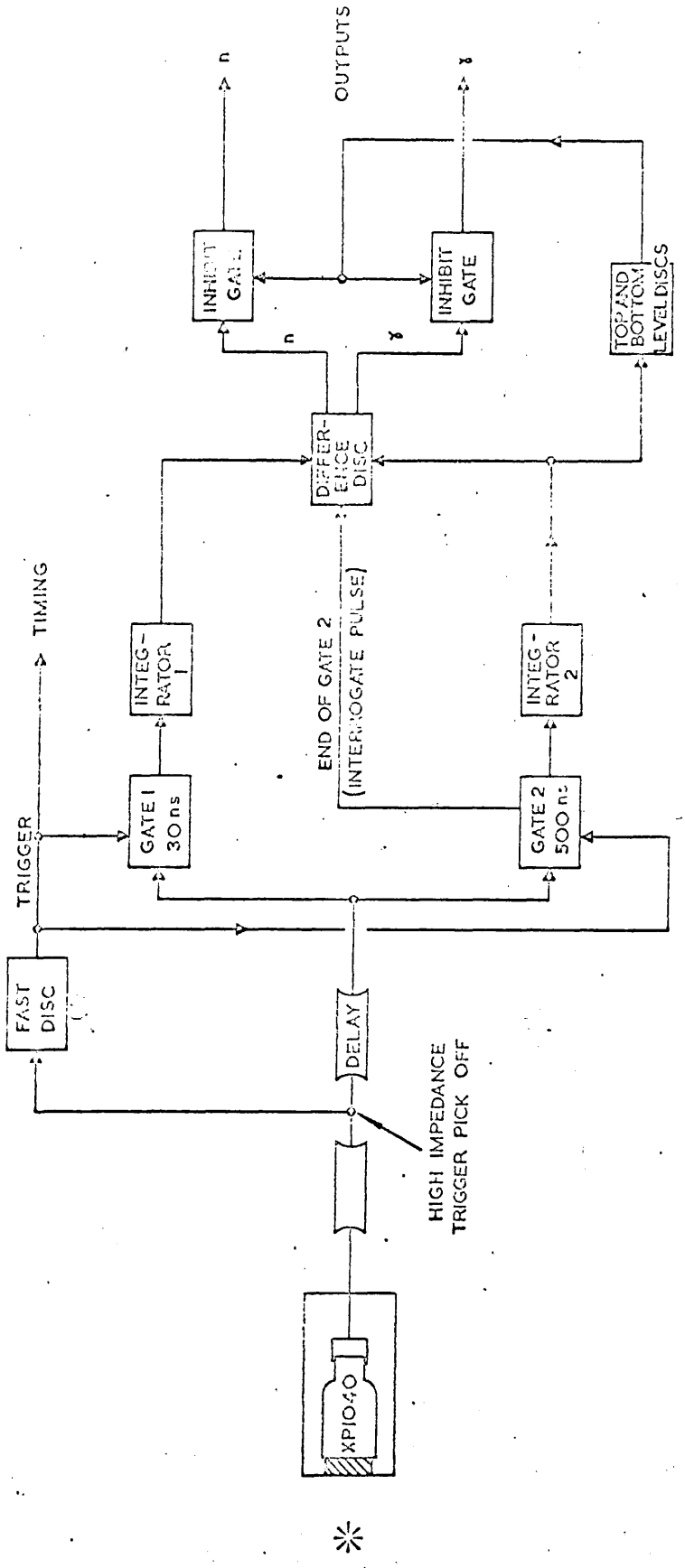

Fig: 3.7.2 PULSE SHAPE DISCRIMINATION SYSTEM.

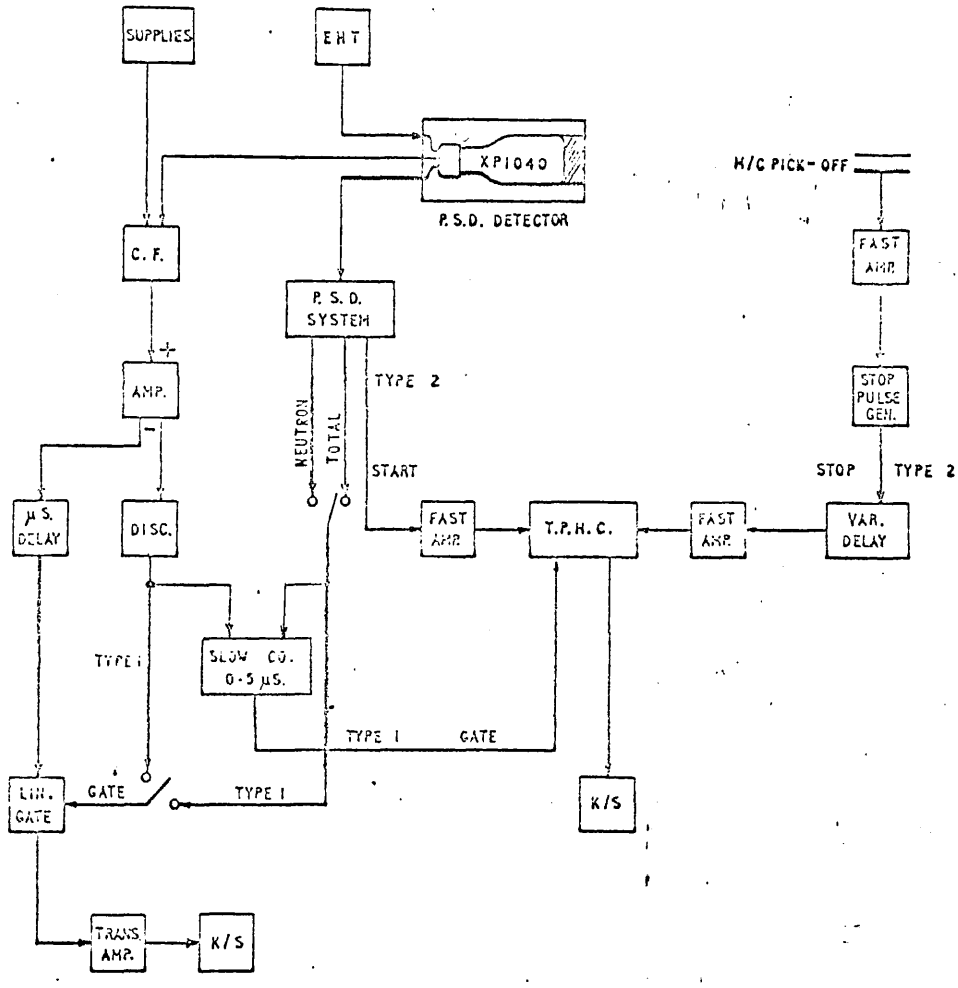

Fig: 3.7.3 ELECTRONIC BLOCK DIAGRAM FOR A TIME-OF-FLIGHT SYSTEM USING THE PULSE SHAPE DISCRIMINATION SYSTEM

counting system using pulse shape discrimination.

3.8 Tandem Van-De-Graaff Generator

In the tandem van-de-Graaff a single high voltage terminal is used twice to accelerate charged particles using the charge exchange principle. Figure 3.8.1 shows a schematic diagram of the Harwell tandem together with the plan and section of the building.

The ion-source at the top injects singly charged negative ions into the accelerator tube. These negative ions get accelerated to the positively charged terminal where they undergo charge exchange to become positive ions. These positive ions receive further acceleration due to repulsion from the positively charged terminal. The maximum attainable voltage of the terminal is 6.5 million volts. Main attractive features of tandem are:

1) Good energy stability, which is of the order of few KeV.

2) Continuous variability of the energy.

3) High beam quality and low machine background.

3.9 The Ibis Van-de-Graaff

The IBIS (Intense bunched ion source) Van-de-Graaff is a nominally 3 MeV machine. The principal feature of this machine is its capacity to produce pulsed ion beams of very short duration (1 ns). The principle of pulsing is illustrated in the figure 3.9.1. A 10 ns ion brust, at one Mhz repetition rate, is produced at the ion source by using rf electro static deflection. After the acceleration this 10 ns pulse is compressed to 1 ns using Mobley bunching mechnism.

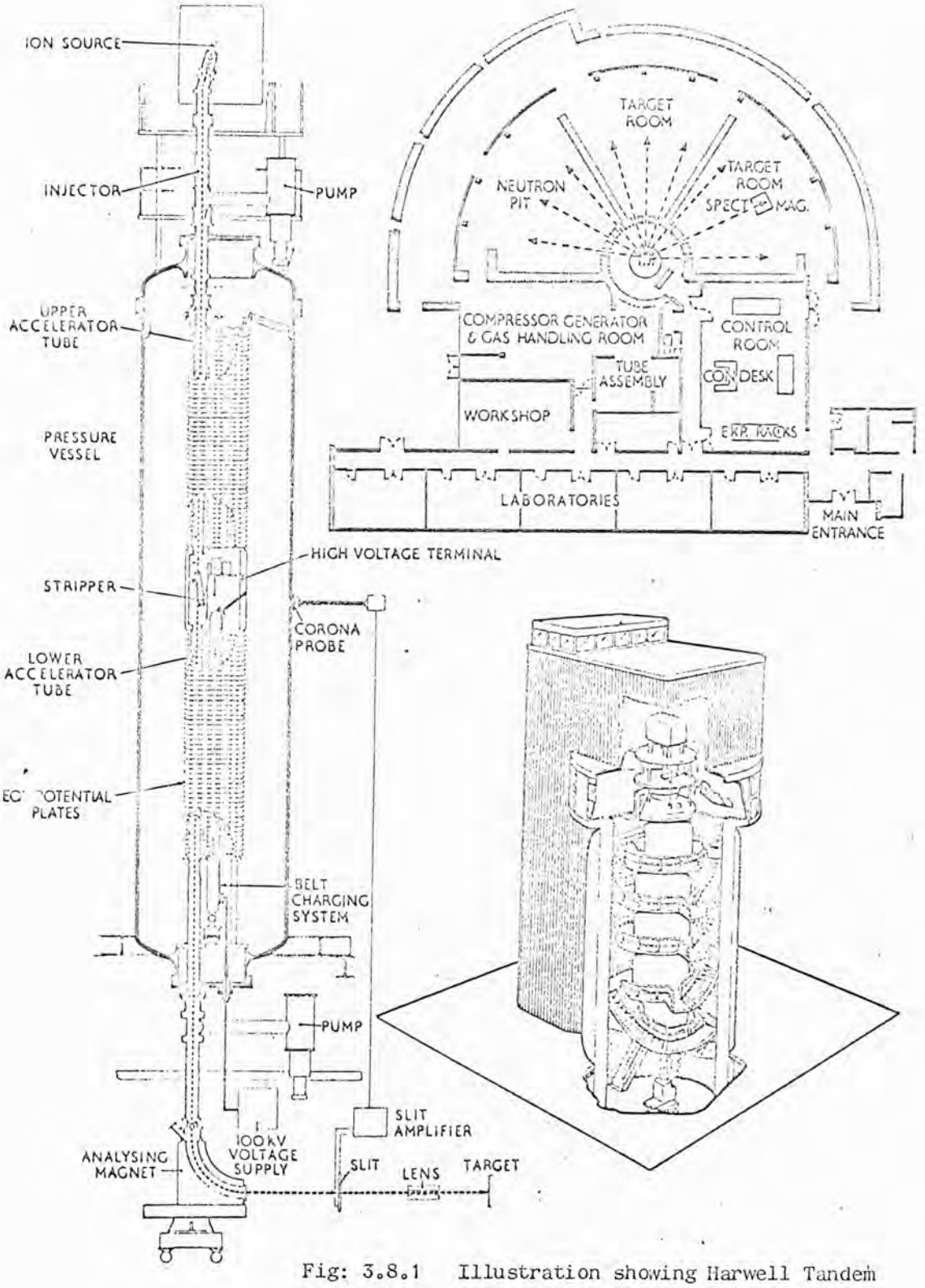

Fig: 3.8.1 Illustration showing Harwell Tandem and ancillary facilities.

Fig: 3.9.1 **IBIS: METHOD OF BUNCHING PROTON PULSE**

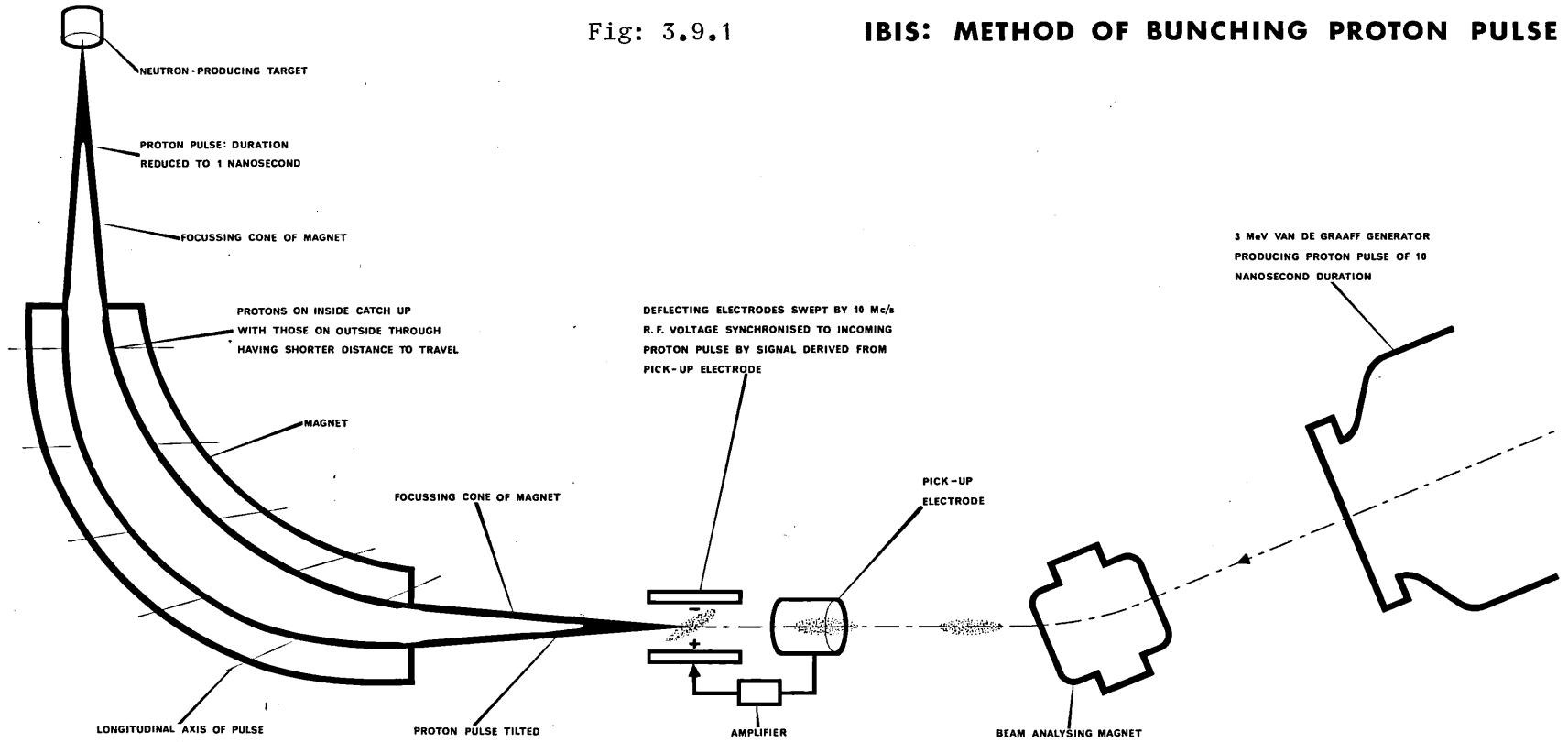

With this type of bunching there is no loss of ions in compressing the ion burst by a factor of ten and virtually no increase in the intrinsic beam energy spread. There is introduced, however, an angular spread in the ion beam which depending on the ion velocity can be up to 2.5^{o}. The IBIS is used mainly to accelerate light ions, i.e. protons, deuterons, ^{3}He and ^{4}He.

CHAPTER IV

EXPERIMENTS, DATA AND THEIR REDUCTION

4.1 Introduction

In this chapter different experiments and data analysis procedures are discussed. The description of different experiments have been grouped together in sections where same instrumentation were used. The data reduction procedures have been collected together in another section.

4.2 Beam and Target Technique.

A schematic set-up of the beam optics is shown in figure 4.2.1. Beam from the machine was bent through 90 degrees by the bending (analysing) magnet, which was then focussed by a pair of magnetic quadrupole lenses. The flap box had the facility for monitoring the beam. The shape of the beam spot could be monitored by putting a quartz flap in the path of the beam and looking through a closed circuit television camera. The beam current could be monitored by bringing in a tantalum flap in the beam path. The beam was then collimated by a system of apertures to satisfy the geometrical

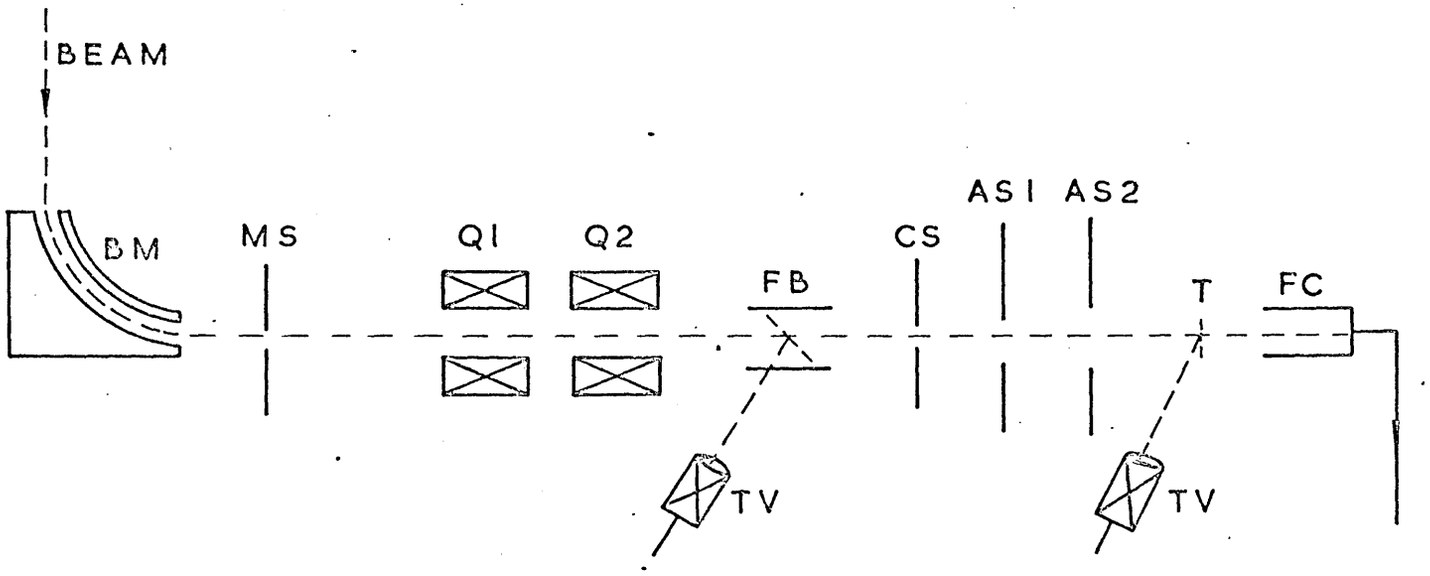

LEGEND:

BM – BENDING MAGNET	CS – COLLIMATING SLIT
MS – MACHINE SLIT	AS – ANTI-SCATTERING SLIT
FB – FLAP BOX	FC – FARADAY CUP
TV – TELEVISION CAMERA	T – TARGET
Q – MAGNETIC QUADRUPLE LENS	

FIG.4.2.1. SCHEMATIC DIAGRAM OF BEAM OPTICS.

requirements of the experiment. Specific details of the collimating requirements are pointed out in each experiment under discussion.

Beam monitoring

After passing through the target the beam was collected in a Faraday cup. Charge collected in the cup was measured by using standard Harwell 2040 system. It gave measurements directly in fractions of a coulomb, the absolute value of which was believed to be correct within 3%. The relative values were more accurate. The calibration of the beam monitoring system was checked from time to time by using a precision current generator.

In order to avoid error in the integrated charge due to emission of secondary electrons from the Faraday cup magnetic and electric suppressions were used. Magnetic suppression was used in the single gap spectrograph experiments. This was achieved by maintaining a constant magnetic field (~ 1 KG) near the entrance of the Faraday cup. Electric suppression was used in the scattering chamber experiments which was achieved by maintaining a one inch diameter guard ring at a voltage of -120 near the entrance to the Faraday cup. Aperture of the Faraday cup was chosen so that it was large enough to collect the beam without significant loss.

Targets

Targets were made by evaporation of the elements in suitable form onto proper backing. In a few cases the targets were self supporting. Table 4.2.1 shows the composition of the targets used.

Table 4.2.1

Element	Enrichment	Material	Backing	Thickness
^{45}Sc	Natural	Metal	Thin carbon ($10\mu g/cm^2$)	$\sim 100\mu g/cm^2$
^{40}Ca	"	Oxide	"	$\sim 100\mu g/cm^2$
^{37}Cl	97.8	Silver-Chloride	"	$\sim 50\mu g/cm^2$
^{35}Cl	96.95	"	"	"
^{29}Si	92.0	Element	"	$\sim 200\mu g/cm^2$
^{27}Al	Natural	Metal	Self-supporting	$\sim 100\mu g/cm^2$
^{25}Mg	98.2	"	"	$\sim 200\mu g/cm^2$
^{23}Na	Natural	Oxide & Bromide	Thin carbon	$100\mu g/cm^2$

4.3 Scattering Chamber Experiments

The Scattering chamber described in section 3.4 was used for both elastic scattering and transfer reaction studies for angles greater than 20 to 25 degrees. A schematic set up of an experiment using scattering chamber is shown in figures 4.3.1.

A single aperture of 2mm diameter about a meter away was used as collimator. There were several (2 to 3) anti-scattering slits of 5mm diameter.

In elastic scattering experiments single counters were used for monitoring and angular distribution measurements. For the transfer reactions the angular distributions were measured using the counter telescope. The monitor was a single counter as in the elastic scattering cases. The monitor counter gave the status of the target while the experiment was going on. The data from the monitor were also used to correct for changes in target thickness due to change of target orientation or evaporation of the material of the target due to heating by the beam.

The telescope was set-up for equal gain for both E and ΔE counter prior to the experiment using an alpha source usually ^{241}Am. The energy resolution of the system with counters cooled to $10^{o}C$ was ~ 90 KeV. Cooling to lower temperature was not possible due to different coefficient of expansion of silicon and the mount of ΔE detector. The energy resolution was found to be ~ 150 KeV with the beam on. As suggested by Anderson et al. [An67], the deterioration in the resolution with the beam on was assumed to be largely due to electrons produced in the target.

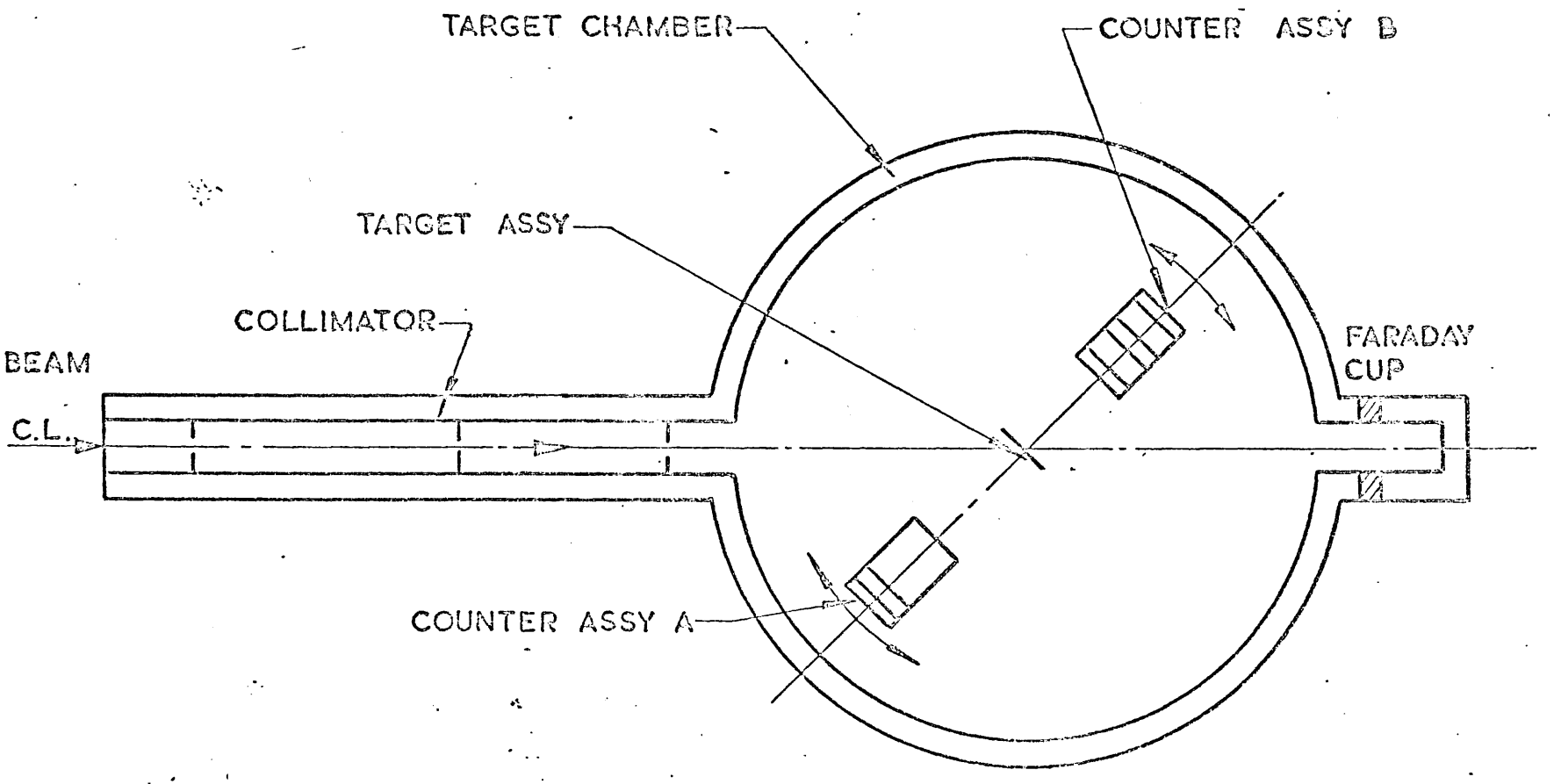

Fig: 4.3.1 Schematic diagram of an experimental set up with the scattering chamber.

In order to stop these low energy electrons reaching the detectors, small permanent magnets with field strength of ~ 1 KG were placed in front of both the telescope and the monitor. The field was strong enough to sweep away the electrons without effecting the heavier particles. With this arrangement an overall resolution of 90 to 100 KeV was obtained.

A block diagram of the total electronic counting system has been shown in the figure 3.4.1. The various scalers shown in the diagram were hooked to a master controller of Harwell type 1857B, which could be used for printing out the counts in all the scalers, starting and stopping all of them as necessary in single operation. In fact the master controller was also coupled to the current integrating system. A pre-set scaler was used to produce a signal when the bombardment of the target was completed for the required charge. This signal initiated the controller action which shut off the scalers and beam current. The beam current was cut off by using an electrically operated tantalum flap.

A PDP-8 computer interfaced to accept data from analogue to digital converters was used for spectrum analysis. This computer has 8k memory of 12 bit words, one teletype unit, two DEC magnetic tape transport, and a display with light pen facility. For operation of the computer in data acquisition mode, a display programme with interrupt facility was used. Whenever any data arrived from the ADC, the display was interrupted. The counting of the address advance in the interface unit was initiated by a start pulse from ADC. The number of address advance pulses give the channel address. On arrival of an accumulate pulse display was interrupted and one was added in the address registered.

This operation took about ~ 2μ-sec and so did not contribute significantly to the dead time of the system. The dead time was mostly due to conversion time in the ADC. For the Harwell ADC type 2011 with a conversion rate of 4 MHz, the dead time was one microsecond per four channel. Apart from this there was a dead time of 5μ-sec for every pulse rejected due to non-fulfilment of coincidence condition. The dead time estimate was obtained by gating a one mega-cycle clock (not shown in diagram 3.4.1) with the dead time output of the ADC unit. Similar system was used to register monitor dead time. In most of our uses the computer was used as two independent multichannel analysers with two ADC input each of 1024 channels. It could also be used in other modes such as 'one group with 2048 channels' or 'eight groups with 256 channels each' At the end of a run data was stored on DEC magnetic tape by using another programme. The data transfer rate to the magnetic tape was very high and it took only few seconds to transfer a spectrum of 2048 channels. About 45 such runs could be stored on a single DEC magnetic tape. At the end of the experiment data tapes were printed out on the line printer of Harwell IBM 360 central computer and written on IBM 7-track magnetic tape for subsequent analysis.

4.4 The Spectrograph Experiments.

The spectrograph system was used when resolution requirements were beyond the capability of the counter telescope system or to check the data obtained with the counter telescope system. Therefore in some cases the system was used as an alternative rather than in a complementary manner. The experiments were performed in lots of 2 to 3 days which are

refered to as runs hereafter. It was more efficient to use a single system in any one run due to time wastage involved in the beam line change.

The instrumentation aspect of the spectrograph system has already been described in section 3.5. The beam optics were similar to those described in section 4.2. A rectangular aperture 1mm high and 3mm wide, half a meter away from the target was used as collimating slit. A single 5mm x 5mm anti-scattering slit was used. The anti-scattering slit system was equiped with a paper roll device so that a burn mark could be used to check the beam spot dimension and alignments.

In order to use the system for experiments, detectors were positioned at required places along the focal plane from Kinematic consideration of the reaction to be studied. This positioning could be done only roughly, the exact limiting radii of the detectors were determined later by using either a ^{241}Am source or elastic scattering from a thin gold target. The gains of the E and E.x amplifiers were set up so that the full length of a detector could be accommodated in the 256 channels allocated to it. This was achieved by using elastic scattering from a thick target and setting up the magnetic field so as to provide a uniform spray of particles over all the counters and adjusting the gains until rectangles corresponding to full length of the detectors were observed in the spectra. The resolution of the detecting system was about ~ 30 KeV.

The required reactions were studied by setting up the magnetic field to required values from kinematic calculations, so that peaks were

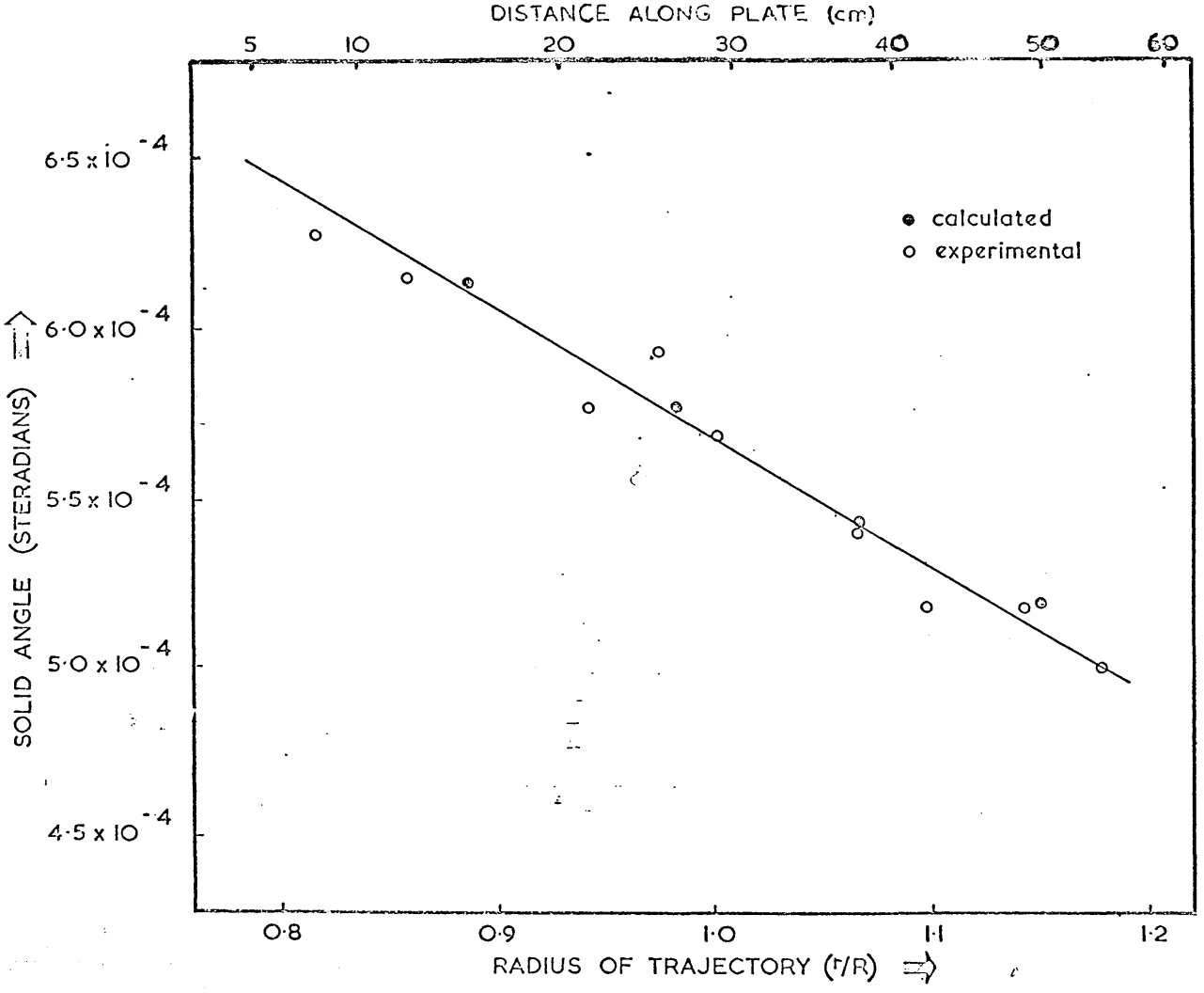

Fig: 4.4.1 Solid angle as a function of position along the plate.

positioned at the centres of the detectors. The magnetic fields were set by using a proton resonance field measuring probe. The required type of particle was chosen by setting up the energy conditions as explained in section 3.5. The use of the PDP-8 computer for data acquisition was parallel to the description in section 4.3.

A solid state detector was used at 60° to the beam direction to monitor the target during the experiments. The elastic scattering from the target seen by monitor was used to correct the changes in target thickness arising either from evaporation or change in the target orientation. The monitor was also used for normalization purposes when the integrated beam current measurement were not available, which occurred for studies at angles less than 15° when the Faraday Cup had to be removed to avoid obstruction of the spectrograph aperture.

Corrections had to be applied to the data from the spectrograph system due to changes in solid angle along the focal plane. This was done by using the calibration curve shown in the figure 4.4.1. The quantity 'R' in the figure refer to mean radius which was taken as 50 cm.

4.5 Multigap Spectrograph Experiments.

The Harwell multigap spectrograph has been described in section 3.6 where the reason for the use of the system was also pointed out.

The beam optics used in the multigap experiments were different from the description in section 4.2 in several ways. No-collimating slits were used at all in this case. The machine slits were set to the dimensions 0.060" inch high x 0.040" inch wide. The magnetic quadrupoles

were used to produce an image of the machine slit on the target with a magnification of ½ in the vertical direction and one in the horizontal direction. The field adjustments of the quadrupoles were done by positioning a 0.020" x 0.040" slit at the target position, four sides of which were insulated from each other and each could be connected to a current monitoring device. It was possible to obtain field settings for the quadrupoles by trial to get a transmission better than 90% through the slit. Once the beam geometry was set up, the slit was replaced by the target. This could be done without breaking the vacuum by sliding the target assembly which could hold many targets using a stepping motor device. The positioning of the target could be done accurately to within a few thousandths of an inch.

The detectors used were Ilford L4 emulsion plates of 50 micron thickness. Polythene absorbers of 0.015" thickness were used in front of the emulsion plates. The effect of the absorbers was to stop the deuterons in the emulsion which made it possible to distinguish the deuterons from the protons which were not stopped in the emulsion.

The magnetic field was set in each experiment so that the first required group arrived in the first gap, at least 10 cm from the top end of the emulsion plate.

A solid state detector was used to monitor the target condition by looking at the elastic scattering. The problem of target deterioration does not arise in multi-gap experiments because all the gaps are equally affected by any change in the target condition.

A routine procedure was used to process the plates before scanning. The scanning of the plates were done in ¼mm strips, only in selected places from the knowledge of the energy levels of residual nucleons and Kinematics considerations.

The only correction needed for the data was the solid angle variation along the focal plane. This correction along with the transformation to the centre of mass system was achieved by using a computer programme (c.f. Appendix B).

4.6 Time of Flight Experiments.

The time of flight system was used to study the $^{29}Si(d,n)^{30}P$ reaction. The instrumentation for the time of flight experiments had already been described in section 3.7. Two detectors with pulse shape discrimination were used in the experiments. One of the detectors was used for angular distribution measurements and the other was set at a fixed angle (15^{o} to the beam direction) to monitor the target condition. The detector used in the angular distribution measurements had a scintillator (NE213) of 4" inch diameter and 1" inch thickness. The monitor detector scintillator had 2" diameter and 1" thickness.

An illustration of the time of flight set-up is shown in the figure 4.6.1. The cylindrical target in the picture was absent in our case. The target used in the experiment was ~ 100 $\mu g/cm^2$ thick (^{29}Si) made by evaporation on a 0.05" thick gold backing and placed at the end of the beams line in a rotating can which was cooled by a stream of compressed air.

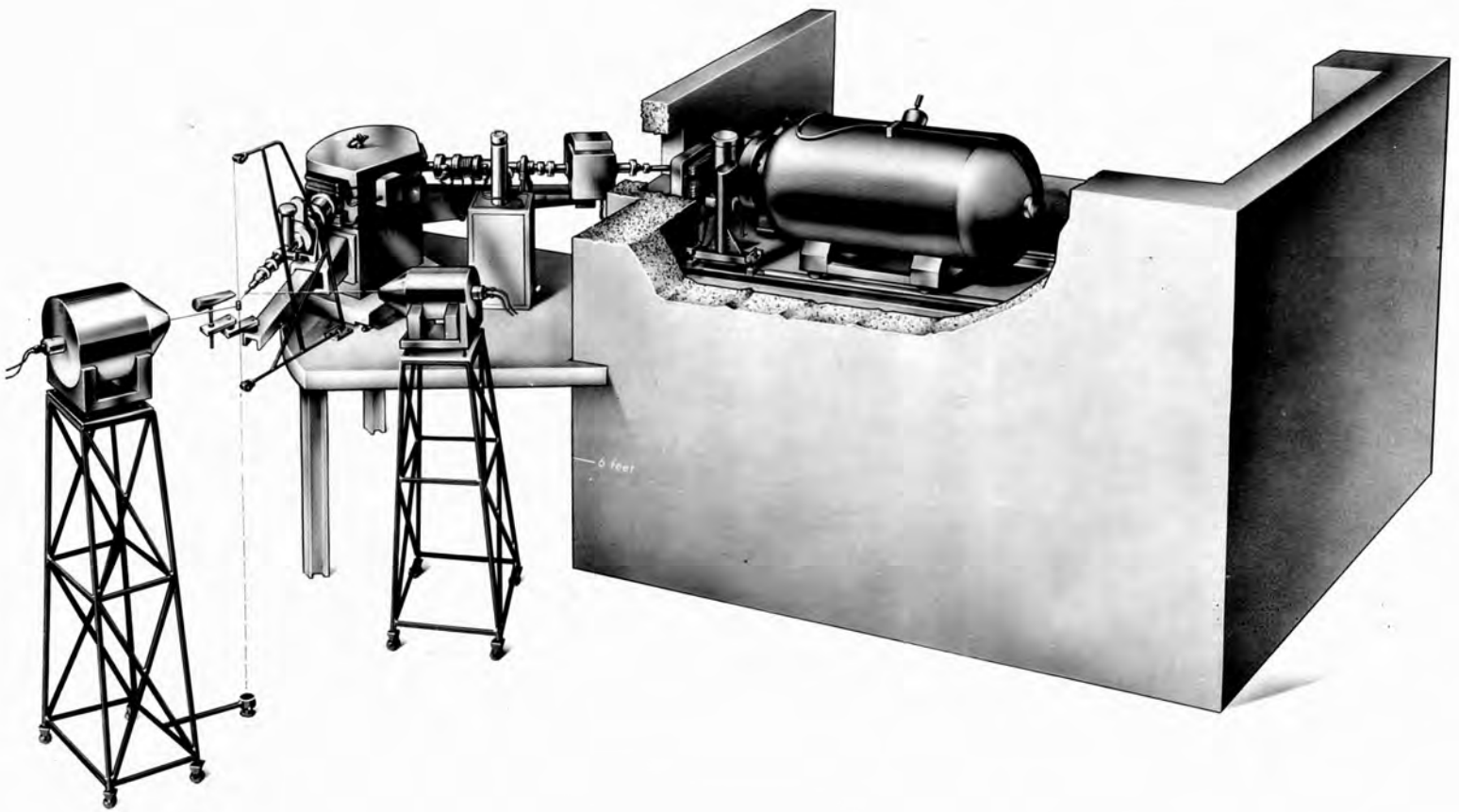

Fig: 4.6.1 **3 MeV PULSED VAN DE GRAAFF at HARWELL**

Before the experiments, linearity checks were done on the instrumentation system using the "white spectrum method". In this method start and stop pulses were generated from the random events in the detector due to an ^{241}Am source and a one Mhz clock respectively and the parameters in the electronic set up were adjusted until a flat time spectrum was obtained. Figure 4.6.2 shows a typical white spectrum. Apart from very low pulse height region a linearity better than 1% was achieved. As the experiments were in the linear region, the low pulse height non-linearity was of no consequence.

The flight path used was about ~ 6 meters for both the detectors. The angular distributions were obtained by rotating the larger detector around the target. In order to keep the distance between the target and the detector fixed, the base of the rotatable counter tower was fixed to a steel bar which pivoted about a point directly below the target (obtained by droping a plumb line). The angular positions were determined from permanent markings on the floor which are believed to be accurate within $\pm \frac{1}{2}^{o}$. The best time resolution obtained was better than 4 ns. A neutron time of flight from $^{29}Si(d,n)^{30}P$ is shown in the figure 4.6.3.

Corrections due to variation in the efficiency of the detectors were applied in the determination of angular distributions using the calibration measurements by Adams (Ad69). The relative efficiency curve is shown in the figure 4.6.4.

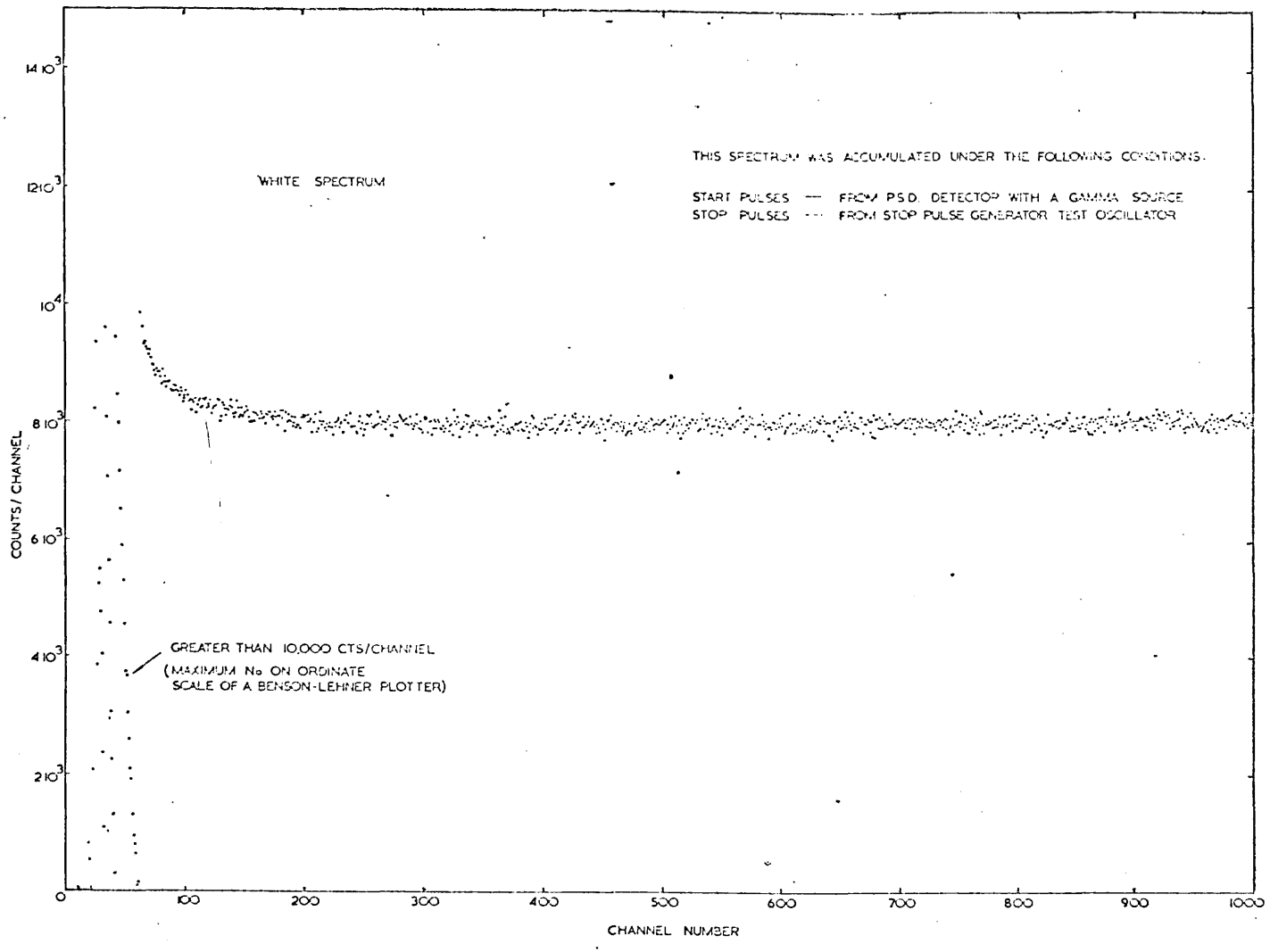

Fig: 4.6.2 A white spectrum

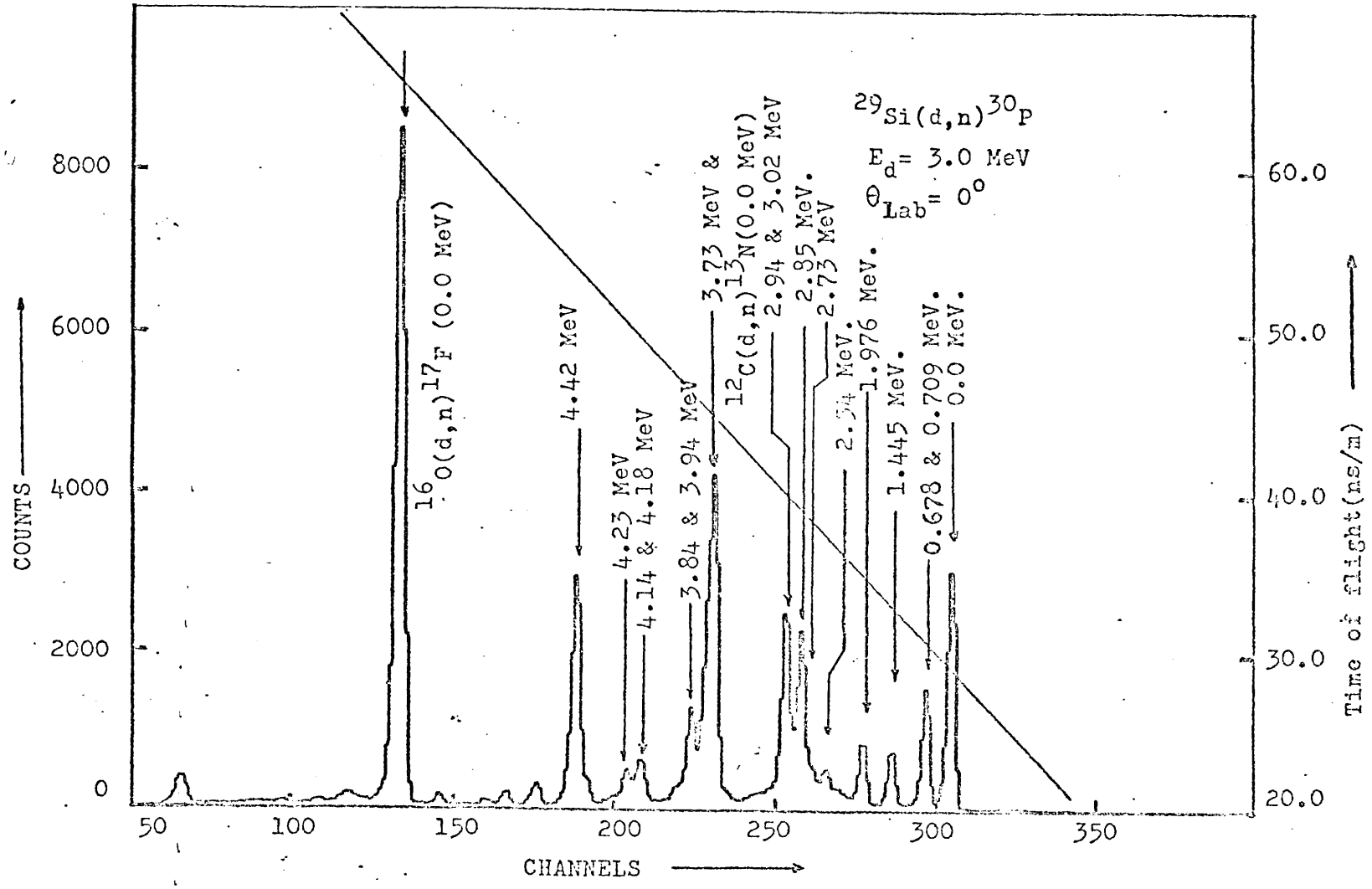

Figure:4.6.3 A time of flight spectrum from $^{29}Si(d,n)^{30}P$ reaction.
(Flight path ~6 meter)

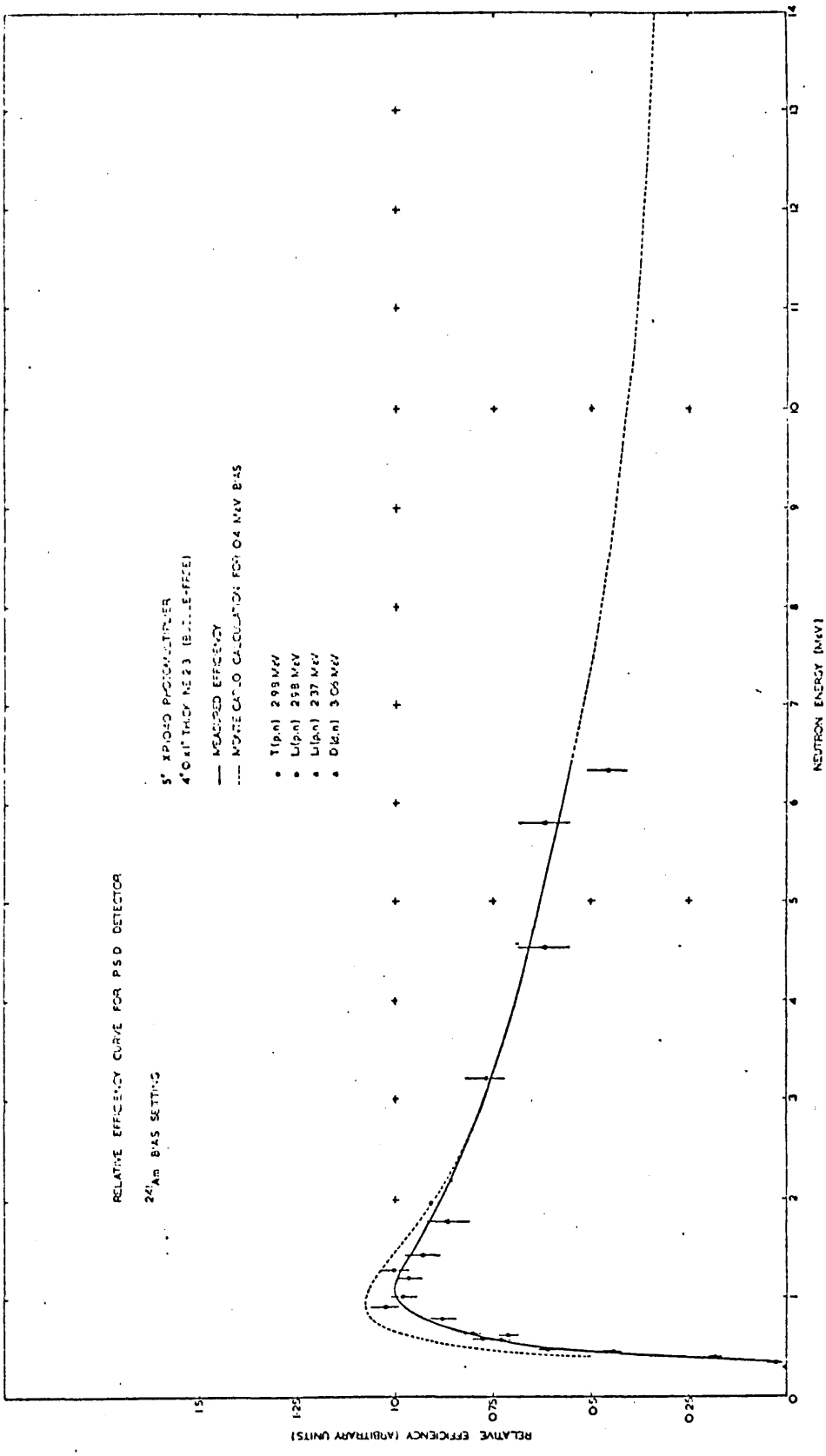

Fig. 4.6.4 Relative efficiency of neutron detector with pulse shape discrimination at ^{241}Am bias.

4.7 Cross-Section Calculations

For the cross-section calculation purpose, an essentially parallel beam was assumed to strike the target. The differential yield measured by the detector is given by

$$dY(\theta) = N_0 \, n \, \varepsilon \, \sigma(\theta) \, d\Omega \qquad (4.7.1)$$

where N_0 = Number of particles in the beam

n = Atomic density of the target

ε = efficiency of the detector

$\sigma(\theta)$ = differential cross-sections

$d\Omega$ = solid angle subtended by the detector at the detector.

The experimental results were essentially measurements of $dY(\theta)$ for known values of No which was measured by monitoring the integrated beam. The problems of beam monitoring have already been dealt with in section 4.2. The quantities nt $d\Omega$ were eliminated from the equation by Rutherford scattering measurements. The Rutherford yield is given by:

$$dY_R(\theta_R) = Nn \; \varepsilon \sigma_R(\theta_R) \, d\Omega \qquad (4.7.2)$$

where the symbols have parallel meaning to 4.7.1. Combination of two equations yield

$$\sigma(\theta) = \frac{dY(\theta)}{d\,Y_R(\theta_R)} \times \frac{N}{N_o} \times \sigma_R\,(\theta_R) \qquad (4.7.3)$$

The Rutherford cross-sections being known $\sigma(\theta)$ could be calculated. The cross-sections thus calculated were transformed into centre of mass system for subsequent analysis. A computer programme was written for the calculations of the cross-sections and to effect the transformations to the centre of mass system (c.f. Appendix A and B).

The following precautions were taken in order to ensure the correctness of calculated $\sigma(\theta)$:

(i) Changes in the target thickness due to evaporation during the experiment were corrected by using a fixed monitor counter and looking at the elastic yield and normalising the yield to the value just before or after the Rutherford measurements.

(ii) Incorrect normalization of $\sigma(\theta)$ could arise from σ_R not being pure Rutherford. In fact σ_R's were taken to be optical cross-sections due to some reasonable parameters instead of pure Rutherford. The measurements of σ_R were made at several angles so that consistency checks could be made.

4.8 Data Analysis

In this section only generalities of the data analysis are considered, peculiarities associated to each technique were considered earlier in this chapter.

The experimental data were essentially spectra of particles consisting of a series of peaks. The first step in the data analysis was

to find the areas of the peaks. When the peaks were well resolved, this was done by using the light pen facilities of the PDP-8 and DDP-516 computers at the Nuclear Physics Division, Harwell. It was also possible to do simple straight line background subtraction in this process.

In the cases of overlapping peaks, a least square fitting computer programme (c.f. Appendix B) was used for the purpose. This programme fitted the overlapping peaks to a given line shape using a least square method and gave areas due to individual peaks at best fit. It was possible to do linear, parabolic or cubic background fit and subtraction with this programme.

The next step consisted of normalisation of the calculated peaks areas to a common charge exposure and correction of these areas due to target deterioration effect. The data so obtained were used for the cross-section calculations as described in section 4.7.

The centre of mass cross-section obtained from the cross-section programme were generally at irregular angular intervals. As it was convenient to have data at regular angular intervals for subsequent analysis in many cases, the C.M. cross-sections were found at required intervals for the necessary cases by interpolation using a Legendre Polynomial least square fitting computer programme (c.f. appendix B). In some cases satisfactory fits could not be obtained using the above method and free hand fitting was used.

The next step in the data analysis consisted in fitting the data to the theories. In the case of elastic scattering, the optical model fitting is described in detail in chapter V.

For the transfer reaction cases DWBA fittings were done to the experimental angular distributions to extract the spectroscopic factors. In the pure cases, i.e. the cases where only one orbital angular momentum transfer was allowed, the spectroscopic factors were found by matching the first experimentally observed peak in the angular distributions to the DWBA cross-sections.

In the cases where more than one orbital angular momentum transfer was allowed, a computer programme (c.f. Appendix B) was used for decomposition of the distribution into its components. In this work composite distributions were due only to ℓ = 0+2 transfers. Three typical cases of decompositions are shown in figure 4.8.1. In the pick up cases data were not available at angles near zero-degree where ℓ=0 distributions are characterised by their large cross-section. So the spectroscopic factors found using the decomposition procedure were not very accurate. For the stripping cases the maximum DWBA cross-section for ℓ=2 transfer is typically an order of magnitude smaller than the maximum DWBA cross-section for ℓ=0 transfer. This gives rise to large uncertainty in the spectroscopic factors for ℓ=2, extracted by using the fitting procedure. As even the pure distributions did not fit very well with the DWBA calculations for $\theta_{cm} \geq 40^{o}$, it was not possible to estimate accurately the variance on the spectroscopic factors extracted by the fitting procedure. For the stripping cases estimates show that the ℓ=0 spectroscopic factors are quite accurate but the ℓ=2 spectroscopic factors are accurate within a factor of 2.

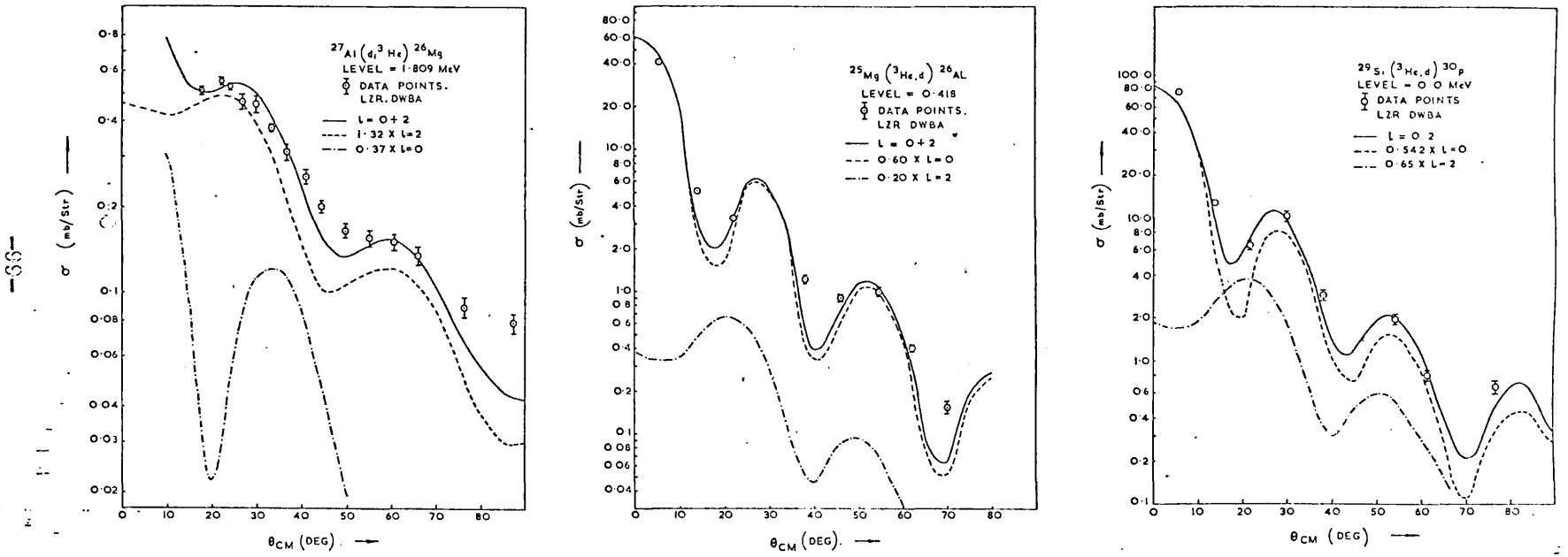

Fig. 4.8.1 Some typical cases of decomposition of composite angular distributions.

Uncertainties in the spectroscopic factor arising from the ambiguities in the decomposition are not shown in the tabulations of spectroscopic factors.

4.9 Errors and Their Evaluation

There are various sources of error in a scattering experiment. The importance of different errors depends on the geometry of the experiment. Some of the common errors are

1) statistical error.
2) error due to finite angular opening of the counter
3) error due to size of the beam spot.
4) errors due to multiple scattering in absorbers
5) errors due to slit system used.

Statistical error are there in common with all the counting processes. It is particularly serious in cases of overlapping peaks and peaks with high background. Standard procedure was adopted, to evaluate them. The statistical errors are not shown in the tabulation of the spectroscopic factors unless they are greater than 10%.

Error due to finite angular opening of counters are important where cross-section vary very rapidly with angle. This is a second order effect because linear change cancels each other on two sides of central angle. This could be important in our counter telescope system for elastic scattering at forward angles because of its rather large angular opening but this system was not used at very forward angles. For spectrograph experiments this was not very important because of

its very small angular opening.

Beam spot dimensions in all our experiments were very small compared to the distance of the counter from the target so that error due to beam spot size was unimportant.

It might be suspected that the error due to multiple scattering in the ΔE counter, in the telescope experiments may be significant. However, calculations show that even in the worst case $\langle\theta\rangle_{av.}$ was less than 2 degrees. Counters in the telescope were arranged without any collimating slits between E and ΔE counters, so that there was no counting loss due to this effect.

Error due to slit edge penetration is unimportant for energy measuring experiments because this effect shows up in energy change and is automatically eliminated.

Other errors arising in specific cases are discussed in relevent places. Examples of these type of errors are: errors in peak areas due to overlapping of peaks, errors in target thickness, errors in the spectroscopic factors arising from decomposition into components etc.

CHAPTER V

ELASTIC SCATTERING STUDIES

5.1 Introduction

The utility of optical potential parameters in our studies has already been pointed out in section 2.5. It was also noted that deuteron and ^{3}He optical potentials show a few ill defined systematic variations and so it is not quite safe to extrapolate potentials from neighbouring nuclei and even from the same nuclei at different energies. So it was decided we should evaluate the necessary optical parameters as much as possible in order to reduce the vagaries in DWBA associated with optical parameters. In practice measurements were limited to targets on which other studies were done as well.

Deuteron elastic scattering angular distributions were measured at an incident energy of 12.0 MeV for targets ^{40}Ca, ^{45}Sc and at an incident energy of 13.0 MeV for targets ^{37}Cl, ^{35}Cl, ^{27}Al and ^{23}Na.

Angular distributions of ^{3}He elastic scattering cross-sections on ^{25}Mg and ^{29}Si were measured at an incident energy of 14.0 MeV.

5.2 Data

The Experimental methods used were those described in sections 4.3 and 4.4. Both the counter telescope and the spectrograph systems were used in (d,d) studies. The counter telescope could not be used at forward angles due to worsening resolution from high count rate and progressive smallness of the kinematic shift which made the resolution of the impurity groups impossible. At forward angles the spectrograph system was used. This also provided an independent check on the normalisation. Even with the spectrograph system it was not possible to explore forward angle less than 25^{o} for ^{45}Sc and ^{23}Na and 20^{o} for chlorine due to the presence of impurity groups and the target thickness effect. Errors in cross-sections are quite high even at these angles due to overlapping of peaks. For (^{3}He,^{3}He) cases spectrograph was used because it was not considered worthwhile to change the beam line as some checks on (d, ^{3}He) reactions were also being made on the same run. The composition of the targets used have already been described in table 4.2.1.

Figures 5.2.1 show some representative counter telescope spectra obtained in experiments to determine (d,d) cross-sections. Figure 5.2 shows a typical position sensitive detector spectrum. The rather poor resolution in the figure was due to target thickness. Absolute normalisations for (d,d) cases were obtained by comparing the cross-sections with elastic cross-sections at 4.0 MeV, by taking the cross-sections to be due to some reasonable optical potential rather than pure

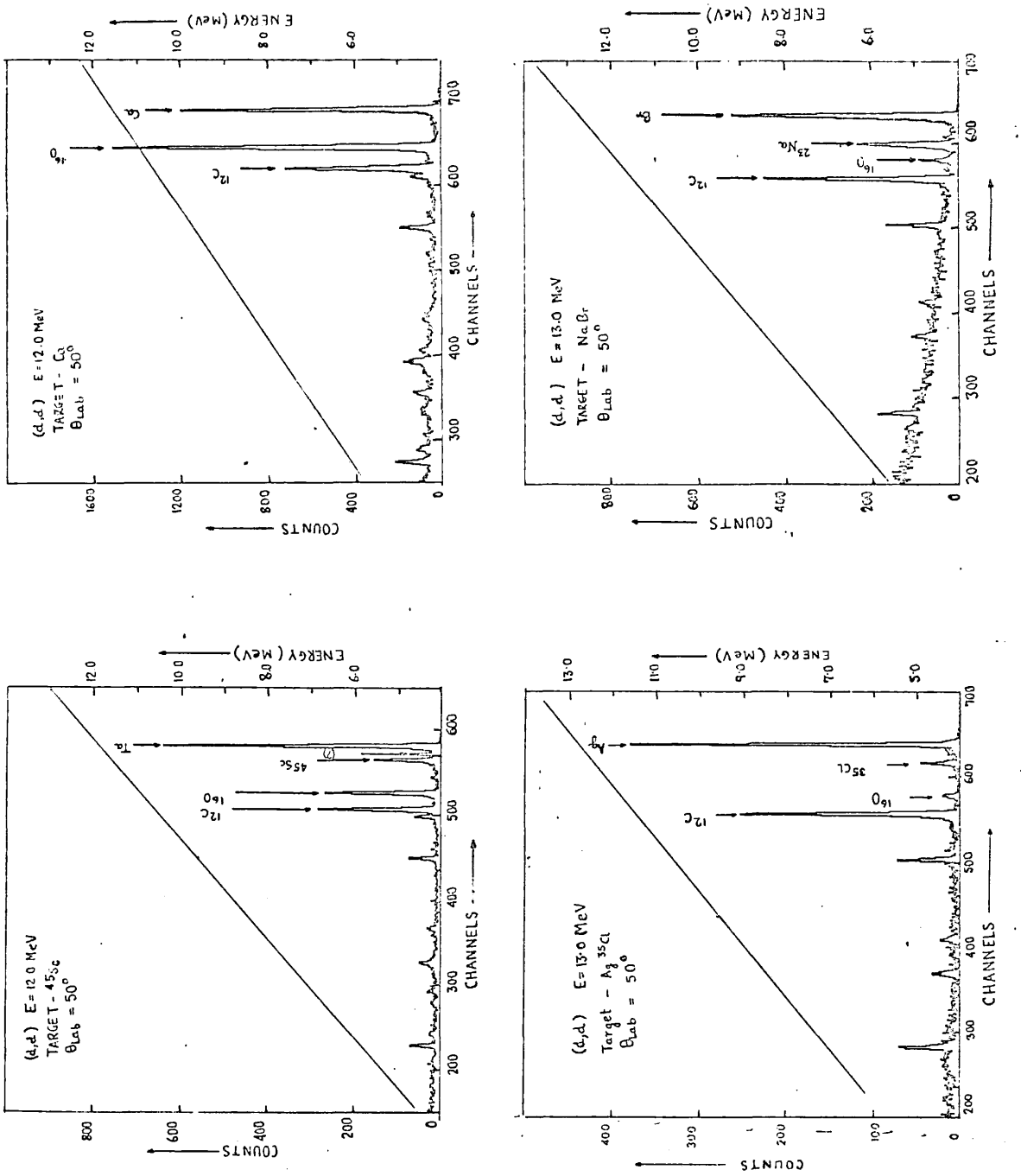

Fig: 5.2.1- Some representative elastic scattering spectra.

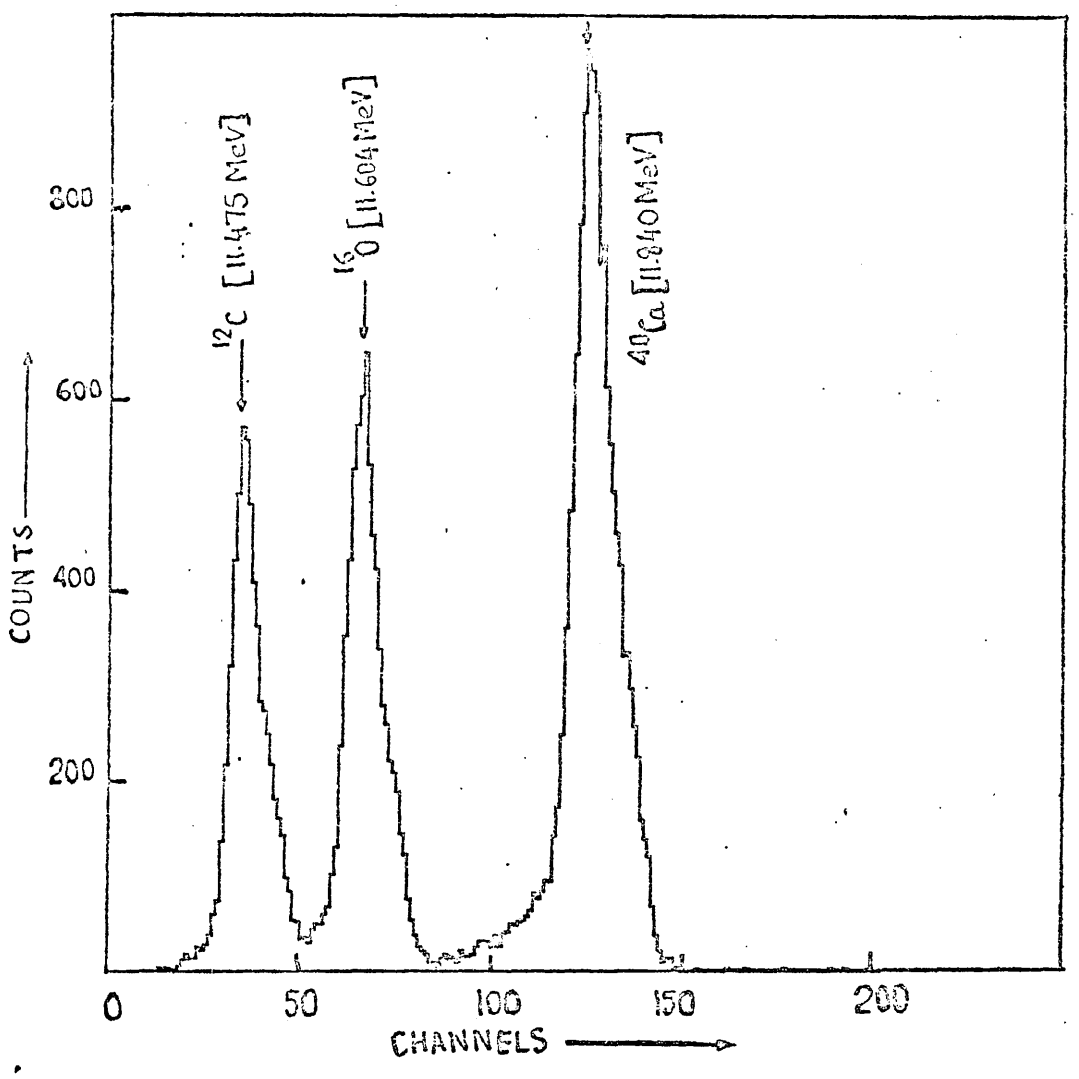

Fig: 5.2.2 A typical position sensitive detector spectrum ($\theta_{Lab} = 30^{o}$) from $^{40}Ca(d,d)^{40}Ca$ at Ed=12.0 MeV.

Rutherford as pointed out in section 4.7. After the evaluation of the final potentials checks were made on these corrections using the final potentials which showed the goodness of the approximation. Procedure for finding absolute normalisation for (^{3}He, ^{3}He) cases are mentioned in each case under consideration.

General aim was to keep statistical error less than 3%, which was taken as the criterion of good statistics. However in some cases errors turned out to be larger than this.

5.3 Methods of Analysis

The method of finding optical potential for a given data set consists in varying the parameters of the optical potential until the difference between the calculated and measured cross-sections is as small as possible. A convenient measure of this difference is the quantity

$$\Delta = \sum_{N} \left(\frac{\sigma_E - \sigma_T}{\delta\sigma_E} \right)^2$$

where σ_T and $\sigma_E \pm \delta\sigma_E$ are the calculated and experimental cross-section at a particular angle and the summation runs over all the N experimental points. This quantity may be minimised by systematic parameter variation using an appropriate computer programme. In this way a satisfactory fit to the experimental data may usually be found, with some exceptions to be discussed in the following sections.

The results of the analysis of a particular set of experimental data depends on the number of parameters of the potential that are allowed

to vary. The number of parameters to be varied depends on the type of analysis required.

If the object is to obtain as good a fit to a set of data as possible, then this will be achieved by varying all the parameters. If it is desired to obtain the best overall fit to a range of nuclei then it is more appropriate to vary a few parameters only.

Even when the variable parameters have been selected according to the aim of the analysis, it is not necessarily best to vary them all at once, as some times this gives rise to ill determined equations for optimum parameter shifts and hence to erratic behaviour of the automatic search routine. It may be better to vary the parameters 2 or 3 at a time until the best fit is found. No general rules can be given for this as it depends very much on the peculiarities of the particular experimental data.

It is usual to start the process with parameters that have already been found to give a good fit to data on similar nuclei at similar energies. However, if the calculations are started with markedly different parameters it is frequently found to converge to quite a different set of parameters. Thus, there may be more than one optical potential that gives an equally acceptable fit to a particular set of experimental data. It turns out that there are several distinct sets of parameter ambiguities. Some are continuous, so that all sets of parameters in a particular region of parameter space give equally good fit. Other ambiguities are discrete in the sense that only a series of particular values of the parameters give acceptable fits while intermediate values do not.

5.4 Types of Parameter Ambiguities

5.4.1 Normalisation ambiguities.

Experimentally measured cross-sections are subjected not only to a statistical error depending on the number of particles counted at each angle but also an overall normalisation error depending on the calibration of the detecting apparatus and thickness of the target. It is only the statistical error that is taken into account in calculating Δ, but even if the normalization error of the order of 5% is added to $\delta\sigma$, the uncertainty in the cross-sections, the ambiguity still remains.

Dickens and Perey [Di65] analysed data on elastic scattering of 12 MeV deuterons by Ni, Zr and Cd using different normalizations. Their results showed that some parameters are quite sensitive to the normalization factor.

It is possible to determine the normalization factor by allowing it to be one of the parameters that is varied to optimize the fit, but experience shows that this is not reliable and usually introduces a substantially additional uncertainty in the values of the optical model parameters. For elastically scattered particles, the coulomb field dominates the scattering at small angles and this fact can be used for normalization of the cross-sections. However in this region the cross-section is both large and varying very rapidly with angle, so it is not easy to measure it with the necessary precision. Indeed, it is usually the case that the accuracy in normalisation obtained by this method is similar to the accuracy obtainable by the technique of absolute measurement. The presence of the normalisation ambiguity show the importance of the accurate measurement of absolute cross-section.

5.4.2 Valley Ambiguities

The value of Δ may usefully be thought as defining a surface in space with as many dimensions as there are variable parameters plus one. The best fit corresponds to the deepest minimum and the presence of ambiguities imply that there are several such minima. In practice it is often found that a minimum is very broad and shallow, so it is possible to vary several parameters at once in a particular way without significantly varying Δ. The more accurate the spectroscopic data the more restricted are the areas of allowed parameters. Some times a minimum is broad and shallow in one direction and steep in the other so that region of best fit corresponds to the floor of the narrow valley. This implies that the fit remains unaltered if say just two parameters are varied in a special way together. An example is the Ur_u^n ambiguity, in which the fit remains almost the same if r_u is varied as much as 10% either way from its optimum value provided U is varied at the same time so that Ur_u^n remains constant. Similar ambiguity involving W and a_w has also been noted [Ho66].

5.4.3 Potential Depth Ambiguities.

These have already been discussed in sections 2.5, where it has been pointed out that there are a series of potential depths to which elastic scattering can be fitted.

5.4.4. Form Factor Ambiguities.

It is possible to obtain good fit to deuteron and ^{3}He elastic scattering with wide range of potential forms. This range may be greatly reduced by the physical conditions but there still remains many forms that are equally acceptable purely from the point of view of fitting data.

For example excellent fits can be obtained using either volume or surface absorption potentials for a series of potential depths [PE63, Ho66]. Even reaction cross-sections remain substantially the same. So, it is not possible to distinguish volume and surface absorption by measuring this quantity.

The ambiguities associated with different form factors are usually dealt with in practice by choosing one form and using it consistently. If this is done analyses of different sets of data are all comparable and the variations of parameters may be interpreted physically. All the results that are obtained using one equivalent form could also be obtained with any of the others.

5.5 Results and Discussions

The figures 5.5.1 show the experimental cross-sections together with the optical model fit. The data points where no error bar has been shown means that errors come within the circles.

In order to evaluate the optical model parameters a programme due to Wilmore [Wi69] was used. Errors in the data points were the actual statistical errors of the experimental data. We shall now briefly discuss the case of each of the nuclei studied.

$^{29}Si(^{3}He, ^{3}He)^{29}Si$

This reaction has previously been studied by Zurmühle [Zh68] at 15.0 MeV. This study was conducted at 14.0 MeV to obtain optical potential for DWBA studies of ^{29}Si $(^{3}He, d)^{30}P$ which has also been studied at the same energy. The statistics were good and the angular region covered was adequate. Absolute normalisation of the cross-sections

was done by taking the cross-section at 20^{o}(Lab) to be equal to the optical model cross-section due to the potential by Zurmühle shown in table 5.5.1. Data point at 20^{o} was chosen because this was the smallest angle where the impurity groups were well resolved. The value of this normalising cross-section is in good agreement with the cross-section calculated with the final potential after the search.

The same potential by Zurmühle was also used as the starting potential for the optical model search. Initially a four parameter search (U, a_u, W, r_w) was carried out on the argument that, as the initial potential is for the same nucleus at comparable energy only a small variation in the parameters would be needed so that (U,r_u) and (W,a_w) ambiguities will be operative. However it was found that the fit about 50^{o} (CM) was not good, so a five parameter (U,a_u,W,r_w,a_w) search was carried out which gave an improved fit. The logic for a 5 parameter search being, whereas (U,r_u) ambiguity is known to be operative for ~ 10% variation in U, the range of (W,a_w) is not so well known. Actual experimental errors on the data points were used in the search in order to avoid fitting some points at the cost of some others. Search was carried out also by using 5% errors on all data points which gave a comparable fit. The angular distribution with optical model fit is shown in fig. 5.5.1, the final potential parameters are shown in table 5.5.2.

$^{25}Mg(^{3}He,^{3}He)^{25}Mg$

The reaction has previously been reported at 33.0 MeV by Dehnhard [Dh67]. This study was conducted at 14.0 MeV to find optical potentials for use in DWBA studies of $^{25}Mg(^{3}He,d)^{26}Al$. Both statistics and angular range coverage of data were good. Absolute normalisation has been obtained by taking the cross-section at 15^{o}(Lab) to be due to potential by Dehnhard. Like the ^{29}Si case cross-section calculated with final potential at this angle agrees very well with the values used.

Due to reasons already pointed out in ^{29}Si case a four parameter (U,a_u, W,r_w) search was carried out using the potential by Dehnhard shown in table 5.5.1. Final potential after search is shown in table 5.5.2. The rather large value of Δ is due to a single point at 22.36^{o}(CM) which for some unknown reason turned out to have a very large value. The angular distribution with optical model fit is shown in figure 5.5.1.

$^{45}Sc(d,d)^{45}Sc$

This study has been conducted at 12.0 MeV for use in DWBA for $^{45}Sc(d,^{3}He)^{44}Ca$ reaction. On previous study on this reaction has been reported by Hansen [Ha68], the potential parameters from which is shown in table 5.5.1.

The quality of data was not good and the coverage of angular range was also rather small. The poor quality of data was due to the presence of large amounts of tantalum and another heavier than ^{45}Sc but less massive than Ta unidentified impurity group in the target. Normalization procedure

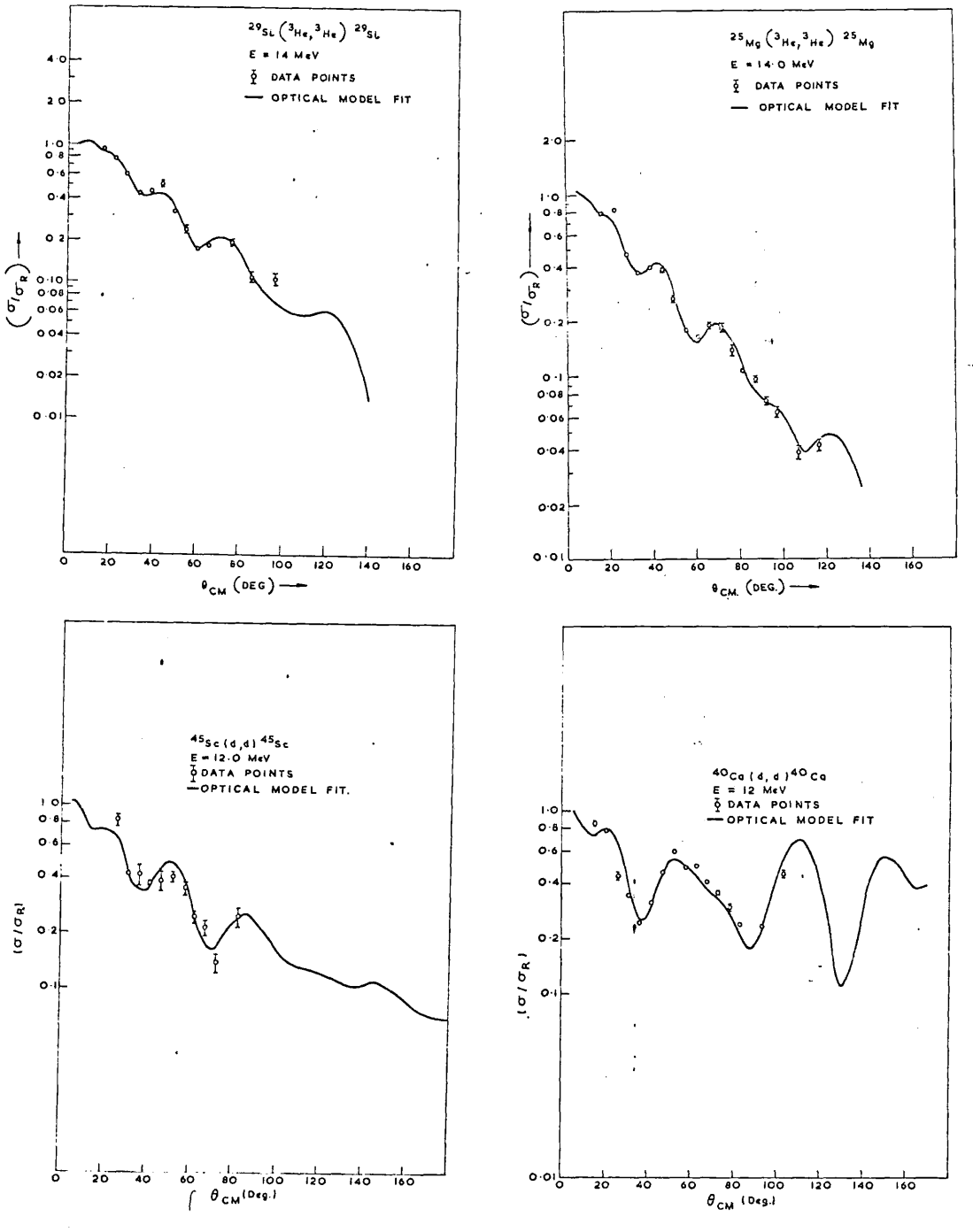

Fig: 5.5.1 Elastic scattering angular distributions with optical model fit.

Table 5.5.1 Initial Potential used in Optical Model Search

Reaction	U MeV	r_u fm	a_u fm	W* MeV	r_w fm	a_w fm	E MeV	Parameters Varied	Comments
$^{29}Si(^3He,^3He)^{29}Si$	173.0	1.25	0.63	17.06 S	1.580	0.78	15.0	U,a_u,W,r_w,a_w	^{29}Si potential [Zh68]
$^{25}Mg(^3He,^3He)^{25}Mg$	167.1	1.10	0.688	20.5 S	1.668	0.75	33.0	U,a_u,W,r_w	^{25}Mg potential [Dh67]
$^{45}Sc(d,d)^{45}Sc$	113.7	1.0	0.785	12.96 D	1.418	0.64	7.5	U,a_u,W,r_w	^{45}Sc potential [Ha68]
$^{40}Ca(d,d)^{40}Ca$	93.5	1.168	0.791	21.55 D	1.477	0.428	12.1	U,a_u,W,r_w	^{40}Ca potential [Ry63]
$^{37}Cl(d,d)^{37}Cl$	112.8	1.021	0.846	19.8 D	1.47	0.444	12.0	U,a_u,W,r_w,a_w	^{40}Ca potential [Pe63]
$^{35}Cl(d,d)^{35}Cl$	112.8	1.021	0.846	19.8 D	1.47	0.444	12.0	U,a_u,W,r_w,a_w	^{40}Ca potential [Pe63]
$^{27}Al(d,d)^{27}Al$	103.0	1.0	0.943	29.6 D	1.501	0.527	10.95	U,a_u,W,r_w	^{27}Al potential [Sa65]
$^{23}Na(d,d)^{23}Na$	108.9	1.0	0.881	25.37D	1.507	0.527	13.0	U,a_u,W,r_w,a_w	^{27}Al potential (this work)

*The letters S and D in the imaginary potential parameter column refer to Saxon-Wood and Saxon-Wood derivative form factors. This convention is followed throughout this work.

described in section 5.2 was used for obtaining absolute values of the cross-sections.

The parameters by Hansen was taken as the starting for a four parameter search (U,a_u,W,r_w). The angular distribution together with the optical model fit is shown in figure 5.5.1. The fit could be improved by decreasing the errors on the data but this was not considered desirable because of the ambiguity it introduces in the parameters found. The final potential parameters are shown in table 5.5.2.

$^{40}Ca(d,d)^{40}Ca$

Cross-section for elastic scattering of deuterons on ^{40}Ca has been measured and optical potential extracted on numerous occasions [Ho66]. Targets used in our measurements was natural calcium (abundance of ^{40}Ca = 96.97%). Statistics of the data is fairly good but normalization for target thickness change was inaccurate at angles greater than 70^{o} due to accidental loss of monitor spectra. So the normalization for these angles was done by using total integrated monitor count which was recorded on a scalar which was obviously not very satisfactory and a bulge in the angular distribution can be seen corresponding to the beginning of this region around 70^{o}. To get the absolute values of the cross-sections procedure in section 5.2 was adopted.

The potential by Raynal [Ry63] which is shown in table 5.5.1 was used as the starting potential for a four parameter (U,a_u,W,r_w) search. Due to the normalization problem mentioned above, the aim had been to get a reasonable fit with a potential close to the starting one and too good a fit was avoided. The final potential is shown in table 5.5.2. The angular distribution along with optical model fit

is shown in figure 5.5.1.

$^{37}Cl(d,d)^{37}Cl$ and $^{35}Cl(d,d)^{35}Cl$

Deuteron elastic scattering from either of these nuclei has not been reported. Our studies were conducted at 13.0 MeV. Targets used were same as those shown in table 4.2.1.

The quality of data was not good and angular range coverage was also small. In the absence of optical potentials for these nuclei, the starting potential for optical model search used was that by Perey (Pe63) for ^{40}Ca which is shown in table 5.5.1. In both cases five parameter (U, a_u, W, r_w, a_w) were carried out. Figures 5.5.2 show the fit to the data. The final potential parameters are shown in table 5.5.2.

$^{27}Al(d,d)^{27}Al$

Elastic scattering of deuterons from ^{27}Al has been studied on numerous occasions [Ho66]. Our studies were conducted at 13.0 MeV for use in DWBA for $^{27}Al(d,^{3}He)^{26}Mg$.

The starting potential used for optical model search is shown in table 5.5.1 which is due to Satchler [Sa65]. A four parameter (U, a_u, W, r_w) search was carried out. Figure 5.5.2 show the fit to the data. Final potential parameters are shown in the table 5.5.2.

$^{23}Na(d,d)^{23}Na$

Deuteron elastic scattering from ^{23}Na has not been reported previously. Our studies were conducted at 13.0 MeV.

The quality of data is not particularly good due to contaminants oxygen and carbon in the targets. The ^{27}Al potential evaluated in this

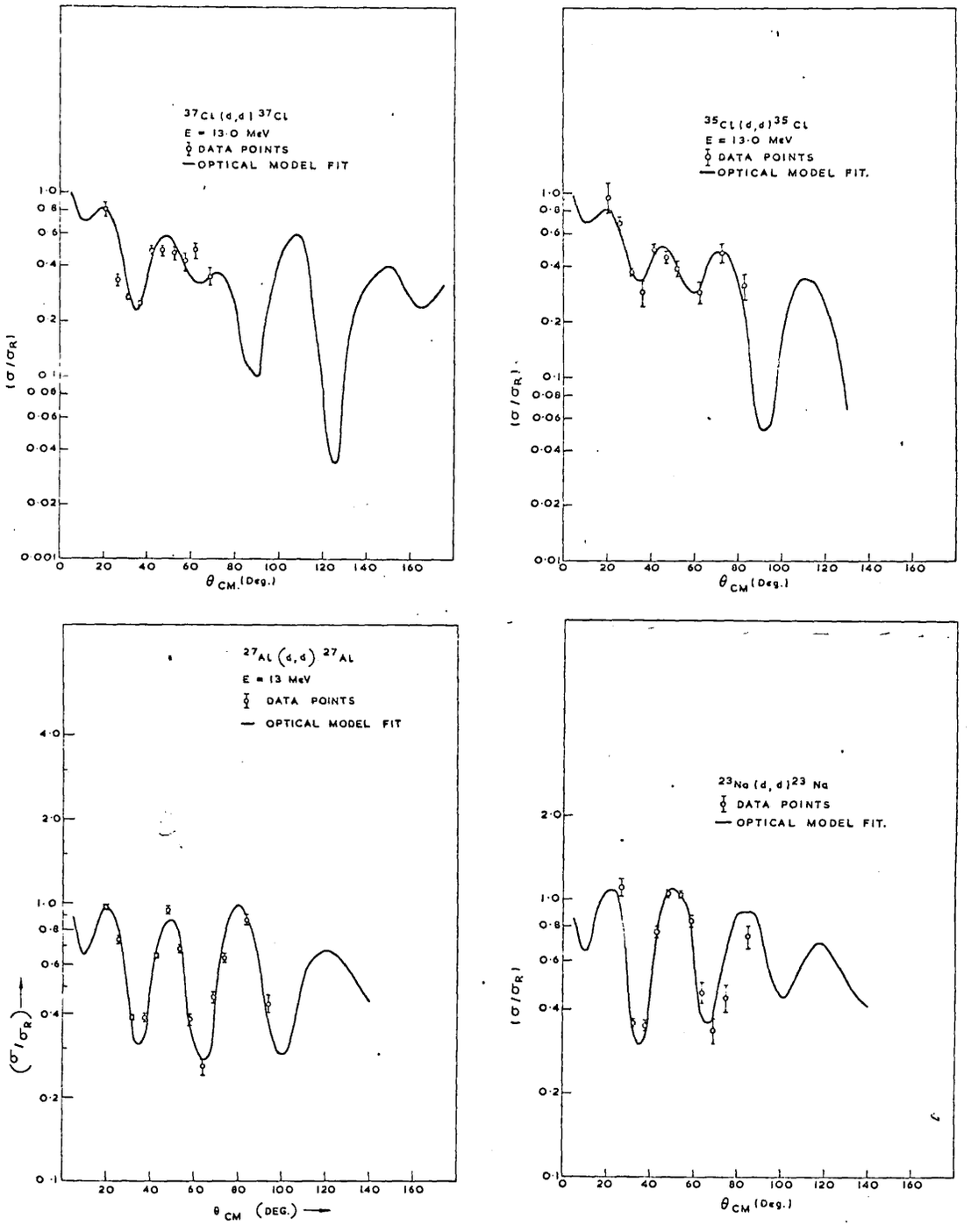

Fig: 5.5.2 Elastic scattering angular distributions with optical model fit.

Table 5.5.2 Optical Model Potentials Found to Fit Experimental Data

Reaction	E MeV	U MeV	r_u fm	a_u fm	W MeV	r_w fm	a_w fm	σ_R mb	Δ
$^{29}Si(^3He,^3He)^{29}Si$	14.0	188.99	1.25	0.601	25.25 S	1.327	0.813	1009.95	76.1
$^{25}Mg(^3He,^3He)^{25}Mg$	14.0	174.15	1.10	0.714	17.96 S	1.631	0.750	1101.35	262.0
$^{45}Sc(d,d)^{45}Sc$	12.0	120.69	1.0	0.770	27.28 D	1.138	0.684	1190.9	211
$^{40}Ca(d,d)^{40}Ca$	12.0	90.89	1.16	0.817	18.22 D	1.54	0.428	1206.0	254
$^{37}Cl(d,d)^{37}Cl$	13.0	113.34	1.021	0.844	15.92 D	1.44	0.578	1393.9	59.0
$^{35}Cl(d,d)^{37}Cl$	13.0	108.66	1.021	0.784	12.55 D	1.36	0.772	1397.8	19.9
$^{27}Al(d,d)^{27}Al$	13.0	108.8	1.00	0.8815	25.37 D	1.507	0.527	1287.5	61.0
$^{23}Na(d,d)^{23}Na$	13.0	80.73	1.0	0.92	37.53D	1.392	0.5826	1286.7	115

work was used as starting potential for five parameter (U, a_u, W, r_w, a_w) search. Fit to the data is not very good and there is a marked phase shift about 70^{o}. The fit to the higher angle could not be improved without changing the errors on the data points which for reasons mentioned earlier was not considered advisable. The final potential is shown in table 5.5.2. The fit to the data is shown in figure 5.5.2.

5.6 Conclusion

The differential cross-sections for elastically scattered deuterons were measured at a bombarding energy of 12.0 MeV from ^{45}Sc, ^{40}Ca and at 13.0 MeV from ^{37}Cl, ^{35}Cl, ^{27}Al, ^{23}Na. The differential elastic scattering cross-section for ^{3}He from ^{29}Si and ^{25}Mg were measured at a bombarding energy of 14.0 MeV. Optical potential parameters were extracted by fitting these, data for use in pick up and stripping reaction studies reported in chapters VI and VII.

CHAPTER VI

THE $(d,{}^3He)$ REACTION STUDIES

6.1 The $(d,{}^3He)$ reactions leading to ground states of ^{44}Ca, ^{39}K, ^{36}S and ^{34}S

6.1.1. Introduction

The equations for the direct reaction cross-sections (i.e. equations 2.3.11 and 2.3.12) contain a normalization factor 'N' arising from the overlap between the light particle wave functions which has already been discussed in section 2.3. As this occurs as a conjugate multiplicative factor with the DWBA cross-sections, a precise estimate of this factor is necessary in order to evaluate accurate absolute spectroscopic factors. For the zero-range DWBA calculations of $({}^3He,d)$ and $(d,{}^3He)$ reactions, the value by Bassel (Ba66) of 4.42 has been widely used but various other values both theoretical and experimental have been reported. As DWBA cross-sections are subject to variation with the choice of optical model parameters and bound state wave functions, the evaluation of 'N' is also subject to these vagaries.

Here an attempt has been made to evaluate the zero-range 'N' from the studies of (d, ^{3}He) transitions to the ground states of ^{41}Ca, ^{39}K, ^{36}S, ^{34}S. The deuteron channel optical potential has been evaluated at the correct incident energies for all these reactions which hopefully would minimise the ambiguities arising from this source. The optical parameters for the ^{3}He channel have been taken from the literature at close enough energies for the same nucleus or the neighbouring nucleus being studied. In any case the out going energies of the ^{3}He particles which are doubly charged are low, and the dominant contribution to elastic scattering is from the coulomb field and hence the calculations should be stable against small variations in the ^{3}He parameters. It is hoped to minimise the bound state ambiguity by using a constant prescription throughout.

Of course tests and comments will be made on the reliability or otherwise of the values obtained. Some discussions will also be made on the individual transitions. A brief review of the past work on the normalization is included below.

6.1.2 Review of the past work on normalisation:

The table 6.1.1. summarises the experimental values of the normalization constant reported in literature.

Table 6.1.1

Summary of experimental values of normalization constant

Reaction	N	References
$^{54,56}Fe(^{3}He,d)^{55,57}Co$	4.4	Ro67a
$^{48}Ca(^{3}He,d)^{49}Sc$	4.17	Er66
$(^{3}He,d)$ on 28 neutron nuclei	3.7±0.6	Ar66
$^{40}Ca(d,^{3}He)^{39}K$	4.42	Hi67
	2.4±0.45	Yn64
	1.44	Cu62
$^{16}O(d,^{3}He)^{15}N$	4.42	Hi67
	1.45	Cu62

It can be seen from the table above that there is considerable scatter in the experimental values of 'N'. Many attempts have been made in order to evaluate the normalization constant theoretically as well. The table 6.1.2 summarises the theoretical values of D_o^2 (defined in equation 2.3.7) and 'N' evaluated using various prescriptions.

Table 6.1.2

Theoretical values of the normalization constant.

Theory	D^2 in 10^4MeV Fm^3	N	References
1. Hulthen Wave functions for both deuteron and ^{3}He.	2.34	3.45	[Th70]
2. Velocity dependent nucleon-nucleon potential, Hulthen function for deuteron, tri-nucleon wave function with 2% $^5S_1$ mixture.	3.13	4.68	[Li69]
3. Ohmura Wave function with hard core potential (r_c = 0.2 fm)	7.4	10.9	[Ro67]
4. Hulthen function for deuteron and Irving-Gunn for ^{3}He wave function	2.99	4.42	[Ba66]

The calculations by Rook [Ro67] are too sensitive to the parameters and the values are too large. The other three values are within 20% of the mean value 4.18. The values by Bassel [Ba66], it has been pointed out by Lim [Li69] is due to choice of a wave function for ^{3}He which has since been proved wrong. The value by Thompson [Th70] has been calculated using the same parameters for a number of reactions which gave agreement with the experimental values and hence possibly more consistent.

6.1.3 Data

The (d,^{3}He) transitions leading to the ground state of ^{44}Ca, ^{39}Ca, ^{36}S, ^{34}S were studied at an incident energy of 12.0 for the first two cases and at an incident energy of 13.0 for the last two cases. The experimental procedures adopted were the same as those described in the sections 4.3 and 4.4. Both the counter telescope and the spectrograph systems were used. For ^{45}Sc and ^{40}Ca targets the counter telescope was used to find the angular distributions which were checked at several angles with the spectrograph system. For the ^{37}Cl case only the spectrograph system was used. The case for the ^{35}Cl target has been described in section 6.2. The composition of the targets have already been described in the table 4.2.1.

The absolute normalizations for the (d,^{3}He) cross-sections were obtained by comparison with the elastic scattering cross-sections at 4.0 Mev which were assumed to be due to optical potentials as explained in sections4.7 and 5.2. There were contaminant problems with the ^{45}Sc target and the errors in the absolute cross-sections can be quite high. The absolute estimates for the other cases are believed to be correct within 10% . No correction for the isotopic abundances has been applied as they are only a few percent. The figures 6.1.1 (a,b,c) show the angular distributions, along with DWBA fits for the ground state transitions to ^{44}Ca, ^{39}K and ^{36}S. The ^{34}S case is shown in figures 6.2.1.

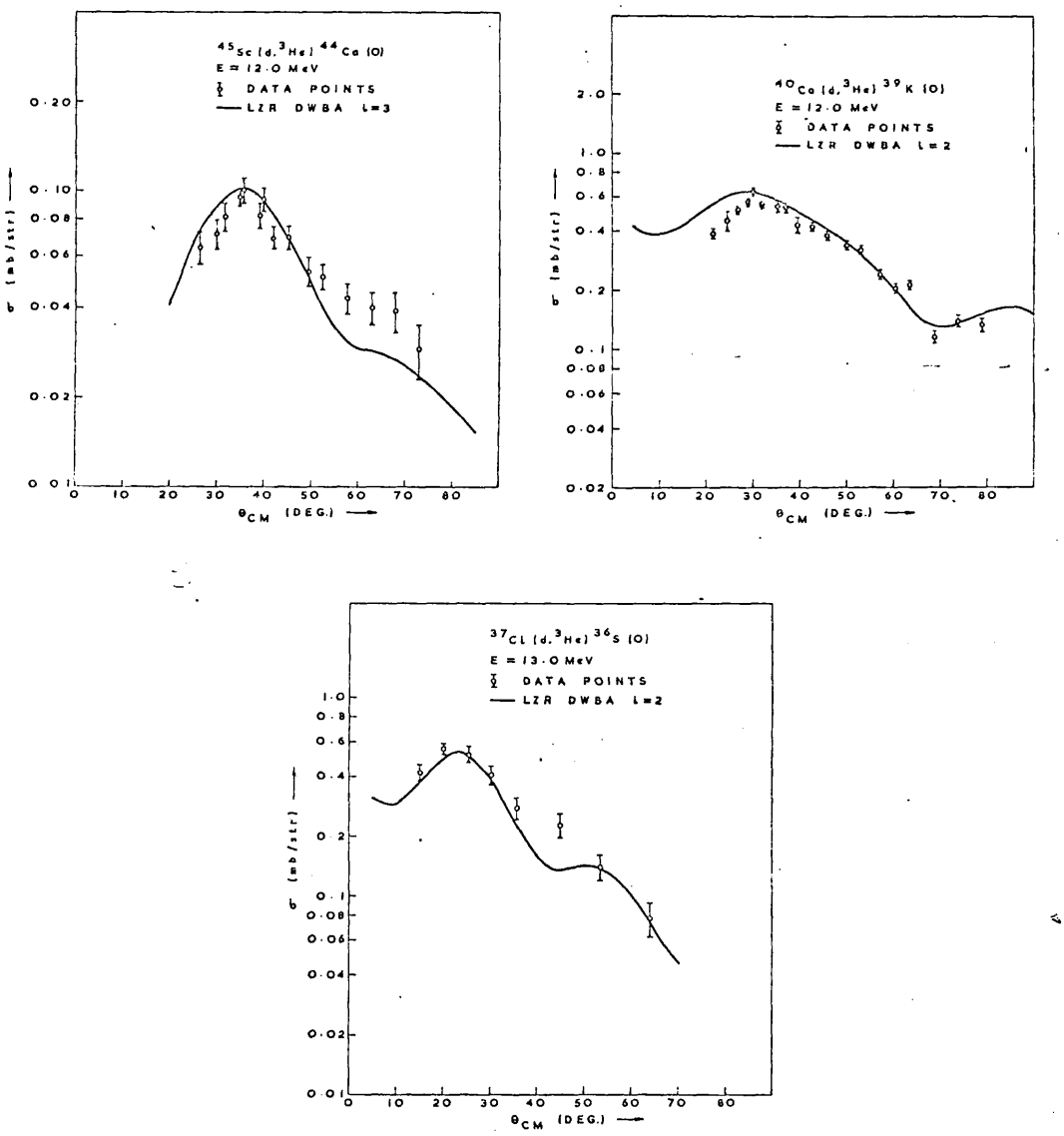

Fig: 6.1.1 (d, ^{3}He) angular distributions with LZR DWBA fit.

6.1.4 DWBA analysis

Local zero-range DWBA calculations were done for the transitions studied. The parameters used in the calculations are shown in the table 6.1.3. For the bound state form factor the separation energy prescription was used throughout. The parameters for the $^{35}Cl(d,^{3}He)^{34}S(0)$ are not shown in the table as they are included in section 6.2.

Table 6.1.3

Parameters used in the DWBA Calculations

CHANNEL		U	R_u	A_u	W	R_w	A_w	R_c
(^{45}Sc+d)	a)	120.69	1.0	0.77	27.28 D	1.138	0.648	1.3
(^{44}Ca+^{3}He)	b)	167.9	1.07	0.775	16.79 S	1.611	0.60	1.3
(^{40}Ca+d)	c)	90.89	1.168	0.817	18.22 D	1.540	0.43	1.3
(^{39}K+^{3}He)	d)	181.0	1.07	0.854	16.12 S	1.81	0.592	1.3
(^{37}Cl+d)	e)	113.34	1.02	0.84	15.93 D	1.44	0.578	1.3
(^{36}S+^{3}He)	f)	173.0	1.25	0.63	17.06 S	1.58	0.78	1.3
Bound States	g)							
^{44}Ca+p		67.09	1.2	0.65	-	-	-	1.3
^{39}K+p		53.59	1.2	0.65	-	-	-	1.3
^{36}S+p		54.20	1.2	0.65	-	-	-	1.3

a) This work (^{45}Sc+d) parameters at 12.0 MeV (c.f. table 5.5.2)
b) [Do67](^{46}Ti+^{3}He) parameters at 12.0 MeV.
c) This work (^{40}Ca+d) parameters at 12.0 MeV (c.f. table 5.5.2)
d) [Bl65] (^{39}K+^{3}He) parameters at 9.0 MeV
e) This work (^{37}Cl+d) parameters at 13.0 MeV (c.f. table 5.5.2)
f) [Ga62] (^{32}S+^{3}He) parameters at 15.0 MeV
g) Bound state potential depths have been adjusted to satisfy binding energy condition.

The table 6.1.4 shows the results from the calculations. The values $\frac{2}{3}$ NC^2S have been extracted by matching the first maximum to the DWBA.

Table 6.1.4

Reaction	$\frac{2}{3}$ NC^2S a)	C^2S b)	N
$^{45}Sc(d,^3He)^{44}Ca(0)$	0.73	0.45 c)	2.43
$^{40}Ca(d,^3He)^{39}K(0)$	8.7	4.0 d)	3.26
$^{37}Cl(d,^3He)^{36}S(0)$	2.9	1.13 e)	3.86
$^{35}Cl(d,^3He)^{34}S(0)$	2.17	0.73 e)	4.76

a) This work

b) The values in this column have been derived by making the sum of the experimental spectroscopic factors

$$\Sigma\, C^2S = \text{Shell model value}$$

c) [Ma69]

d) simple shell model value

e) [Pu69]

6.1.5 Sensitivity test on the DWBA calculations to Optical Parameters

The sensitivity of the DWBA calculations to optical parameters has been tested for the transitions to ^{44}Ca and ^{39}K ground state using a different set of potentials than shown in the table 6.1.3. Sensitivity checks for transitions to ^{36}S and ^{34}S were not done due to nonavailability of suitable parameters in the deuteron channels. The table 6.1.5 summarises the results of the calculations. The potential sets 'A' in the table 6.1.5 refer to the same potential as listed in the table 6.1.3. In the potential set 'B' deuteron parameters have been replaced by the values shown in the table 6.1.6.

Table 6.1.5

Results of sensitivity tests on DWBA calculations.

Transitions	Parameter set	$\frac{2}{3} NC^2S$	N
$^{45}Sc(d,^3He))^{44}Ca(0)$	A	0.73	2.43
	B	1.0	3.33
$^{40}Ca(d,^3He)^{39}K(0)$	A	8.7	3.26
	B	7.5	2.50

Table 6.1.6

Deuteron Channel Parameters used in Set B.

Channel		U	R_u	A_u	W	R_w	A_w	R_c
(^{45}Sc + d)	a)	113.7	1.0	0.785	12.96 D	1.418	0.648	1.3
(^{40}Ca+ d)	b)	93.5	1.168	0.791	21.55 D	1.477	0.428	1.3

a) [Ha68] (^{45}Sc + d) parameters at 7.5 MeV.

b) [Pe63] (^{40}Ca+ d) parameters at 12.0 MeV.

6.1.6 Discussions and conclusion

It can be seen from the table 6.1.4 that values of the normalization obtained are fairly close except in the case of ^{45}Sc(d,^{3}He)^{44}Ca. It has already been pointed out that there was contaminants problem with the ^{45}Sc target which might have lead to smaller cross-section. This problem may have affected the optical parameters as well for ^{45}Sc(d,d)^{45}Sc which in turn may have lead to even smaller value of 'N' as it can be seen from the sensitivity test on optical parameters (i.e. table 6.1.5) that use of (^{45}Sc + d) parameters by Hansen [Ha68] leads to 35% increase in the value of 'N' which brings the value in line with the other values. The average value of 3.8 ± 0.6 for the remaining three transitions is in agreement with the

value of 3.7 ± 0.6 from another detailed study by Armstrong et al [Ar66] on 28 neutron targets. From these results it seems very likely that the value of 'N' lies in between the theoretical values of 3.45 by Thompson [Th70] and 4.42 by Bassel [Ba66]. However it can be seen from the sensitivity test on the $^{40}Ca(d,^{3}He)^{39}K(0)$ case (i.e. table 6.1.5) that the difference noted from either theoretical value could arise from the ambiguities in the optical parameters.

6.2 The $^{35}Cl(d,^{3}He)^{34}S$ reaction

6.2.1 Introduction

The region of nuclei in the upper half of s-d shell ($2s-1d_{\frac{3}{2}}$) has come under considerable attention both experimentally and theoretically recently. The reason is that this region of nuclei provides a good testing ground for shell model calculations [Go68]. Shell model calculations in this region have been reported [Gl64,St67] which reproduces observed spectra reasonably well. However, this agreement is only meaningful if the theoretical wave functions of the various levels are equivalently good approximations. It has already been pointed out (c.f. chapter I and II) that the spectroscopic factors for single nucleon transfer are directly related to the wave function of the nuclear states, hence a comparison between the theoretical and experimental spectroscopic factor provides a criterion for the goodness or otherwise of the wave functions of the nuclear states concerned.

It was reported by Taras [Ta66] that low lying states of ^{35}Cl could be explained as rotational excitations built on the ground state which was assumed to correspond to Nilsson orbit no-8 with $\eta = -2.0$.

This value of η is consistent with ground state electric quadrupole moment. Hence comparison of the spectroscopic factors to the rotational model values are also made.

Two studies on this reaction have been reported recently at 34.5 MeV [Wi68] and at 23.35 MeV[Pu69]. One other study for the ground state transition only was reported by Cujec [Cu62].

6.2.2. Data

The reaction $^{35}Cl(d,^{3}He)^{34}S$ has been studied at an incident energy of 13.0 MeV. Transitions to the ground (0^+), 2.13 MeV(2^+) and 3.13 MeV(2^+) states have been observed. The experimental procedure adopted has already been described in sections 4.3 and 4.4. Both the counter telescope and the spectrograph system were used in a complementary manner.

Initially, experiments were conducted with the counter telescope system using a natural NaCl target. The first excited state of ^{34}S and the ground state of ^{36}S could not be resolved and the data could not be normalised because it was not possible to resolve the contaminant groups in the elastic scattering at 4.0 MeV. Later experiments to find the absolute normalization and the angular distribution to the first excited state (2.13 MeV(2^+)) were conducted with the spectrograph system using separated $Ag^{35}Cl$ target, the composition of which is shown in the table 4.2.1. The absolute normalization was evaluated by comparison with the elastic scattering cross-sections at 4.0 MeV, as pointed out in section 4.7. An approximate estimate of the error in the absolute normalization is ~ 10%. Figures 6.2.1 (a,b,c) shows the angular distributions along with local zero-range (LZR) DWBA curves.

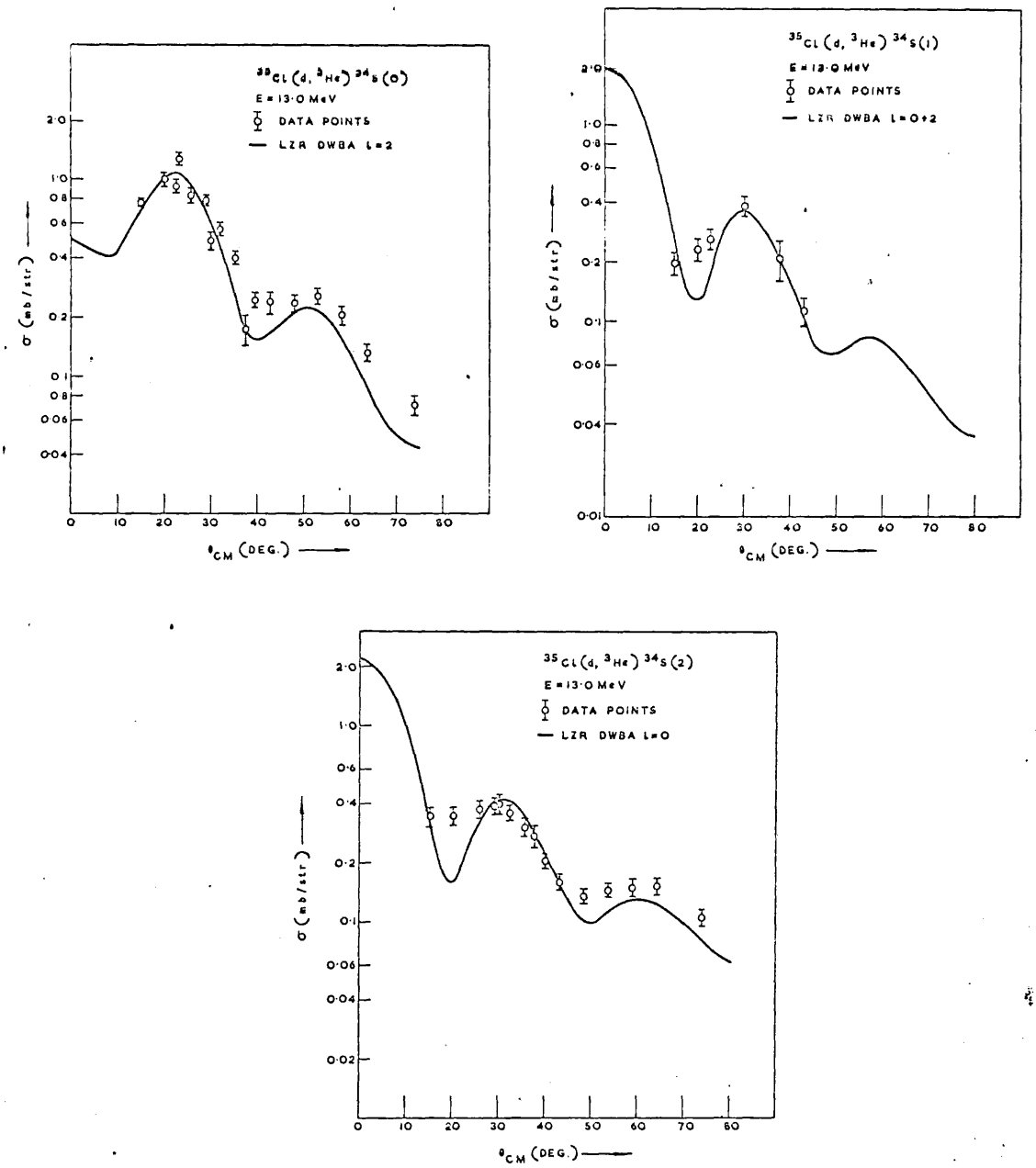

Fig: 6.2.1 (d, ^{3}He) angular distributions with LZR DWBA fit.

6.2.3. DWBA analysis

Local zero-range DWBA calculations were done for the observed transitions. Bound state form factors were assumed to be $1d_{3/2}$ for the ℓ=2 transitions, for the ℓ=0 transitions $2S_{1/2}$ form factors were assumed. The table 6.2.1 shows the parameters used in the DWBA calculations.

Table 6.2.1

Parameters used in the DWBA calculations.

Channel	U MeV	R_u fm	A_u fm	W MeV	R_w fm	A_w fm	R_c fm
^{35}Cl + d a)	108.66	1.02	0.784	12.55 D	1.36	0.772	1.3
^{34}Cl + ^{3}He b)	173.0	1.25	0.63	17.06 S	1.58	0.78	1.3
^{34}S + p c)							
Ex=0.0 MeV							
$1d_{3/2}$	52.75	1.2	0.65	-	-	-	1.3
Ex=2.13 MeV							
$1d_{3/2}$	55.98	1.2	0.65	-	-	-	1.3
$2S_{1/2}$	58.24	1.2	0.65	-	-	-	1.3
Ex=3.13 MeV							
$1d_{3/2}$	57.72	1.2	0.65	-	-	-	1.3
$2S_{1/2}$	60.09	1.2	0.65	-	-	-	1.3

a) This work (^{35}Cl + d) parameters at 13.0 MeV(c.f. table 5.5.2).

b) [Zr68] (^{32}S + ^{3}He) parameters at 15.0 MeV.

c) Potential depths were adjusted to satisfy binding energy condition.

For the ground state transition the experimental angular distribution agrees well with the DWBA calculation. The angular distribution for the first excited state is available over a small region only. For the second state only an ℓ=0 distribution is plotted as the contribution from the ℓ=2 distribution is very small. The deep minima at 20^{0} shown by the DWBA is not seen in the experiment.

The table 6.2.2 shows the spectroscopic factors obtained along with all the other theoretical and experimental values available in the literature. The normalization factor of 4.42 by Bassel (Ba66) was used to extract the spectroscopic factors. For the ground state transitions a spectroscopic factor was obtained by matching the first maxima with the DWBA calculations. The ℓ=0 and ℓ = 2 decomposition for the transition for the transition to 2.13 and 3.31 MeV states were done using a least square fitting computer programme. Statistical errors less than 10% are not shown in the table. The decomposition into ℓ = 0 and ℓ = 2 distributions provides best values and hence no errors are shown on them.

6.2.4 Discussions.

A comparison of the spectroscopic factors in the table 6.2.2 shows that the values of the spectroscopic factors obtained in this work, is in fair agreement with the values at 23.35 MeV [Pu69] and 34.5 MeV [Wi68]. For the ℓ=0 transition at 34.5 MeV the spectroscopic factor for the first excited state is in excellent agreement with this work but the ℓ=0 transition for the second excited state is about 30% lower. The values for the ℓ=2 transitions are consistently higher in 23.35 MeV work than either this or 34.50 MeV work but the ℓ=0 transitions are in

Table 6.2.2

Spectroscopic factors for $^{35}Cl(d,^{3}He)^{34}S$ transitions.

Group	Level MeV	j^{π},T	B.E. of separated particle	E=13.0 MeV[a] C^2S $\ell=0$ $(s_{1/2})$	E=13.0 MeV[a] C^2S $\ell=2$ $(d_{3/2})$	E=150 MeV[b] C^2S $\ell=2$	E=23.35 MeV[c] C^2S $\ell=0$	E=23.35 MeV[c] C^2S $\ell=2$	E=34.5 MeV[d] C^2S $\ell=0$	E=34.5 MeV[d] C^2S $\ell=2$	Shell Model[e] $\ell=0$	Shell Model[e] $\ell=2$	Shell Model[f] $\ell=0$	Shell Model[f] $\ell=2$	Rot. Model[g] Pick up orbit	Rot. Model[g] C^2S $\ell=0$	Rot. Model[g] C^2S $\ell=2$
1	0.0	$0^+,1$	-6.366	-	.735	1.26	-	1.0	-	0.86	-	.73	-	.71	8 $k_f=0$	-	0.32
2	2.13	$2^+,1$	-8.496	.24	.126	-	0.25	0.37	.26	<.21	0.39	.14	.061	.11	8 $k_f=0$	-	0.34
3	3.31	$2^+,1$	-9.666	1.002	.012	-	0.98	-	.70	<.07	0.69	.004	0.81	.07	9 $k_f=2$	0.35	-

a) This work

b) [Cu62]

c) [Pu69]

d) [Wi68]

e) [Wi68] (Set A)

f) [Wi68] (Set B)

g) Calculated using eq. 2.7.10

excellent agreement with this work. The divergence may be partially due to the ambiguity in decomposition into $\ell = 0$ and $\ell = 2$ distributions and partially due to ambiguity in the absolute normalization arising from optical parameter ambiguities. The disagreement of the ground state spectroscopic factor by Cujec [Cu62] is due to the use of different normalization for the DWBA calculations than the other works.

The spectroscopic factors obtained in this work are in good agreement with the shell model calculations 'set A' (table 6.2.2) for the ground and the first excited state but this calculation predicts a 30% lower value for the second excited state. The calculations in 'set B' (table 6.2.2) improves the agreement with the second excited state but at the cost of divergence from the first excited state. The experimental spectroscopic factors disagrees very strongly with the rotational model values. Such a strong disagreement even for the ground state transition points against a rotational description for the ground state of ^{35}Cl (c.f. section 2.7)

6.2.5 Conclusion

The $^{35}Cl(d,^{3}He)^{34}S$ reaction studied at an incident energy of 13.0 MeV. The transitions to the ground state and the first two excited states have been observed and the spectroscopic factors for the transitions have been extracted using DWBA. The spectroscopic factors show fair agreement with the previous work and the shell model calculations. The spectroscopic factors differ very strongly from the rotational model values.

6.3 The $^{27}Al(d,^{3}He)^{26}Mg$ reaction

6.3.1 Introduction

A great deal of experimental work has been performed to investigate various features of ^{26}Mg. The interest is due to the fact that it lies in the transition region from prolate to oblate deformation [Go60] and from strong to weak coupling [Cr65].

The $^{27}Al(d,^{3}He)^{26}Mg$ reaction has been studied previously at 82 MeV [Wa69], 34 MeV [Wi68], 15 MeV [Cu62] and 12.8 MeV [Pe63]. The spectroscopic factors exhibit marked energy dependence. They essentially fall into two groups. The studies at 82 MeV and 34 MeV are quite consistent with each other and the shell model description of the low lying states seem reasonable. On the other hand low energy measurements at 15 MeV and 12.8 MeV are in better agreement with the rotational-vibrational model. The $^{27}Al(n,d)^{26}Mg$ reaction at 14.0 MeV [Gl61] also leads to the same conclusion. However, these lower energy studies were conducted employing difficult techniques. The spectroscopic factors for 12.8 MeV and the (n,d) experiments were extracted using DWBA.

The purpose of the present study is to investigate this energy dependence of spectroscopic factors and hence also to understand the configurations of the low lying states.

6.3.2 Data

The reaction $^{27}Al(d,^{3}He)^{26}Mg$ was studied at an incident energy of 13.0 MeV. Transitions to the ground and the first two excited states were observed. The angular distributions of the ^{3}He particles

were measured using the counter telescope system and checked at some angles using the spectrograph system. In the figure 3.3.8 a spectrum obtained with the counter telescope system for $^{27}Al(d,^{3}He)^{26}$ has already been shown.

Absolute cross-sections were found by comparison with scattering cross-section at 4.0 MeV and assuming the cross-section to be reasonable optical potential as explained in section 4.7. For an element as light as ^{27}Al, nuclear contributions to the elastic scattering even at 4.0 MeV are quite substantial and are the main cause of uncertainty in the absolute normalization. An error of 10 to 15% in the absolute cross-sections is considered to be a conservative estimate. Figures 6.3.1 (a,b,c) show the angular distribution along with LZR (local zero range) DWBA curves. The errors shown in the figures are purely statistical in nature. The transition to the 2.94 MeV level shows poor agreement with the DWBA calculation.

6.3.3 DWBA Analysis

The first set of DWBA calculations were done using the separation energy procedure for bound state form factors i.e., with bound state energies equal to actual separation energies. Local zero-range approximation was used in the calculations. The table 6.3.1 summarises the optical potential as well as the bound state parameters used in the calculations.

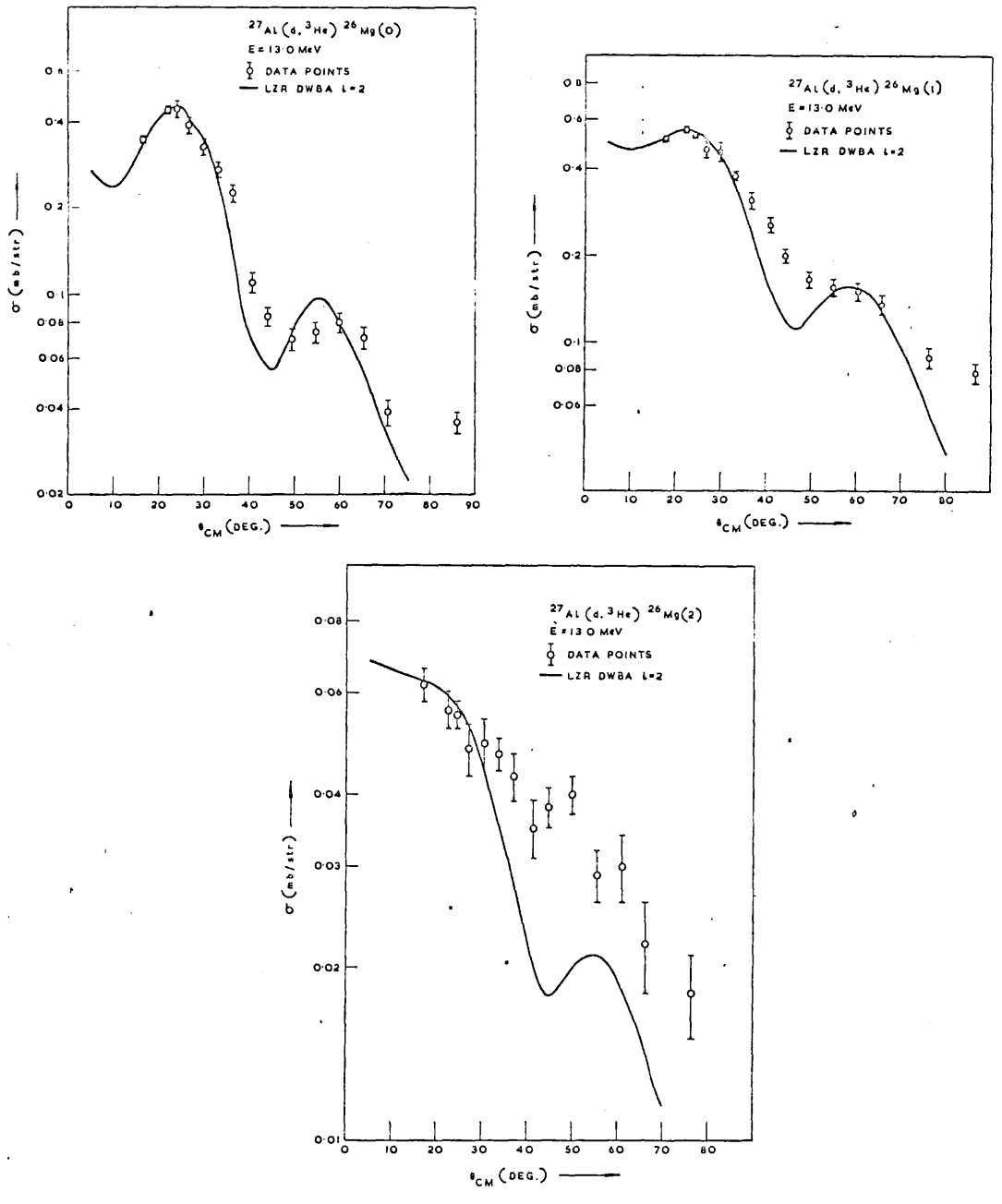

Fig: 6.3.1 (d, ^{3}He) angular distributions with LZR DWBA fit.

Table 6.3.1

Parameters used in the DWBA calculations

Channel		U MeV	R_u fm	A_u fm	W MeV	R_w fm	a_w fm	R_c
^{27}Al+d	a)	108.8	1.0	0.88	25.37 D	1.507	0.527	1.3
^{26}Mg+^{3}He	b)	173.0	1.11	0.74	36.36 S	1.430	0.75	1.3
^{26}Mg+ p	c)							
S.E. Proc								
Ex = 0.0/$d_{5/2}$		61.43	1.2	0.65	–	–	–	1.3
Ex = 1.809/$d_{5/2}$		64.29	1.2	0.65	–	–	–	1.3
$2s_{1/2}$		66.10	1.2	0.65	–	–	–	1.3
Ex = 2.94 $1d_{5/2}$		66.04	1.2	0.65	–	–	–	1.3
$2s_{1/2}$		67.98	1.2	0.65	–	–	–	1.3
E.B.E. Proc.								
Ex = 1.809/$d_{5/2}$		61.43	1.2	0.65	–	–	–	1.3
$2s_{1/2}$		63.01	1.2	0.65	–	–	–	1.3
Ex = 2.94/$d_{5/2}$		64.06	1.2	0.65	–	–	–	1.3
$2s_{1/2}$		65.85	1.2	0.65	–	–	–	1.3

a) This work (^{27}Al+d) parameters c.f. table 5.5.2

b) [Zr68] (^{26}Mg+^{3}He) parameters at 15.0 MeV.

c) Bound state potentials were obtained by varying the depth of the well to suit the binding energy condition.

Table 6.3.2 shows the spectroscopic factors using the normalization factor by Bassel [Ba66] of 4.42. For the two excited states the angular momentum transfer of ℓ=0 is allowed in addition to ℓ=2, so it is imperative that one should try to fit the angular distributions for these states with weighted combination of ℓ=0 and ℓ=2 DWBA distributions. This was attempted and spectroscopic factors have been calculated assuming both pure ℓ=2 distribution and ℓ=0+2 composite distribution. The spectroscopic factors in the former case were extracted by matching DWBA cross-section to the first observed peak for the ground and the first excited states and for the 2.94 MeV state by matching to 15^{o} data. For decomposition of the angular distributions into ℓ=0 and ℓ=2 components procedure described in section 4.8 was adopted. The spectroscopic factors extracted were not very reliable because data were not available for angles near zero degrees where ℓ=0 distributions have very large values. This was more so because the fit to the DWBA calculations was not very good even for pure distributions at angles greater than $\sim 40^{o}$. The DWBA fits to the two excited state angular distributions are shown in the figure 6.3.2 with composite (ℓ=0+2) DWBA fit.

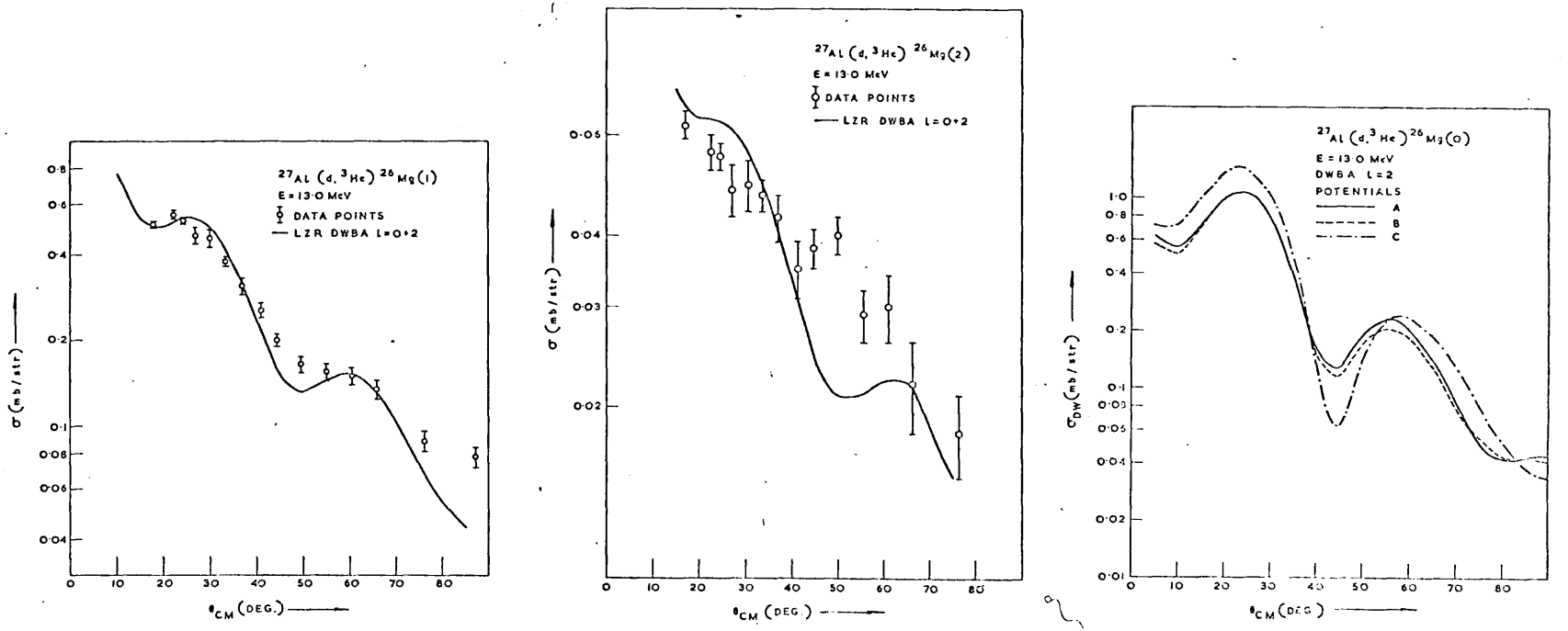

Fig: 6.3.2 (d, ^{3}He) angular distributions with LZR DWBA fit.

Table 6.3.2

Spectroscopic factors from separation energy calculations for ^{26}Mg states.

Level MeV	J^π	B.E. of transfered proton	Allowed ℓ transfer	C^2S a) $\ell = 2$	C^2S $\ell = 0$	b) $\ell = 2$
0.0	0^+	-8.272	2	0.43	-	0.43
1.809	2^+	-10.082	0+2	1.47	0.11	1.32
2.94	2^+	-11.212	0+2	0.38	0.04	0.37

a) Assuming pure $\ell = 2$ transfer

b) From least square fit with $\ell = 0+2$ distribution (variance ~ 10%)

The second set of DWBA calculations were done using the effective binding energy procedure assuming a rotational description for ^{27}Al. The same binding energy of 8.24 MeV was used for the ground state and the first excited state since in the rotational model picture they are members of a K=0 ground state band formed by pickup from Nilsson orbit no.5. For the second excited state pickup has been assumed from Nilsson orbit no.7 which is 1.69 MeV below orbit no.5 for $\eta = 3.0$, a value widely quoted for ^{27}Al. Hence a binding energy of 9.93 MeV was used in the calculation for this level. These binding energies are the same as those used by Cujec [Cu62]. Optical parameters and the normalization used were the same as in the previous calculations. The table 6.3.3 summarises the spectroscopic factors.

The same procedure for decomposition into $\ell = 0$ and $\ell = 2$ distribution was adopted for the two excited states as in the previous case and the same comments apply to the values obtained. As the distributions are very similar to the previous calculations they have not been plotted.

Table 6.3.3

Spectroscopic factors from effective binding energy procedure

^{26}Mg states.

Level MeV	J^π	B.E. of transferred proton	Allowed transfer	C^2S a) $\ell = 2$	C^2S b) $\ell = 0$	C^2S b) $\ell = 2$
0.0	0^+	-8.272	2	0.43	-	0.43
1.809	2^+	-8.272	0+2	0.91	0.09	0.786
2.94	2^+	-9.93	0+2	0.29	0.04	0.255

a) Assuming pure $\ell = 2$ transfer

b) From least square fit with $\ell = 0+2$ distribution (variance ~ 10%).

6.3.4 Sensitivity of spectroscopic factors to optical parameters.

In order to check the sensitivity of dependence of the spectroscopic factors on the optical potential parameters, DWBA calculations were done for the ground state transition using the three sets of parameters shown in the table 6.3.4. The set 'A' is the same as used in the previous calculations (c.f. table 6.3.1) Table 6.3.5 shows the spectroscopic factors for the ground state transition for

Table 6.3.4

Optical parameters used in sensitivity check on DWBA

Set	Channel		U MeV	R_u fm	A_u fm	W MeV	R_w fm	A_w fm	R_c fm
A	$^{27}Al + d$	a)	108.8	1.0	0.88	25.27 D	1.507	0.527	1.3
	$^{26}Mg + ^{3}He$	b)	173.0	1.11	0.74	36.36 S	1.430	0.750	1.3
B	$^{27}Al + d$	c)	103.0	1.0	0.943	29.6 D	1.501	0.527	1.3
	$^{26}Mg + ^{3}He$	b)	173.0	1.11	0.74	36.36 S	1.43	0.75	1.3
C	$^{27}Al + d$	d)	184.0	1.25	0.765	15.5 D	1.275	0.645	1.3
	$^{26}Mg + ^{3}He$	e)	174.15	1.10	0.714	17.96 S	1.631	0.75	1.3

a) This work ($^{27}Al+d$) parameters c.f. table 5.5.2.

b) [Zr68] ($^{26}Mg + ^{3}He$) parameters at 15.0 MeV.

c) [Sa65] ($^{27}Al + d$) parameters at 10.95 MeV.

d) [Co66] ($^{27}Al+d$) parameters at 15.8 MeV.

e) This work ($^{25}Mg + ^{3}He$) parameters at 14.0 MeV (c.f. table 5.5.2).

Table 6.3.5

Sensitivity test on DWBA for ^{26}Mg ground state.

Parameter set	C^2S $\ell=2$
A	0.43
B	0.43
C	0.32

different sets of parameters. Figure 6.3.2 (c) shows the plot for the three distributions.

The potential set 'B' gives remarkably precise agreement with set 'A' where as set 'C' yields value which is about 25% lower. This rather large difference essentially points to the degree of confidence in the absolute values of the spectroscopic factors reported here [Hi67]. However it should also be remembered that set 'C' potential for the deuteron, is at a different energy from this experiment, and the ^{3}He potential is not for the same nucleus. The relative spectroscopic factors are quite stable with the variation of the optical parameters.

6.3.5 Discussions

The table 6.5.6 shows the compilation of all the (d,^{3}He) spectroscopic factors for the states of ^{26}Mg that have been observed in this work and also the (n,d) spectroscopic factors for the first two states.

It can now be clearly seen that the discrepancy between the spectroscopic factors derived from lower and higher energy experiments can be explained due to different bound state wave functions used in DWBA calculations.

The spectroscopic factors (relative) found by using the actual separation energy as the binding energy for calculation of wave function of picked up particle, are in excellent agreement with the results of Wagner [Wa69] and Wildenthal [Wi68] at 82 MeV and 34.4 MeV respectively in which cases a similar procedure for the bound state wave functions was used to extract spectroscopic factors.

Table 6.3.6

Compilation of Spectroscopic Factors for $^{27}Al(d,^{3}He)^{26}Mg$ and $^{27}Al(n,d)^{26}Mg$.

Group	E=13.0 MeV[a]		E=13.0 MeV[b]		E=12.8 MeV[c]	E=15.0 MeV[d]		E=34.4 MeV[e]			E=82.0 MeV[f]		$^{27}Al(n,d)^{26}Mg$[g]	Rot. Model[h]		Shell Model[i]		
	C^2S $\ell=2$	S/Sg	C^2S $\ell=2$	S/Sg	S/Sg	C^2S $\ell=2$	S/Sg	C^2S $\ell=2$	C^2S $\ell=0$	S/Sg $\ell=2$	C^2S $\ell=2$	S/Sg	S/Sg	C^2S $\ell=2$	S/Sg	C^2S $\ell=2$	C^2S $\ell=0$	S/Sg ℓ
0	0.43	1.0	0.43	1.0	1.0	0.46	1.0	.30	-	1.0	0.27	1.0	1.0	0.33	1.0	0.29	-	1.0
1	1.47	3.42	0.91	2.1	1.52	0.86	1.87	1.05	<.01	3.5	0.92	3.4	2.18	0.59	1.78	0.75	.001	2.5
2	0.38	0.88	0.29	0.67	0.32	0.29	0.63	0.23	<.01	0.77	0.19	0.71	-	.36	1.10	0.29	.003	1.0

a) This work S.E. Proc. calculations (c.f. Table 6.3.2)

b) This work E.B.E. Proc. calculations (c.f. Table 6.3.3)

c) [Pe62] (Spectroscopic factors extracted using DWBA).

d) [Cu62]

e) [Wi68]

f) [Wa69]

g) [Gl61]

h) [Pe62]

i) [Wi68]

The absolute values in this work are consistently higher in each case from the values by Wagner and Wildenthal but are within the combined uncertainty of the values here and the values mentioned earlier. It can also be seen that by using bound state wave functions from rotational model considerations similar to those used by Cujec [Cu62], it is possible to get spectroscopic factors (relative) which are in fair agreement with the results of Cujec [Cu62] and Peliagrini [Pe63] and the (n,d) results of Glover [Gl61], considering that in the last two sets the spectroscopic factors were extracted using PWBA and also that difficult experimental technique was used in the work by Peliagrini.

In the following we shall discuss the implications of $(d,{}^3He)$ spectroscopic factors leading to the first three states of ^{26}Mg observed in this work.

Shell Model and the Spectroscopic Factors

In the extreme shell model picture $\ell=2$ pickup can be considered as being due to $(d_{5/2})^{-1}$ to $(d_{5/2})^{-2}$ T = 1 transitions. In such case spectroscopic factors are $C^2S = 0.33, 1.66$ for $J = 0^+, 2^+$ states respectively. These values (relative) are in good agreement with the values of Wagner and Wildenthal and the values obtained in this work from calculations using separation energy procedure, if spectroscopic factors for the first two 2^+ states are summed.

The more refined effective interaction calculations [Wi68] in $d_{5/2}$ and $S_{1/2}$ configurations give results shown in table 6.5.6, which also agree well with the experiments. This calculation predicts very small $\ell=0$ strengths for the transitions. The values of the spectroscopic

factor for $\ell = 0$ transitions obtained in this work (c.f. tables 6.3.2 and 6.3.3) is rather larger. However this is not necessarily a disagreement as it has already been pointed out, the decompositions in to $\ell = 0$ and $\ell = 2$ strengths are not very reliable. This calculation by Wildenthal [Wi68] describes nearly quantitatively the splitting of the 2^+ strength which is essentially due to $(d_{5/2})^{10}\ (2S_{1/2})^2$ configuration. An increase of the mixing of the states should carry part of the $\ell = 2$ strength from the 2nd 2^+ state to the first 2^+ state and at the same time pushing the states further apart and thus improving the agreement with experiment.

Rotational model and spectroscopic factors.

The rotational model with prolate deformation gives a good qualitative description of many of the properties of low lying levels of ^{27}Al [Al60, Ke64], so it is imperative that one should consider pickup from the deformed orbit. The deformation parameter of $\eta = 3.0$ has been widely quoted. Figure 6.3.3 shows schematically the ground state configuration of ^{27}Al in the rotational model. The spectroscopic factors for pickup from the rotational orbit are given by equation 2.7.10. The table 6.5.2 shows the spectroscopic factors for this model for a deformation of $\eta = 3.0$. The results concerning orbit-5 are independent of the deformation parameter.

The ground and the 1.81 MeV States.

There is evidence that the 0^+ ground state and the 2^+ first excited states of ^{26}Mg are members of K=0 rotational band. The enhancement characteristic of E2 within the same rotational band is present

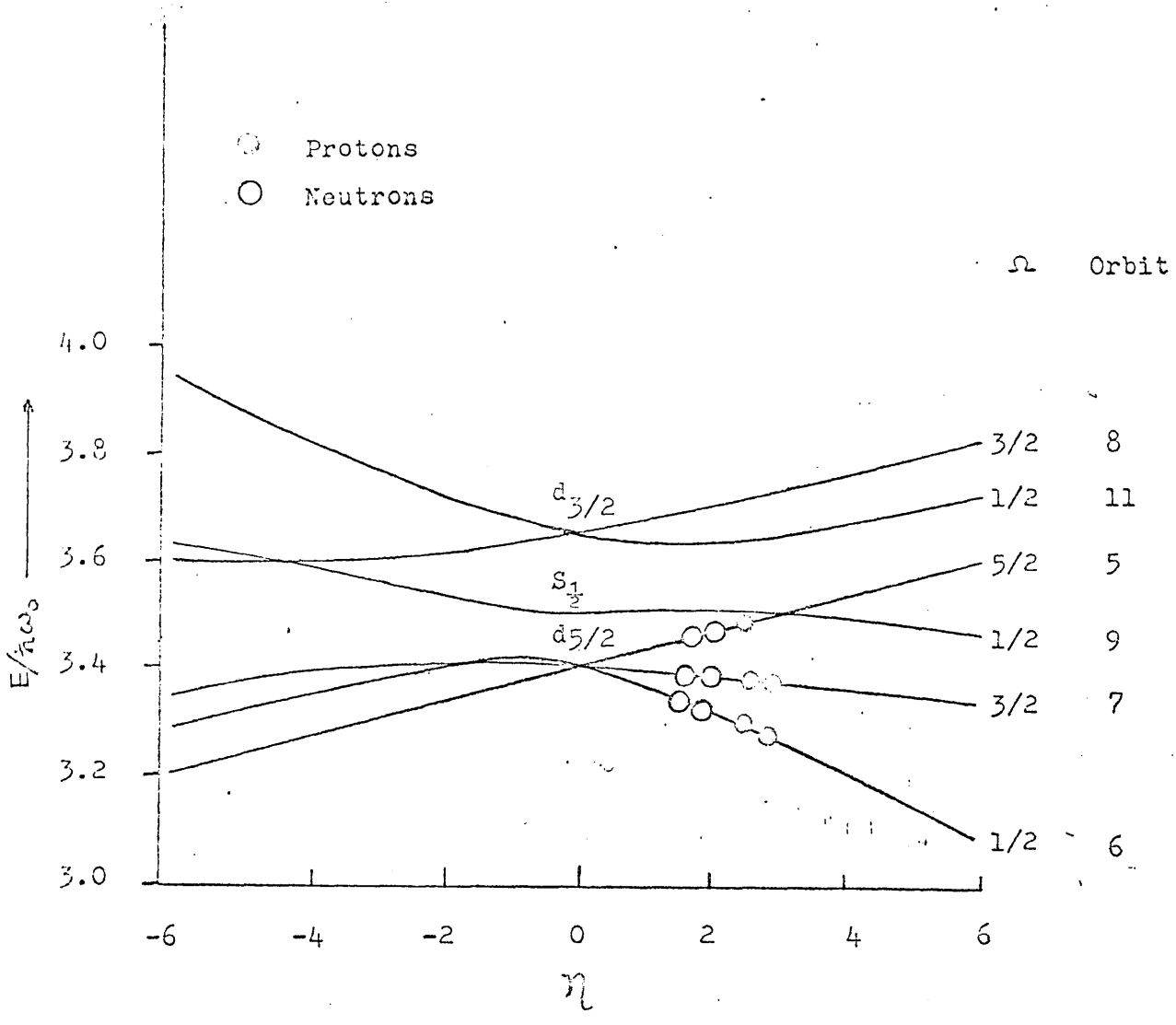

Fig: 6.3.3 Schematic ground state Nilsson configuration for ^{27}Al ($\eta = 3.0$).

The mean life time of the 2^+ state is $(6.0 \pm 1.3) \times 10^{-13}$ sec, which is close to life time of 3×10^{-13} derived from corresponding transition in ^{24}Mg applying energy correction is thirty times faster than the E2 single particle value of 10^{-11} sec [Cu64].

Spectroscopic factors from this work shown in tables 6.3.3 and 6.3.6 are in fair agreement with the rotational model assumption. This calculation assumes complete overlap between the deformed core states of the target and the final nucleus which is not necessarily true. The basis for using EBE procedure has already been pointed out in the section 2.4. The point is that, without solving equation 2.4.6, one can not vouch for the accuracy or otherwise of the wave functions generated in the procedure. So this apparent agreement does not necessarily prove the K=0 band assignment.

On the other hand as pointed out earlier using bound state wave function with binding energy equal to the actual separation energy which has asymptotically the correct shape leads to much too big a value for the ratio of the spectroscopic factors between the two states than expected from the rotational model. Therefore unperturbed K=0 band assignment for these states is in conflict with the $(d, ^3He)$ data.

This is also supported by $^{25}Mg(d,p)^{26}Mg$ transitions [Lu66, Cu64]. The ratio of spectroscopic factors between these two states in (d,p) transition has been found to be 0.24 compared to the value of 0.36 from the rotational model. This 50% difference in relative spectroscopic factors can not be explained away as due to vagaries in DWBA.

2.94 MeV State

The γ-transition probability for this state is consistent with the assumption that this is a member of N_γ=1, K=2 rotation vibrational band [Cu64]. Comparable spectroscopic factors are found in the stripping reaction [Cu64] for this state and the other supposed member of the band 3^+(3.94 MeV) state in agreement with this assumption. However (d, ^{3}He) results at 84 MeV and 34 MeV are not in agreement with this. It has been pointed out by Wagner et al. [Wa69], that this could point to the fact that the intrinsic N_γ = 1 band is not excited at all but only the part of the wave function of the second 2^+ state mixed in from the first is seen. This interpretation would require an increase in 2^+ strength in the first excited state which is already too big from the rotational model description.

3.5.6 Conclusions

The ^{27}Al(d, ^{3}He)^{26}Mg reaction has been studied at an incident energy of 13.0 MeV. Transitions to the first three states in the residual nuclei have been observed and the spectroscopic factors for these states have been extracted.

The energy dependence of the spectroscopic factors for these states from earlier studies has been explained. The spectroscopic factors have been found to be in better agreement with shell model calculations with effective interaction than with rotational model.

6.4 The $^{23}Na(d,^{3}He)^{22}Na$ reaction

6.4.1 Introduction

The static properties of low lying excited states of ^{23}Na are consistent with Nilsson rotational description [Ho67] with a prolate deformation in the region of $\eta = 4.0$.

Tewari and Banarjee [Te66] have done shell mode calculations for the 0^+, 2^+ and 4^+ states in ^{22}Ne. According to their calculations the wave function have quite pure K=0 configurations and the admixture of K=2 band is quite small.

The purpose of this work is to see to what extent these observations are supported by $(d,^{3}He)$ studies. A comparison will also be done with the shell model predictions. A study on this reaction conducted at 34.0 MeV has been reported recently [Wi68].

6.4.2 Data

This study has been conducted at an incident energy of 13.0 MeV. Transitions to the ground state and the 1.274 MeV first excited states have been observed. The experimental procedure was the same as mentioned in section 4.7. Both the counter telescope and the spectrograph system were used in a complementary way as described elsewhere (e.g. section 6.2.2).

Figures 6.4.1 shows the experimental angular distribution along with local zero-range DWBA, which shows strong divergence from the experiments at $\geq 40^{o}$. The same comments as in ^{27}Al case (section 6.3.2) applies for the normalization.

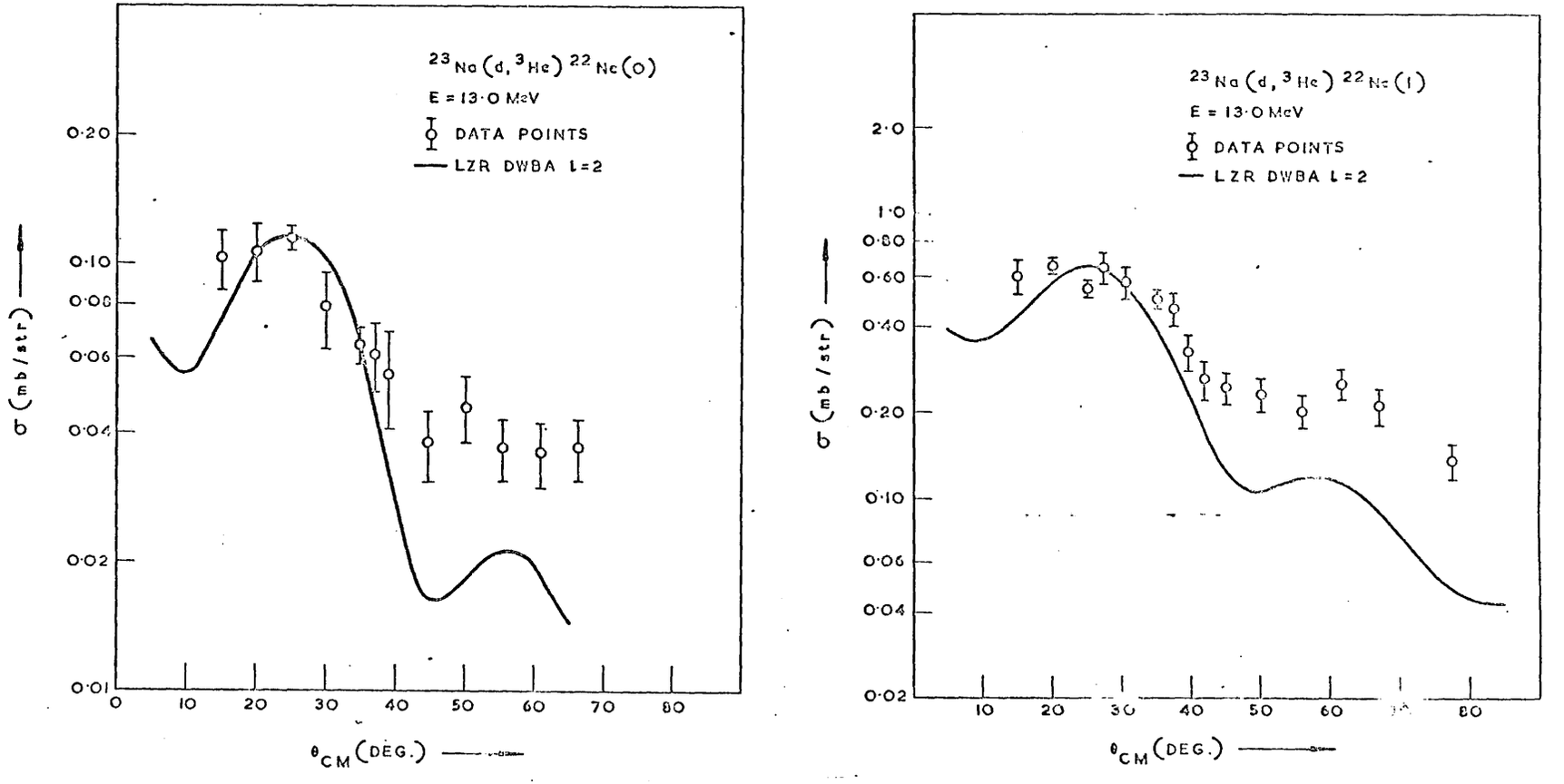

Fig: 6.4.1 (d,^{3}He) angular distributions with LZR DWBA fit.

6.4.3 DWBA calculations

Local zero-range DWBA calculations were done with the parameters shown in the table 6.4.1. The spectroscopic factors were obtained by matching the principal peaks with the DWBA calculations. The spectroscopic factors are shown in the table 6.4.2 along with the values by Wildenthal [Wi69] and the ones calculated from the models. The second value quoted for the 1.274 MeV state has been obtained by using the same separation energy as the ground state.

6.4.4 Discussions

It has already been pointed out that the spectroscopic factors have been obtained by matching the principal peak in the angular distributions with the DWBA calculations, the reason is that the DWBA calculations have been found to be more stable in the region with the changes in the parameters. The absolute spectroscopic factors from this work are consistently higher than the values reported by Wildenthal et al [Wi69] (c.f. table 6.4.2 column a and b) but the divergences are within the combined uncertainty of the two sets.

In the $(1d_{5/2}-2S_{1/2})$ shell model picture, the ground state transition is J forbidden and the transition is due to $1d_{3/2}$ admixture. In the rotational model, the transiton proceeds with small amplitude. The table 6.4.2 (column c) shows the spectroscopic factors from the rotational model with the assumption of pickup from the Nilsson orbit No.7. The ground state configuration of ^{23}Na is shown schematically in the figure 6.4.2.

Table 6.4.1

Parameters used in DWBA Calculations

Channel		W	R_u	A_u	W	R_w	A_w	R_c
$^{23}Na + d$	a)	80.73	1.0	0.92	37.28D	1.39	0.583	1.3
$^{22}Nc + {}^{3}He$	b)	165.19	1.14	0.72	13.19S	1.86	0.72	1.3
$^{22}Nc + p$	c)							
S.E. Proc								
Ex = 0		66.634	1.2	0.65	-	-	-	1.3
Ex = 1.274		68.690	1.2	0.65	-	-	-	1.3
EBE Proc								
Ex = 1.274		66.634	1.2	0.65	-	-	-	1.3

a) This work ($^{23}Na + d$) parameters at 13.0 MeV (c.f. table 5.5.2)

b) [Zr68] ($^{22}Ne + {}^{3}He$) parameters at 15.0 MeV

c) Bound state potentials have been found by varying the depth to satisfy the binding energy conditions.

Table 6.4.2

Spectroscopic Factors for ^{23}Na (d, ^{3}He) ^{22}He transitions

States	Ex	j^{π}	Separation energy of proton	C^2S a) E=13.0 MeV ℓ=2	C^2S b) E=34.0 MeV ℓ=0	ℓ=2	C^2S c)	C^2S d) ℓ=0	ℓ=2
0	0.0	0^+	+8.736	0.137 ±.020	-	0.08	0.014	-	-
1	1.274	2^+	+10.010	1.35	<.02	1.11-1.18	0.64	0.04	1.18
1	1.274	2^+	+ 8.736	0.95	-	-	-	-	-

a) This work

b) [Wi68]

c) Rotational model values. Calculated using equation 2.7.10.

d) Shell model calculations [Wi68].

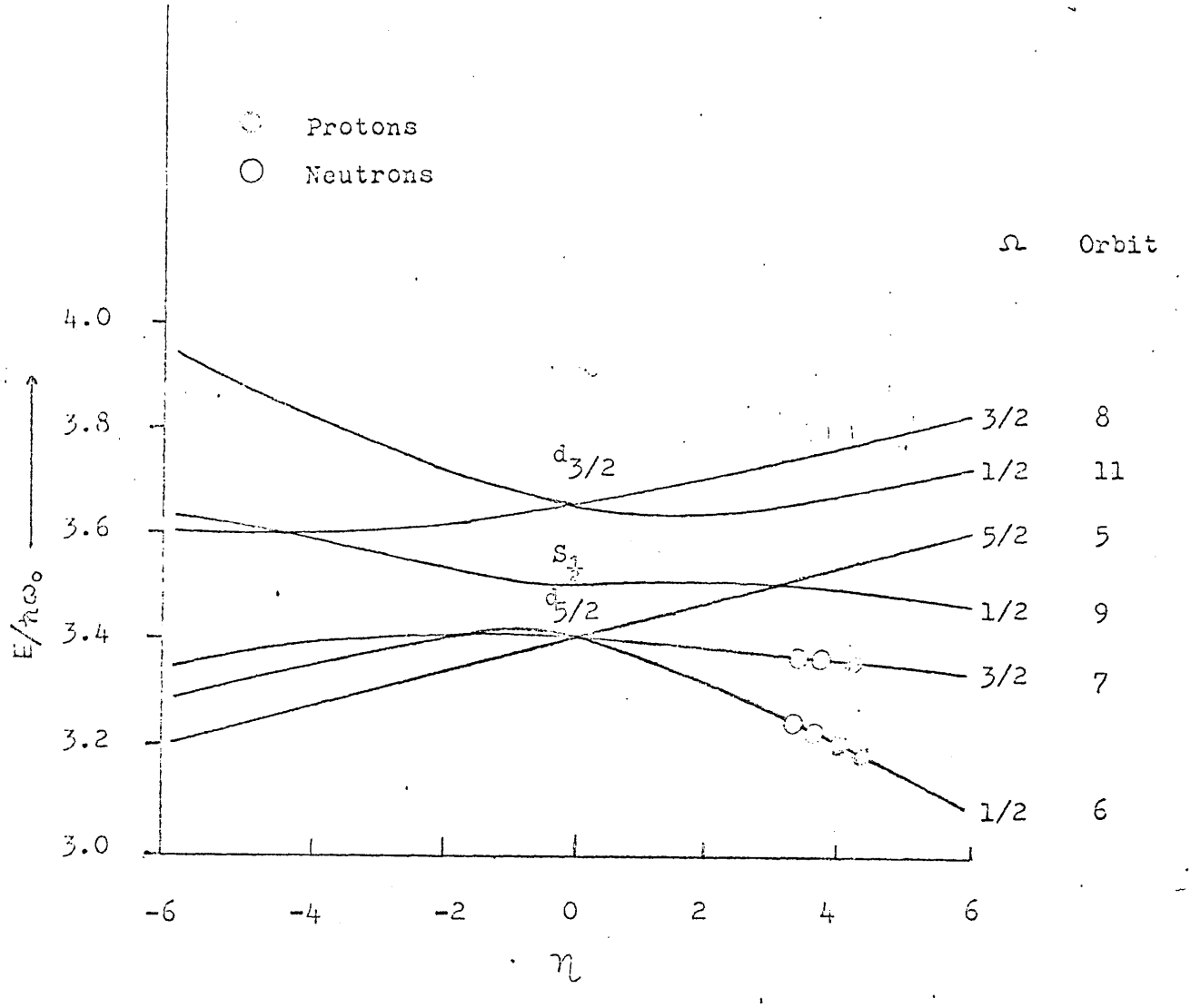

Fig: 6.4.2 Schematic ground state Nilsson configuration for ^{23}Na ($\eta = 4.0$).

The shell model spectroscopic factors quoted in table 6.4.2 (column d) are the same as Wildenthal [Wi68]. The observed spectroscopic factor for the ground state transition though small is large compared to the values predicted from either model. The extent of the $1d_{\frac{3}{2}}$ admixture in the ground state of ^{23}Na (~10%), shows the inadequacy of the truncation of the shell model calculations by including only $1d_{5/2}$-$2S_{\frac{1}{2}}$ configurations.

The comparison of the relative spectroscopic factors would not be meaningful because of this comparatively large value for the ground state transition. The absolute value for the spectroscopic factor for the 1.274 MeV state is in agreement with both the models within the vagaries in DWBA as pointed out earlier (c.f. section 6.3.3). The spectroscopic factor for this state calculated in the effective binding energy procedure assuming the same bound state energy as the ground state is nearer in value to the rotational model value. However, as it has been already pointed out (c.f. section 6.3.5) this could be fortuitous.

6.4.5 Conclusion

The $^{23}Na(d,^{3}He)Ne^{22}$ reaction has been studied at an incident energy of 13.0 MeV. The transitions to the ground state (0^+) and the 1.274 MeV (2^+) states in ^{22}Ne have been observed. The spectroscopic factors have been extracted for these states using LZR DWBA and compared with the rotational and the shell model predictions. The ground state transition has been found to have larger spectroscopic factor than predicted by either model which indicates the degree of $1d_{\frac{3}{2}}$ admixture in the ^{23}Na ground state.

CHAPTER VII

THE (^{3}He,d) AND THE (d,n) REACTION STUDIES

7.1 Introduction

The primary incentive to study the (^{3}He,d) and (d,n) reactions leading to $T_z = 0$ final nuclei in the s-d shell came from work by Siemssen et al. [Si66]. In this work a discrepancy of the spectroscopic factors between T=0 and T=1 states in (^{3}He,d) reaction was found from model considerations. Discrepancies were also reported between (^{3}He,d) and (d,n) reactions for transitions leading to the same T=1 final states in the residual nuclei in this work.

The experiments reported in this chapter were performed to investigate the discrepancy of spectroscopic factors mentioned earlier and also to compare the spectroscopic factors obtained with the various model calculations reported. Each reaction studied is reported under a separate section.

7.2 The ^{29}Si(^{3}He,d)^{30}P Reaction

7.2.1 Introduction

The energy levels of the self conjugate ^{30}P nucleus are well established from the studies of (p,γ) [Va58,Ba62,Mo63,Ha66a,

Ha66b,Ha67], (d,α) [En58] and (^{3}He,p) [Ve69] studies.

Firm spin and parity assignments have been made for the 0.0, 0.67 0.71, 1.45, 1.98, 2.54, 2.96 and 4.18 MeV states only. For the other states there are either several alternative assignments or the assignments are disputed. The spins and parities of the states are considered in detail in section 7.2.4.

A shell model calculation of ^{30}P has been reported by Glaudman et al [Gl64] which explained quite well the energies of the low lying states. A comparison of the spectroscopic factors from this work was done with the spectroscopic factors from the Glaudman calculations to check the correctness or otherwise of the wave function of the calculated states.

Rotational model calculations with residual neutron proton interaction have been reported by Pickard and de Pinho [Pi66] and by Ascuito et al. [As68]. These also show good agreement with the first three levels. However, no spectroscopic factors were reported in these papers.

No experimental spectroscopic factors for this nucleus have so far been reported. Hence this work provides a substantial body of completely new information.

7.2.2 Data

The reaction ^{29}Si(^{3}He,d)^{30}P was studied at an incident energy of 14.0 MeV. Transitions to 19 states up to 4.61 MeV excitation were observed. Angular distributions for the 15 transitions up to 4.23 MeV excitation were determined.

The Harwell multigap spectrograph was used in the experiment. The

properties of the target used has been shown in the table 2.4.1. Although exposures were taken in all the 24 gaps of the spectrograph, only the first nine gaps (i.e. from 5^{o} to 65^{o} (Lab) at an interval of 7.5^{o}) were scanned. The over all resolution was about ~ 30 KeV which was mostly due to target thickness. The ground state Q-value and the excitation energies of the excited states were found to be in agreement with the values by Endt and Van der Leun [En67] to within ± 20 KeV.

The absolute normalization of the data was obtained by comparing the (^{3}He,d) ground state cross-section with the elastic cross-section at 15^{o} at 14.0 MeV using the single gap system (c.f. section 5.5). The absolute values are believed to be correct within ~ 20%. The large uncertainty in the absolute value of the spectroscopic factors is due to the fact that measurement was done at a single point ($\theta_{Lab} = 40^{o}$) where the cross-section varies rather rapidly with the angle. A spectrum of the deuterons at 12.5^{o} (Lab) is shown in figure 7.2.1. The angular distributions along with appropriate DWBA are shown in figures 7.2.2.

7.2.3 DWBA Calculations

The DWBA calculations were done for the observed transitions using the parameters shown in the table 7.2.1. The separation energy prescription was used for all the bound state form factors.

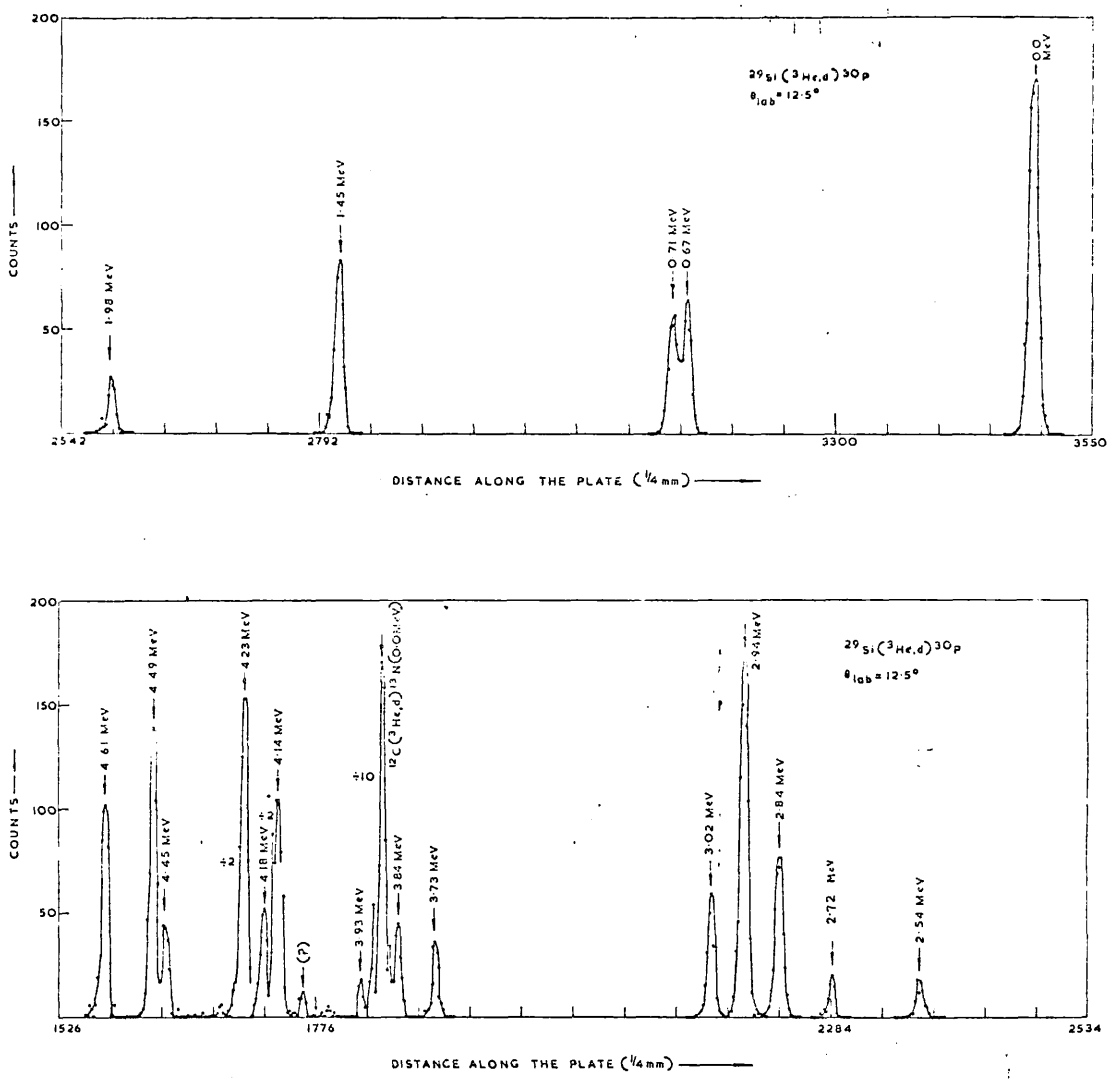

Fig: 7.2.1 Deuteron spectrum from the $^{29}Si(^{3}He,d)^{30}P$ reactions obtained with multigap spectrograph. Energies refer to excitation of the final nucleus.

The figures 7.2.2 show the experimental angular distributions along with appropriate DWBA fits. The states at 0.67 and 2.48 MeV could be fitted well with pure ℓ=0 DWBA. Pure ℓ=2 DWBA fitted fairly well, the states at 1.45, 1.98, 2.54, 2.72, 2.94, 3.84, 4.18 and 4.23 MeV. The state at 3.93 MeV was very weakly excited and was seen only at the first two angles of the multigap exposure. For the remaining states up to 4.23 MeV excitation a combination of ℓ = 0 and ℓ=2 DWBA distributions were required to obtain acceptable fits. The decomposition procedure into ℓ=0 and ℓ=2 components was the same as described in section 4.8. The comments about the uncertainty in the spectroscopic factors are also valid. The table 7.2.2 shows the value of the spectroscopic factors extracted. As the final spin of the some of the states are not known with certainty only $(2J_f+1)C^2S$ values are shown for these states. The value of the normalization constant used for the extraction of the spectroscopic factors was 4.42 [Ba66] .

Table 7.2.1

Parameters used in the DWBA Calculations.

Channel	U MeV	r_u fm	a_u fm	W MeV	r_w fm	a_w fm	R_c fm
$^{30}P + d$ a)	101.7	1.10	0.815	21.22D	1.376	0.556	1.3
$^{29}Si + ^{3}He$ b)	188.99	1.25	0.601	25.27S	1.327	0.813	1.3
$^{30}P + p$ c)	-	1.2	0.65	-	-	-	1.3

a) (^{31}p+d) parameters obtained by fitting data by Denortier et al. [De61] at 11.5 MeV.

b) This work ($^{29}Si + ^{3}He$) parameters at 14.0 MeV (c.f. Table 5.5.2).

c) Potential depth was varied to satisfy the binding energy condition.

Table 7.2.2

Spectroscopic factors from $^{29}Si(^{3}He,d)^{30}$ reaction.

Level MeV	$j^{\pi};T$	L Transfer	$(2J_f+1)C^2S$		C^2S	
			$\ell = 0$	$\ell = 2$	$\ell = 0$	$\ell = 2$
0.0	1^+	0,2	1.65	1.97	0.542	0.65
0.67	$0^+;1$	0	0.62	–	0.62	–
0.71	1^+	0,2	0.327	0.97	0.107	0.324
1.45	2^+	2	–	2.47	–	0.495
1.98	3^+	2	–	0.585	–	0.084
2.54	3^+	2	–	0.332	–	0.048
2.72	$1^+,2^{+*}$	2	–	0.196		
2.84	$0^+,1^{+*}$	0	0.45	–		
2.94	$2^+;1$	2	–	2.07	–	0.415
3.02	1^{+*}	0,2	0.18	0.275	0.06	0.092
3.73	1^{+*}	0,2	0.062	0.18	0.021	0.06
3.84	$1^+,2^{+*}$	2	–	0.353		
3.93	–	–	–	–	–	–
4.14	1^{+*}	0,2	0.193	1.24	0.064	0.41
4.18	$2^+;1$	2	–	0.407	–	0.081
4.23	$1^+,2^{+*}$	2	–	0.25	–	–

* Assignments from this work (c.f. section 7.2.4).

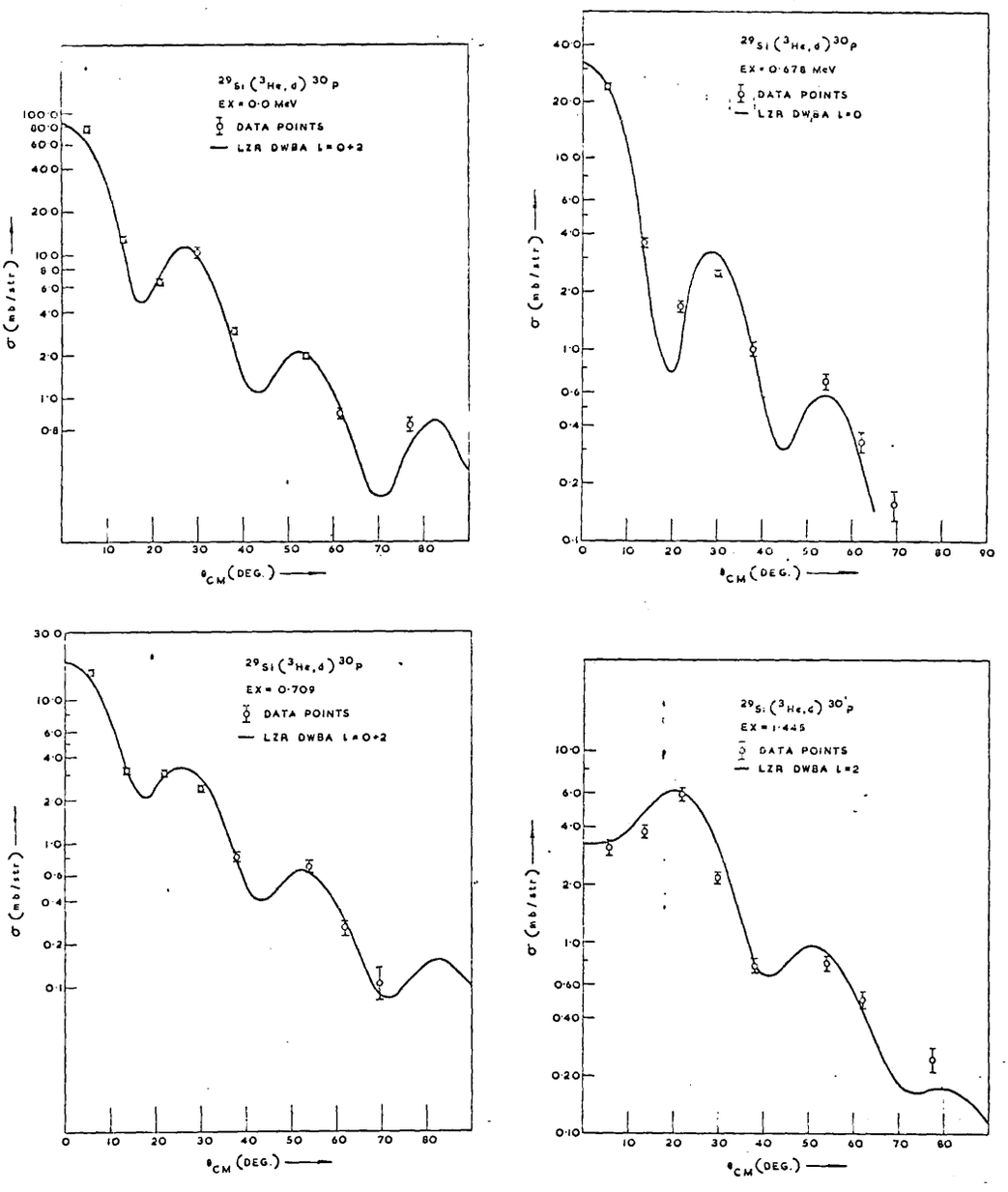

Fig: 7.2.2 (^{3}He,d) angular distribution along with DWBA fits. The quantities 'Ex' also refer to levels in the final nucleus.

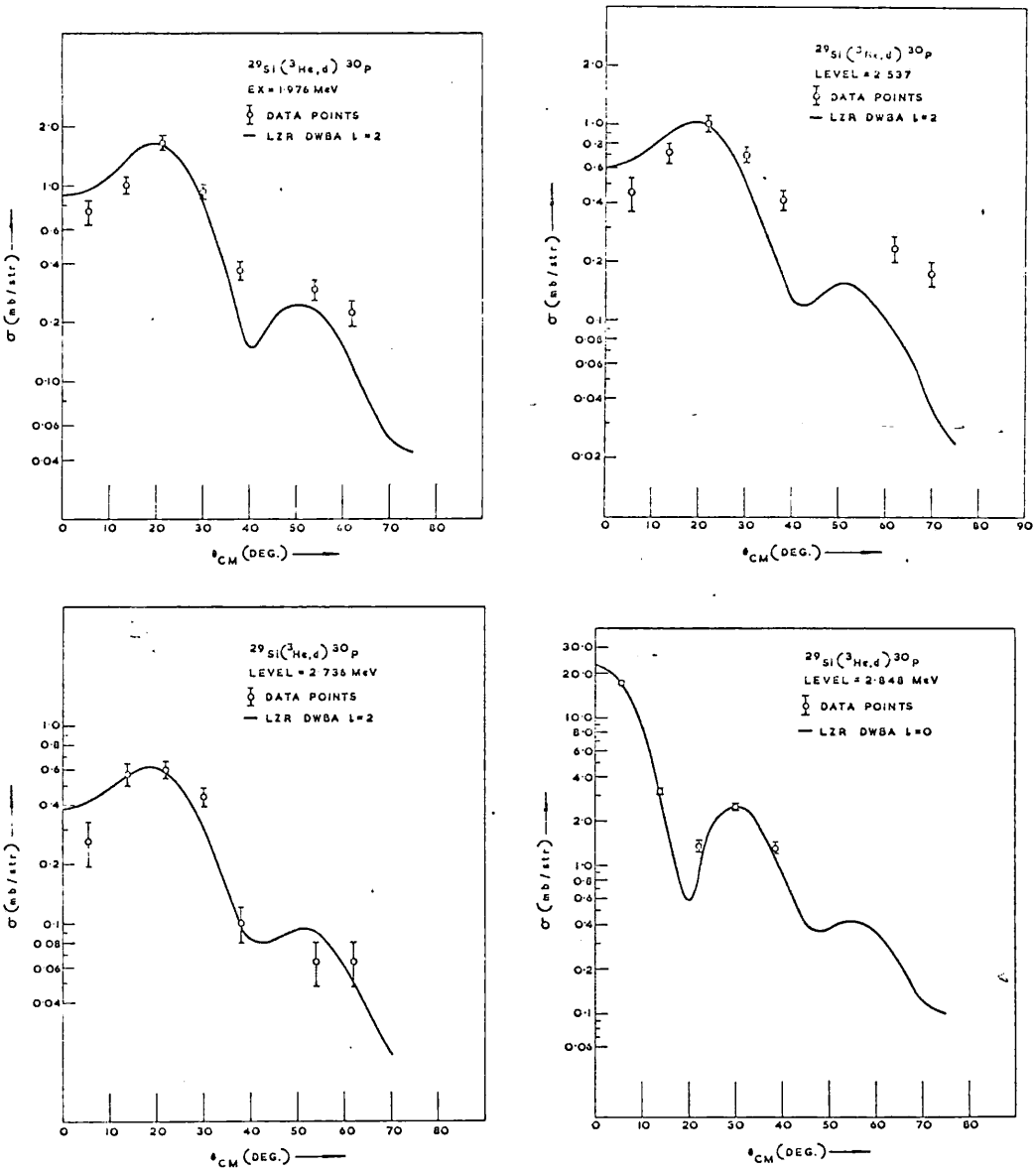

Fig: 7.2.2 continued

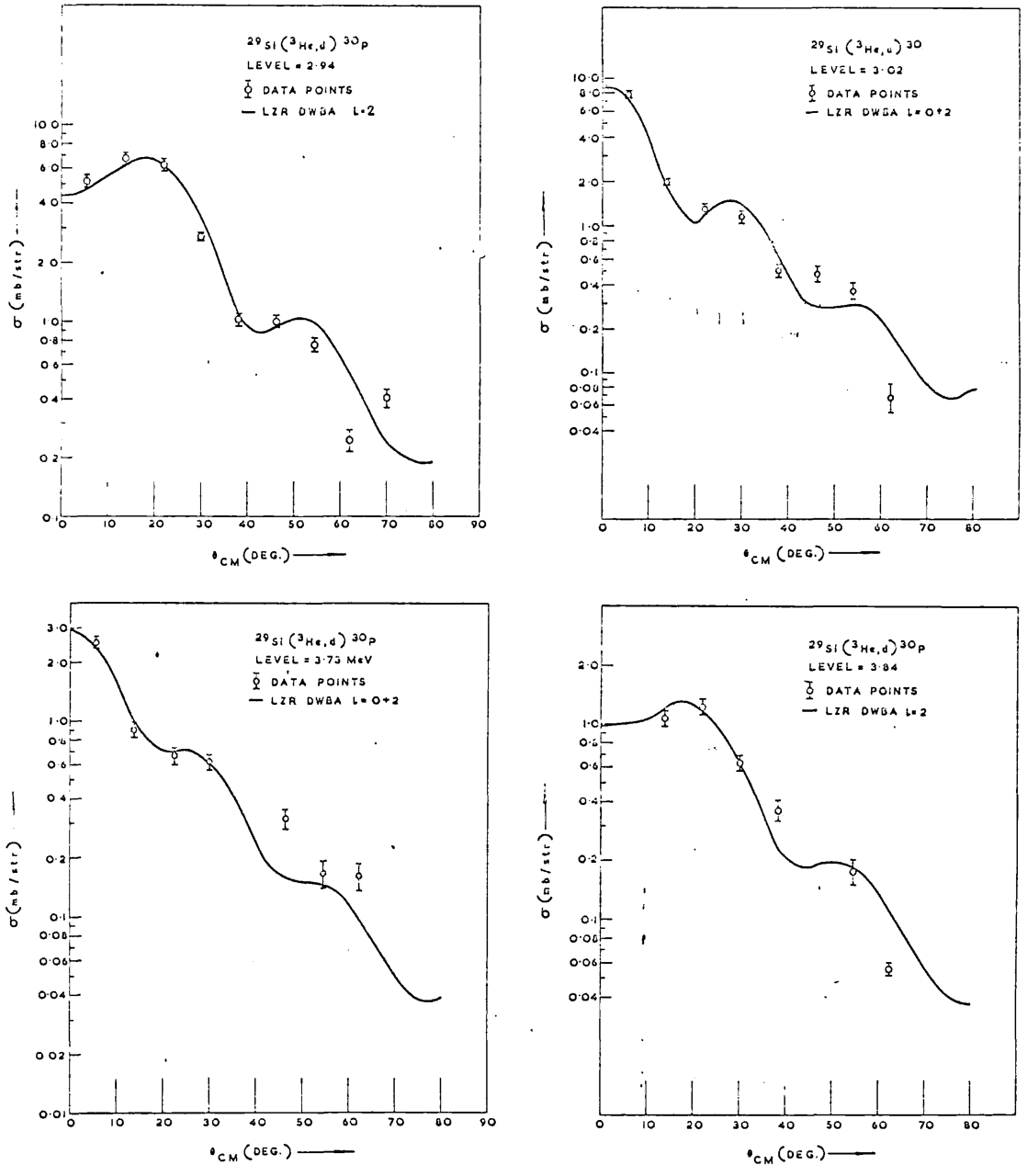

Fig: 7.2.2. continued

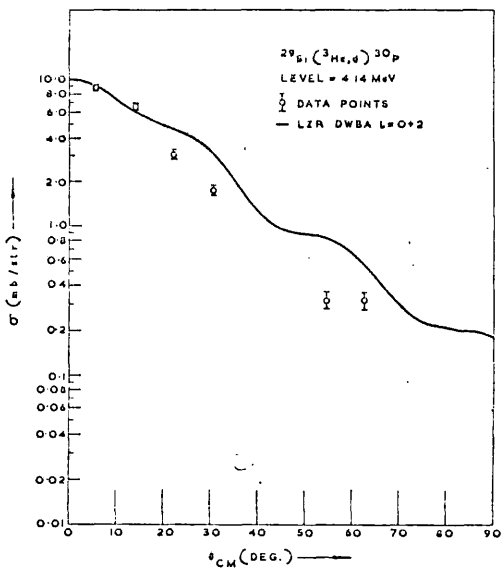

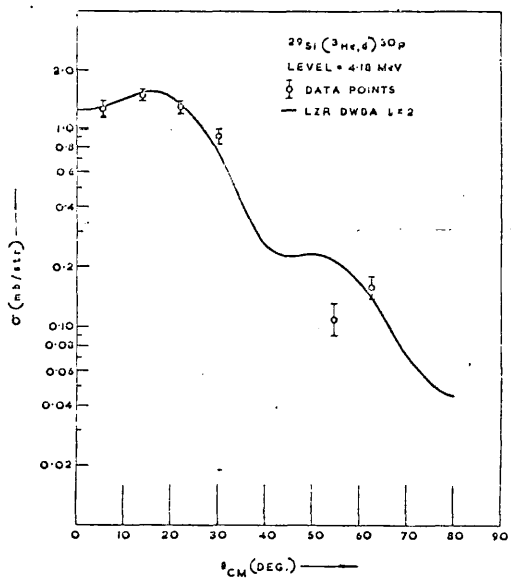

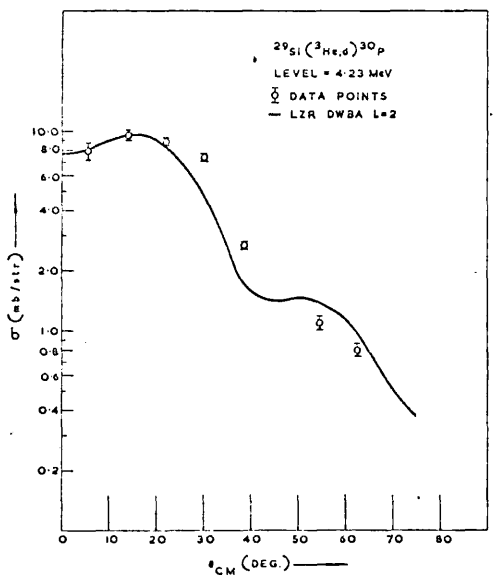

Fig: 7.2.2. continued.

7.2.4 Spin and Parity Assignments

In general definite spin assignments can not be made from the study of single nucleon transfer reactions on odd nuclei. However, in this particular case the initial spin ½ of the ground state of ^{29}Si, limits the number of possibilities of the final state spins to two only and in some cases unique assignments can be made.

The parity is of course $(-1)^{\ell}$ where 'ℓ' is the orbital angular momentum transfer. In the transitions studied, the angular momentum transfer is either 0 or 2 or a combination of the two distributions. For the ℓ=0 transitions the final state spin is limited to 0^+ or 1^+. For the ℓ=2 transitions final state spins of 1^+ or 2^+ are permitted, if a transfer is assumed to be to the empty $1d_{\frac{3}{2}}$ shell. The exceptions are the cases of 1.98 and 2.54 MeV states where firm 3^+ assignments have been made from other measurements. A $d_{5/2}$ transfer corresponding to the holes in the supposedly filled $1d_{5/2}$ shell has to be assumed in these two cases. If a combination of ℓ=0 and ℓ=2 distributions occur the final state spins can only be 1^+. The figure 7.2.3 shows the present and the previous spin assignments for the states in ^{30}P. The 'T' values for the states other than T=0 are only shown in column (b) of the figure. In the column showing the assignments from this work, the cases where alternative spins are permitted from this work but firm assignments have been made from previous studies, have been left out. The values in the brackets are doubtful assignments.

From the above considerations a definite assignment of 1^+ was made to the 3.02, 3.75 and 4.14 MeV states. Alternative assignments of

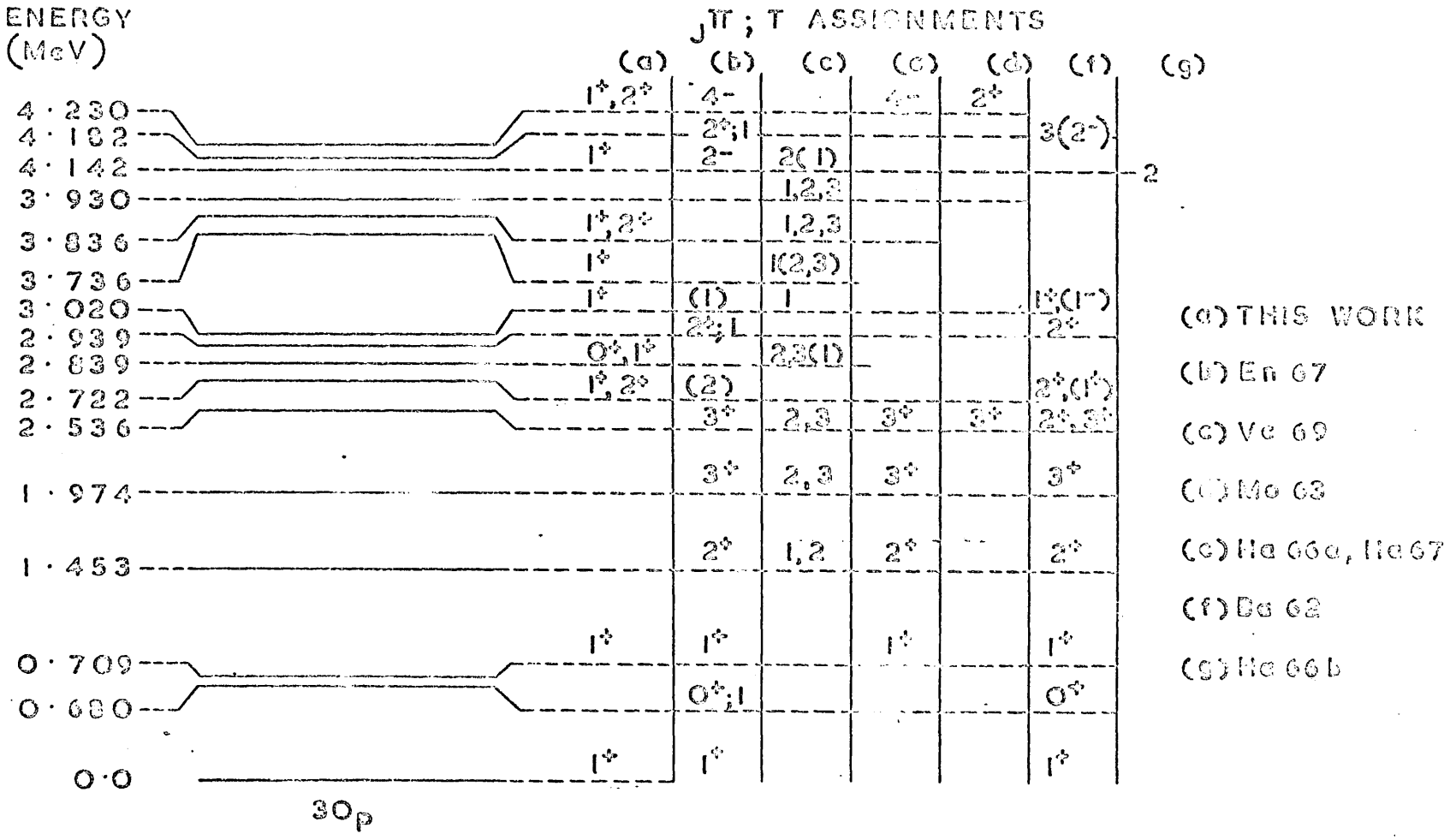

Fig: 7.2.3 Energy levels of ^{30}P.

$(1^+,2^+)$ were made to the states at 2.72, 3.84 and 4.23 MeV. The assignment of 4^- to 4.23 MeV state by Harris and Hyder [Ha66a] is very unlikely to be correct because the fit to ℓ=2 DWBA distribution to this state is as good as to the fit to the 4.18 MeV (2^+, T=1) state. It is also very unlikely that this state is a doublet because states excited in (p,γ) should be seen in (^{3}He,d) as well. Similarly in the absence of any evidence of doublet nature for 3.02 MeV level, the 2^- assignment [En67] for this state is extremely unlikely. The state at 2.84 MeV was assigned alternative spins of $(0^+,1^+)$ due to the presence of only pure ℓ=0 transition.

7.2.5 Discussions

In this section the implications of the experimental results presented in earlier sections are discussed.

Shell Model and the Spectroscopic Factors

The table 7.2.3. shows the comparison of the experimental spectroscopic factors with the values from the shell model calculations by Glaudman [Gl64]. The theoretical values for the 0.68 and 2.94 MeV T=1 states agree very well with the experiments but for the other states this is not so.

Table 7.2.3

Comparison between shell model & experimental spectroscopic factors

Level MeV	Calculated[a] Level MeV	$J^{\pi};T$	C^2S [a] Shell Model $\ell = 0$	$\ell = 2$	C^2S [b] Experimental $\ell = 0$	$\ell = 2$
0.0	0.02	1^+	0.232	0.375	0.542	0.65
0.68	0.67	$0^+;1$	0.726	0	0.62	0
0.71	0.69	1^+	0.768	0.111	0.107	0.324
2.54	2.73	3^+	0	0	–	0.048
2.72[c]	2.91	2^+	0	0.5	–	0.040
2.94	3.0	$2^+;1$	0	0.471	–	0.415
4.18	5.69	$2^+;1$	0	0.029	–	0.081

a) [G164]

b) This work

c) Two spin values 1^+ and 2^+ are possible for this state. By identifying it with the calculated 2.91 MeV level, the spectroscopic factor was extracted assuming 2^+ assignment.

It can be seen by examining the wave functions tabulated by Glaudman et al. [Gl64] for the ^{30}P(J=1, T=0) states shown in the table 7.2.4 that inversion in level order has probably taken place in the calculation between the first (ground state) and the second 1^+ states.

Table 7.2.4

Wave Functions of ^{30}P(J=1, T=0) States.

Calculated Level (MeV)	S2 10	S1d1 1131	d2 10
+ 0.02	+ 23.2	+ 74.9	+ 1.9
+ 0.69	- 76.8	+ 22.2	+ 1.0
+ 4.58	+ 0	- 2.8	+ 97.1

The nomenclature used for the configuration in table 7.1.4 is

$$\begin{matrix} S\ n & d\ m \\ J_1 t_1 & J_2 t_2 \end{matrix} = S^n_{J_1 t_1}\ d^m_{\frac{j_2}{2}\ \frac{t_2}{2}}$$

where underlining indicates half integer. From qualitative reasoning one would expect that the $[^{S2}_{10}]$ component would be the largest for the ground state whereas the calculated + 0.69 MeV state has the larger $[^{S2}_{10}]$ component. If on this logic the spectroscopic factors for the ground and the first excited 1^+ state are interchanged, the agreement between

the experimental and the theoretical spectroscopic factors for the ground state is comparable with the agreement for the T=1 states mentioned earlier. The comparison for the ground state is of course limited to the ℓ=0 component only because of the large uncertainty in the ℓ=2 spectroscopic factors arising out of the decomposition procedure as pointed out earlier. Even with this inversion the experimental spectroscopic factor for the 0.71 MeV state is still smaller than the theory.

The transition to the 2.54 MeV 3^+ state is 'J' forbidden in the $2S_{1/2}$-$1d_{3/2}$ model and only the part of the wave function mixed in from the $1d_{5/2}$ configuration can be seen in this reaction. The fairly large values of the spectroscopic factors to this and the 1.98 MeV state shows the inadequacy of the $2s_{1/2}$-$1d_{3/2}$ model.

The identification of the 2.72 and 4.18 MeV experimental levels with the theoretical 2.91 and 5.69 MeV states respectively, is not consistent with the gross disagreement between the experimental and the calculated spectroscopic factors for these states. From the discussions above it can also be infered that no discrepancy between the experimental values of spectroscopic factors for the T=0 and the T=1 states have been observed from the model values.

Rotational model and the spectroscopic factors.

Brief mention has already been made about the rotational model calculations in the introduction. Baart et al. [Ba62] investigated the applicability of the strong coupling collective model to ^{30}P and

concluded that a description in terms of rotational behaviour is probably inappropriate. Detailed calculation by Picard and DePinho [Pi66] using a rotational Nilsson model with a Soper two body neutron-proton interaction with $\eta = 2.0$ ($\beta \simeq 0.1$) led to a satisfactory prediction of only first two excited states. Another similar calculation by Ascuitto et al. [As68] using for the neutron-proton interaction, a Serber force with a Gaussian radial dependence and $\beta = 0.15$, also led to agreement with the first two excited states only. Neither of the last two papers gave any spectroscopic factors, hence a comparison of the experimental spectroscopic factors for the ground and the first two excited states was done with the values obtained from the simple rotational model using equation 2.7.9. The Nilsson orbitals in the s-d shell are shown in figure 7.3.3. The table 7.2.5 shows the comparison for various deformations. It can be seen that no single value of β gives agreement with the spectroscopic factors for all the three states (discussions limited to $\ell=0$ components in case of the ground and the 0.71 MeV state). This is of course, not surprising because both the neutron-proton interaction and the rotation particle coupling were not considered. The experimental spectroscopic factor for the 0.67 MeV T=1 first excited state is in excellent agreement with the theoretical value of the spectroscopic factors, for $\beta = 0.1$, the value quoted by Picard and De Pinho [Pi66].

Table 7.2.5

Comparison between experimental and rotational model spectroscopic factors.

Level MeV	j^{π},T	Rotational Configuration Ω_1, Ω_2	L Transfer	C^2S a) Expt.	C^2S Rot. Model β=0.0	0.1	0.2	0.3
0.0	1^+	$\frac{1}{2}$(No9)$\uparrow$, $\frac{1}{2}$(No9)$\uparrow$ K = 1	0	0.542	0.667	0.433	0.186	0.091
			2	0.65	0.0	0.03	0.077	0.094
0.67	$0^+,1$	$\frac{1}{2}$(No9)$\uparrow$, $\frac{1}{2}$(No9)$\downarrow$ K = 0	2	0.62	1.0	0.65	0.28	0.14
0.71	1^+	$\frac{1}{2}$(No9)$\uparrow$, $\frac{1}{2}$(No9)$\downarrow$ K = 0	0	0.107	0.334	0.22	0.09	0.05
			2	0.324	0.0	0.06	0.15	0.19

7.2.6 Conclusion

The reaction $^{29}Si(^{3}He,d)^{30}P$ was studied at an incident energy of 14.0 MeV. Angular distributions for the transitions to 16 states up to 4.23 MeV were determined and spectroscopic factors were extracted using the DWBA method.

A spin assignment of 1^+ has been made to the 3.02, 3.73 and 4.14 MeV states. Alternative assignments of $(1^+, 2^+)$ were made to the 2.72, 3.84 and 4.23 MeV states. The state at 2.84 MeV was assigned alternative spins of $(0^+, 1^+)$.

The experimental spectroscopic factors have been compared with various model calculations. Spectroscopic factors from shell model calculations by Glaudman [Gl64] were in good agreement with the experimental values for the 0.68 and 2.94 MeV T=1 states. A similar agreement with the ground state transition could be obtained by assuming an inversion in level order between the first excited (1^+) and the ground state (1^+). No discrepancy of the spectroscopic factors between the T=0 and T=1 transitions have been noticed from the shell model considerations.

The simple strong coupling rotational model can not explain the spectroscopic factors even for the lowest three states.

7.3 The $^{25}Mg(^{3}He,d)^{26}Al$ reaction.

7.3.2 Introduction

The reasons for this study have already been noted in the introduction to this chapter. The energy levels of the self conjugate nucleus ^{26}Al are well established from the studies of the $^{24}Mg(^{3}He,p)^{26}Al$, $^{27}Al(^{3}He,\alpha)^{26}Al$ [Hi59], $^{25}Mg(p,\gamma)^{26}Al$ [Ho63] reactions. It has been reported in a recent work by Hausser et al. [Ha68] that the 2.07 MeV level is a triplet consisting of 2.0687 (3^+), 2.0695 (2^+,1) and 2.0717 (1 or 2) MeV states. Spins and parities for the states up to 2.37 MeV were assigned from β-decay, (p,γ) and triple correlation experiments [Ho63, Ne62, Gr64]. Alternative assignments of (2^+,3^+) were made by Weidinger et al. [We68] to 2.55, 2.92 MeV states.

The reaction $^{25}Mg(^{3}He,d)^{26}Al$ was studied by Weidinger et al. at an incident energy of 12.0 MeV up to an excitation of 4.2 MeV. In the other previous study [Si66] transitions to only a few low lying states were observed.

On several occasions attempts were made to explain energy levels and other properties of ^{26}Al from the rotational model [Ho63, Pi66]. The calculations by Picard and De Pinho [Pi66] which included residual neutron-proton interaction gave good agreement with the low lying states. However, as no spectroscopic factors were given in this paper, the comparison with the rotational model is limited to a simple strong coupling Nilsson model in parallel with Weidinger et al. [We68].

Shell model calculations by Wildenthal [Wi68] in the s-d shell did not succeed in the case of ^{26}Al. In an intermediate coupling calculation by Bouten et al. [Bo67] of the energy levels as a function of a parameter which measured the relative strengths of the spin orbit and central force, the lowest levels were well predicted. As spectroscopic factors were also not reported in this work, no comments can be made on the goodness or otherwise of the wave functions involved.

7.3.2 Data

The reaction ^{25}Mg(^{3}He,d)^{26}Al was studied at an incident energy of 14.0 MeV. Transitions to all the states in the residual nucleus up to an excitation energy of 3.16 MeV were observed and the angular distributions for all these transitions were measured. The 2.07 MeV triplet was not resolved.

The Harwell multigap spectrograph was used in the experiments. The properties of the target used has been described in table 2.4.1. The overall resolution obtained was ~ 60 KeV. The main contributions to the resolution came from the target thickness and the beam geometry, which had to be relaxed due to the low intensity of the beam available. The treatment of data from multigap experiments have already been described in section 4.5.

Due to instrument malfunction the results of the normalization experiments turned out to be erroneous, so normalization of the data was done assuming the ground state spectroscopic factor to be the same as that of Weidinger et al.

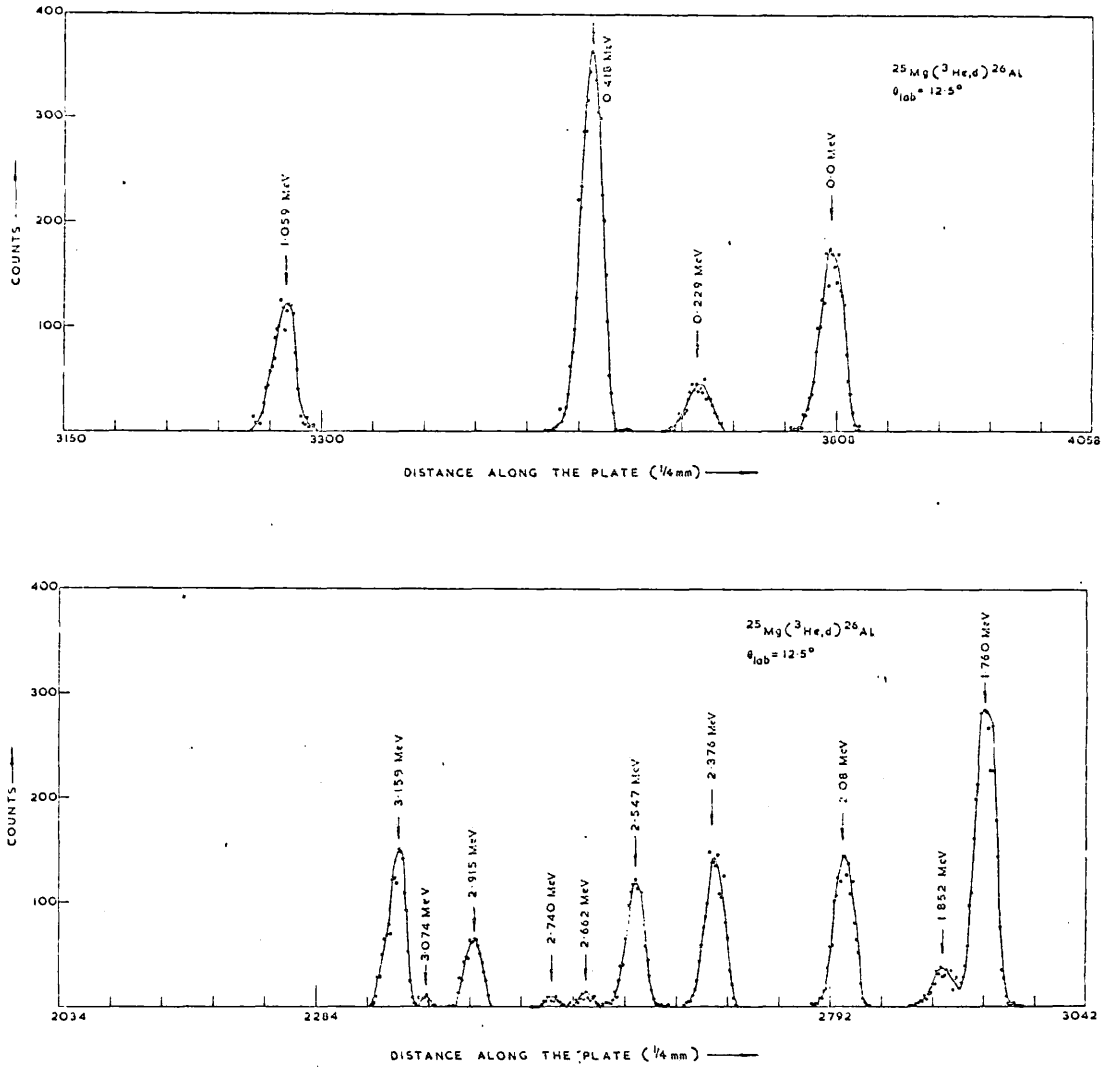

Fig: 7.3.1 Deuteron spectrum from the reaction $^{25}Mg(^{3}He,d)^{26}Al$ obtained with multigap spectrograph.

A spectrum of the deuterons at 12.5^{o}(Lab) i.e. from the 2nd channel is shown in the figure 7.3.1. Figures 7.3.2 show the angular distributions of the observed states together with the appropriate DWBA calculations.

7.3.3 DWBA Calculations

DWBA calculations were performed for the observed transitions using the parameters shown in the table 7.2.1. The separation energy prescription was used for the bound state form factors for all the transitions. Pure ℓ=2 DWBA calculations fitted fairly well the 0.0, 0.229, 1.060, and 2.74 MeV states, for all the other states a combination of ℓ=0 and ℓ=2 DWBA distributions were required to obtain an acceptable fit.

Conservation of angular momentum and parity allows ℓ=0 stripping to lead to only 2^{+} and 3^{+} final states because the ground state spin of ^{25}Mg is $5/2^{+}$. The ℓ=0 admixture limits the spins and parities of 2.66 and 3.07 MeV states to 2^{+} or 3^{+} for which no previous assignments exist. Similarly the pure ℓ=2 transition to the 2.74 MeV state fixes the parity to be positive.

The experimental angular distributions together with appropriate DWBA calculations are shown in the figures 7.3.2.

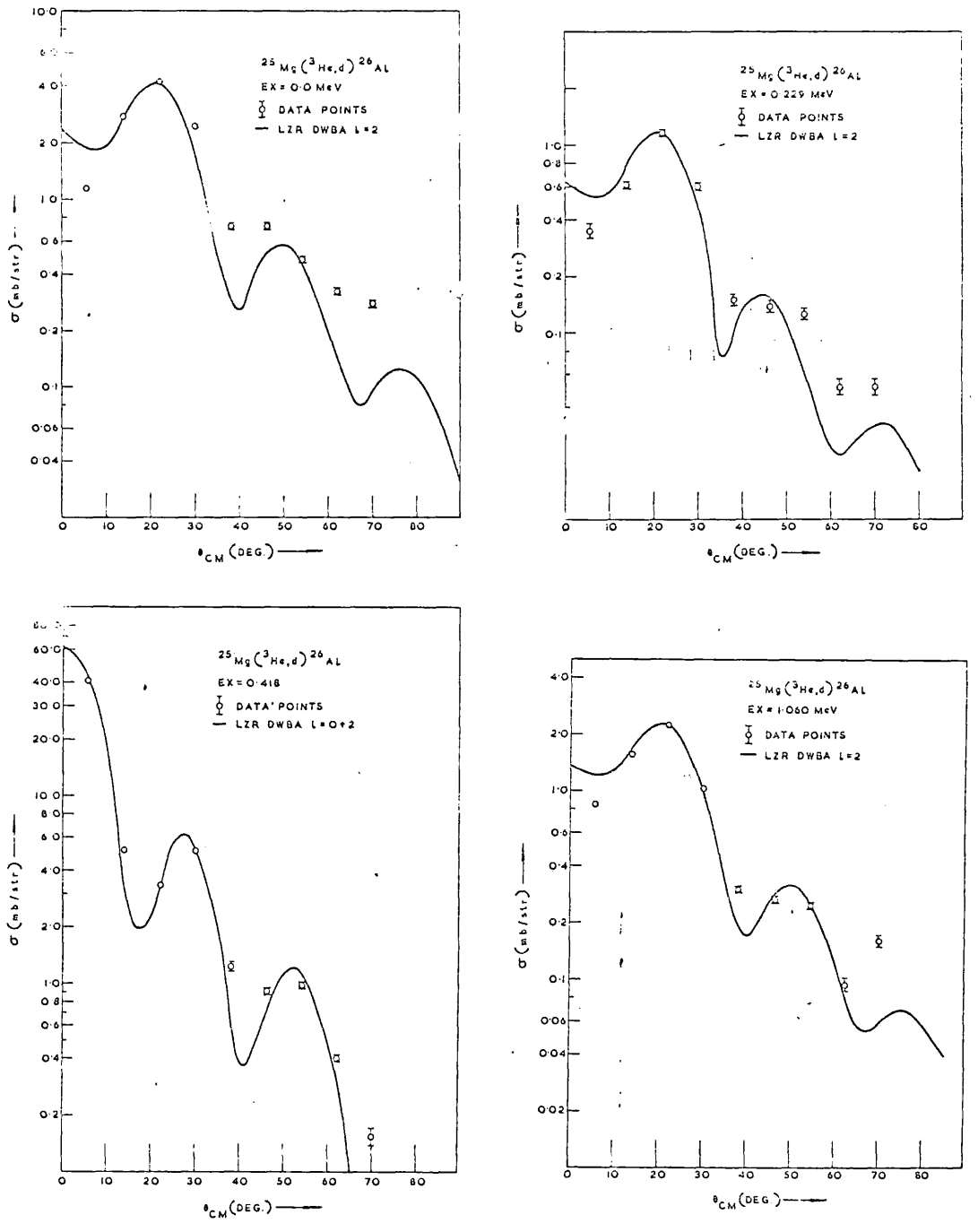

Fig: 7.3.2 (^{3}He,d) angular distributions along with DWBA fits.

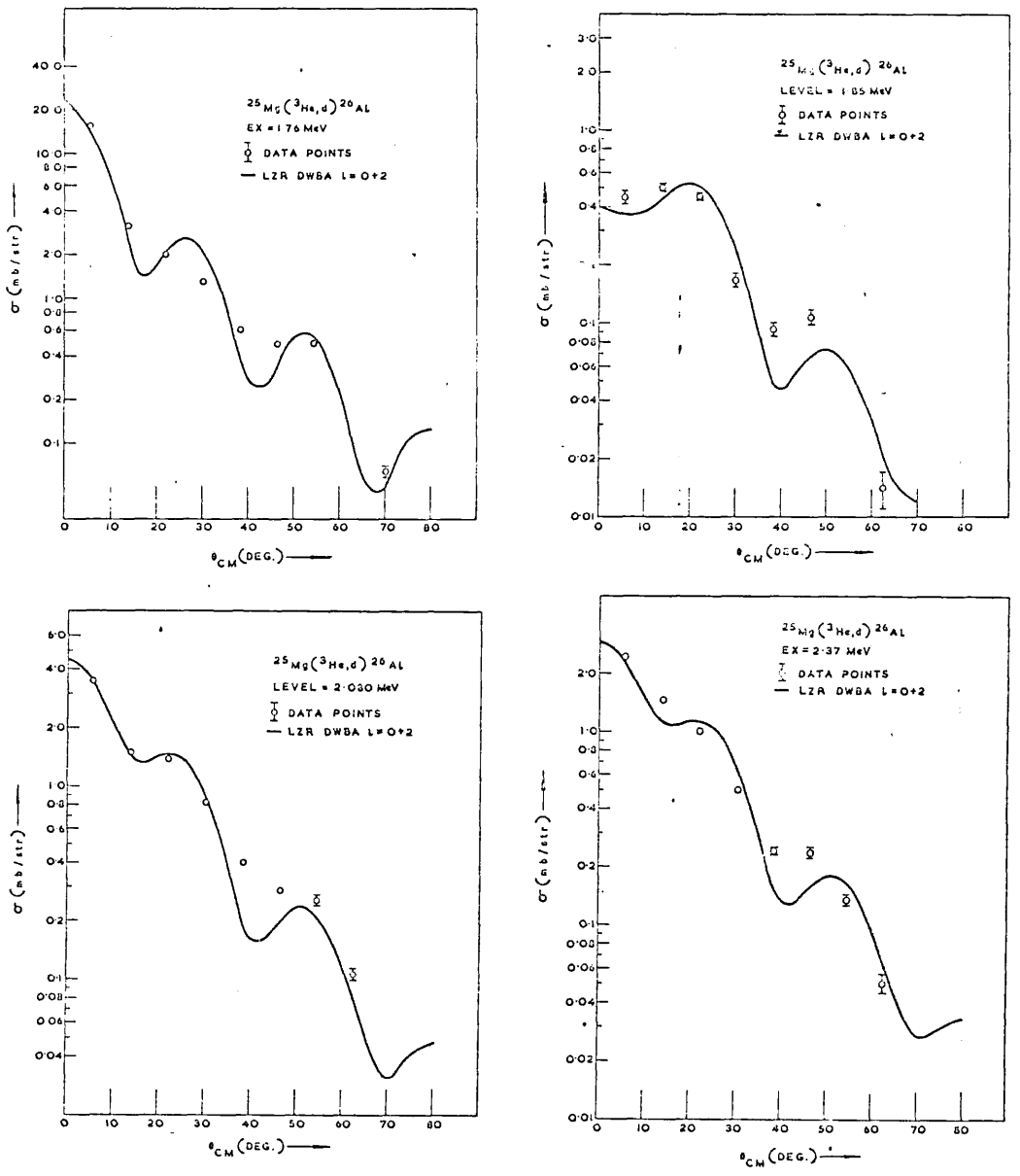

Fig: 7.3.2 continued.

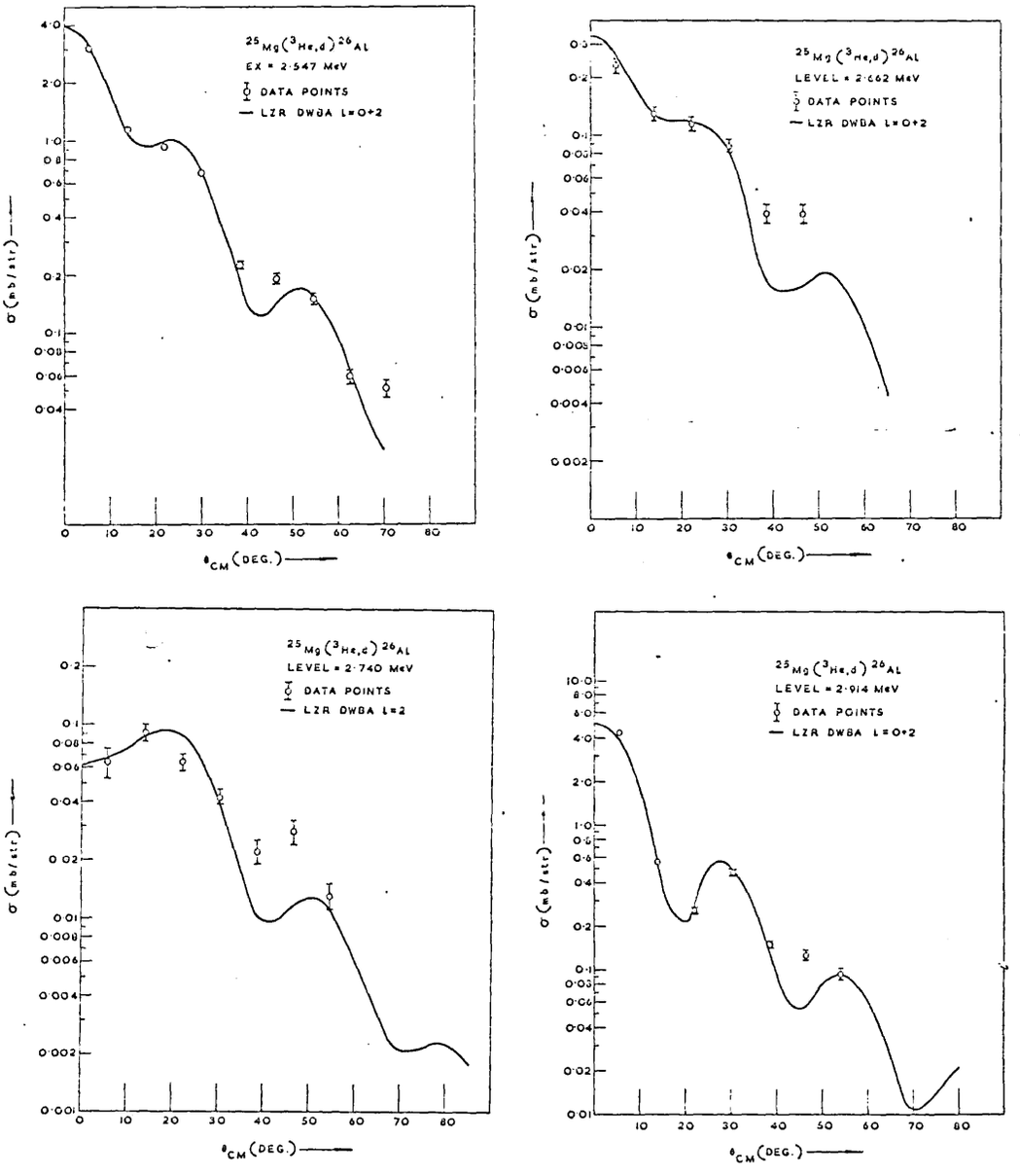

Fig: 7.3.2 continued.

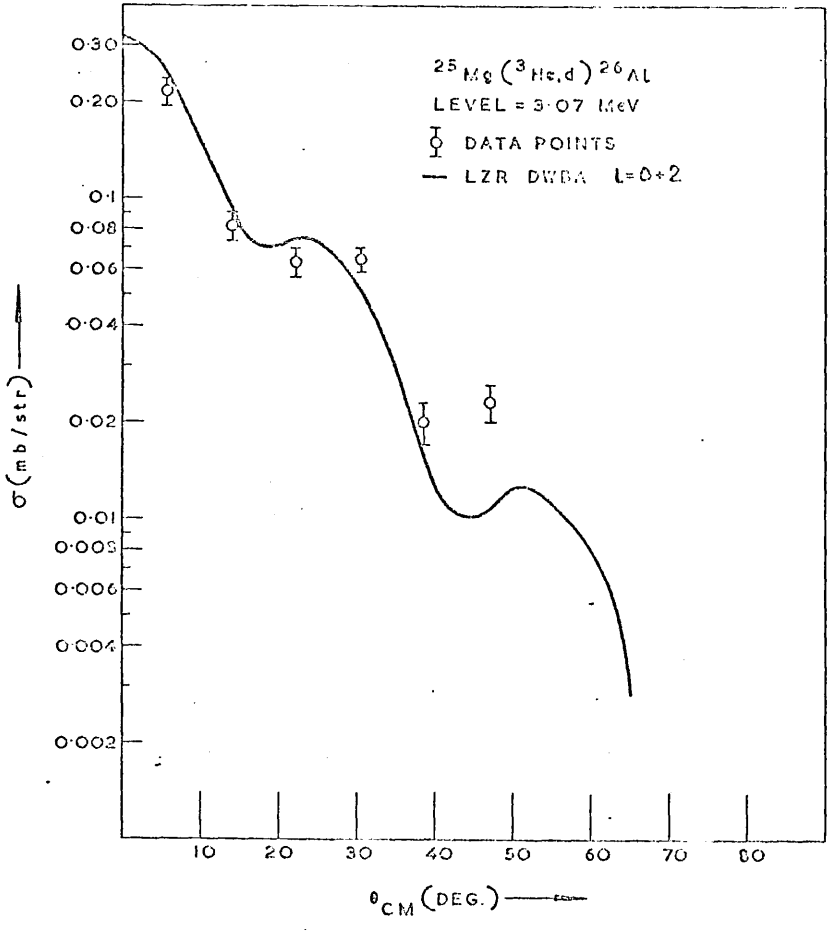

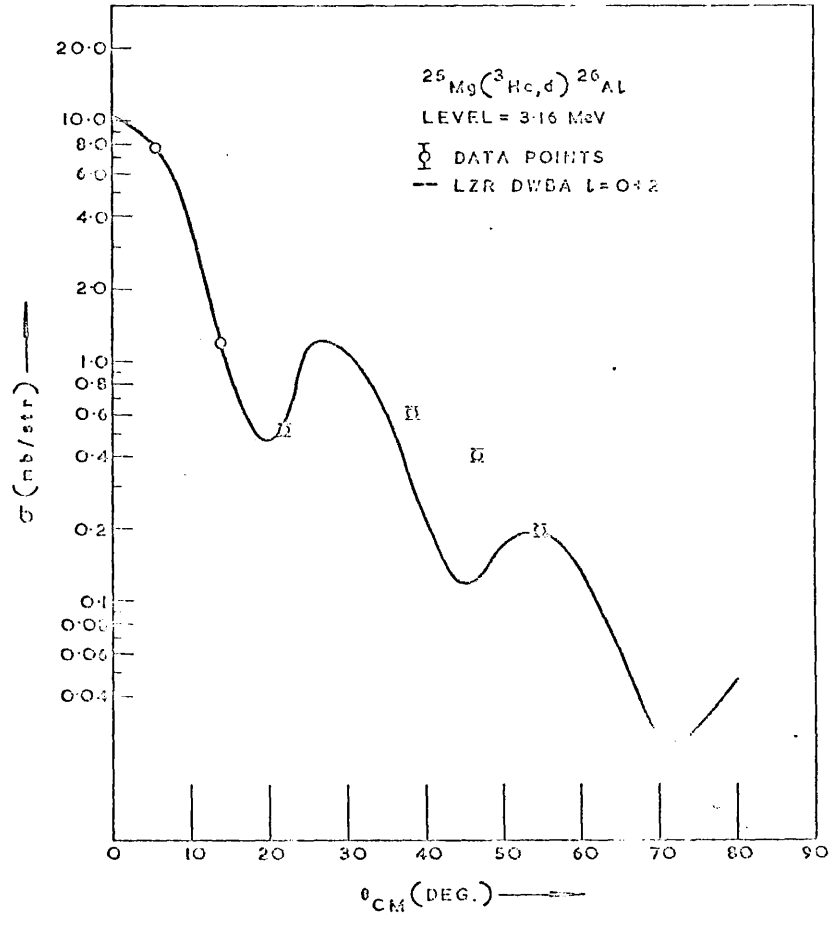

Fig. 7.3.2. continued.

Table 7.3.1

Parameters used in $^{25}Mg(^{3}He,d)^{26}Al$ DWBA calculations.

Channel	U MeV	R_u fm	A_u fm	W MeV	R_w fm	A_w fm	R_c fm
$^{26}Al+d$ a)	73.9	1.63	0.52	23.85	1.63	0.52	1.3
$^{25}Mg+^{3}He$ b)	174.15	1.10	0.764	17.96S	1.631	0.75	1.3
$^{25}Mg+p$ c)	-	1.2	0.65	-	-	-	1.3

a) [Gl65] - ($^{26}Mg+d$) parameters at 10.0 MeV

b) This work - ($^{25}Mg+^{3}He$) parameters at 14.0 MeV (c.f. table 5.5.2)

c) Potential depth was varied to suit the binding energy condition.

The spectroscopic factors obtained in this work together with the values by Weidinger et al. [We68] are shown in table 7.3.2. For the states with non-unique spins, only the quantities $(2J_f+1)C^2S$ are shown in the table. The spectroscopic factors from this work are in excellent agreement with the values at Weidinger et al. [We68] except in the case of the 2.91 and 3.16 MeV states. In the later case the values differ by a factor of ~2.5.

Table 7.3.2

Spectroscopic factors from $^{25}Mg(^{3}He,d)^{26}Al$ reaction.

Level MeV	$j^{\pi};T$	L Transfer	$(2J_f+1)C^2S$ a) $\ell=0$	$\ell=2$	C^2S a) $\ell=0$	$\ell=2$	$(2J_f+1)C^2S$ b) $\ell=0$	$\ell=2$	C^2S b) $\ell=0$	$\ell=2$
0.0	5^+	2	–	9.6	–	0.87	–	9.6	–	0.87
0.229	$0^+;1$	2	–	2.44	–	2.44	–	2.46	–	2.46
0.418	3^+	0,2	4.22	1.40	0.60	0.20	3.86	0.0 ± 3.5	0.55	0.0 ± .5
1.060	1^+	2	–	4.19	–	1.40	–	4.20	–	1.40
1.76	2^+	0,2	1.10	1.93	0.22	0.39	1.32	3.2	.26	0.65 ± 0.25
1.85	3^+	0,2	0.0033	0.82	0.0005	0.12	≤.04	0.70		
2.08	Triplet including $2^+,1$	0,2	0.22	2.01	–	–	0.22	2.76		
2.37	3^+	0,2	0.13	1.54	0.018	0.22	0.20	2.28	0.029	0.33
2.55	$2^+,3^+$	0,2	0.21	1.17	–	–	.25	2.22	–	–
2.66	$2^+,3^+$ *	0,2	0.016	0.15	–	–	–	–	–	–
2.74	$?^+$ *	2	–	0.12	–	–	–	–	–	–
2.91	$2^+, 3^+$	0,2	0.33	0.13	–	–	0.50	0.7±.4		
3.07	$2^+, 3^+$*	0,2	0.017	0.08	–	–	–	–	–	–
3.16	2 ; 1	0,2	0.67	0.31	0.13	0.061	1.68	3.2±1.6	0.34	0.65±0.3

a) This work
b) [We68] at 12.0 MeV

* Assignment from this work.

7.3.4 Discussion .

In this section the implications of the experimental spectroscopic factors are discussed.

Rotational models and the spectroscopic factors.

Spectroscopic factors from the strong coupling rotational model, with prolate deformation for ^{26}Al, were used for comparison with the experimental work of Weidinger et al. The application of the strong coupling Nilsson model to the ^{26}Al case was introduced earlier by Horvat et al. [Ho63] in connection with (p,γ) work. The schematic diagrams of the Nilsson orbitals in the s-d shell and the ground state Nilsson configuration of ^{26}Al are shown in the figure 7.3.3 for prolate deformation. The spectroscopic factors quoted here are the same as Weidinger et al, which were calculated using the Satchler formula (i.e. equation 2.7.9). Table 7.3.3. shows the measured and the calculated spectroscopic factors each multiplied by $[(2J_f+1)/(2J_i+1)]C^2$ together with the values by Weidinger et al. The configuration of K=5 and two K=0 bands for the ground and the first and third excited states respectively is due to Horvat et al. These states should be pure Nilsson configurations and there should be no admixtures because no other low lying states with the same spin and parity are predicted. The theoretical and the experimental values of the spectroscopic factors for these 3 states are in agreement within the uncertainty of DWBA calculations. For this work only the comparison between the relative values is important as the ground state was normalized to the value by Weidinger et al. One point about this agreement is that it

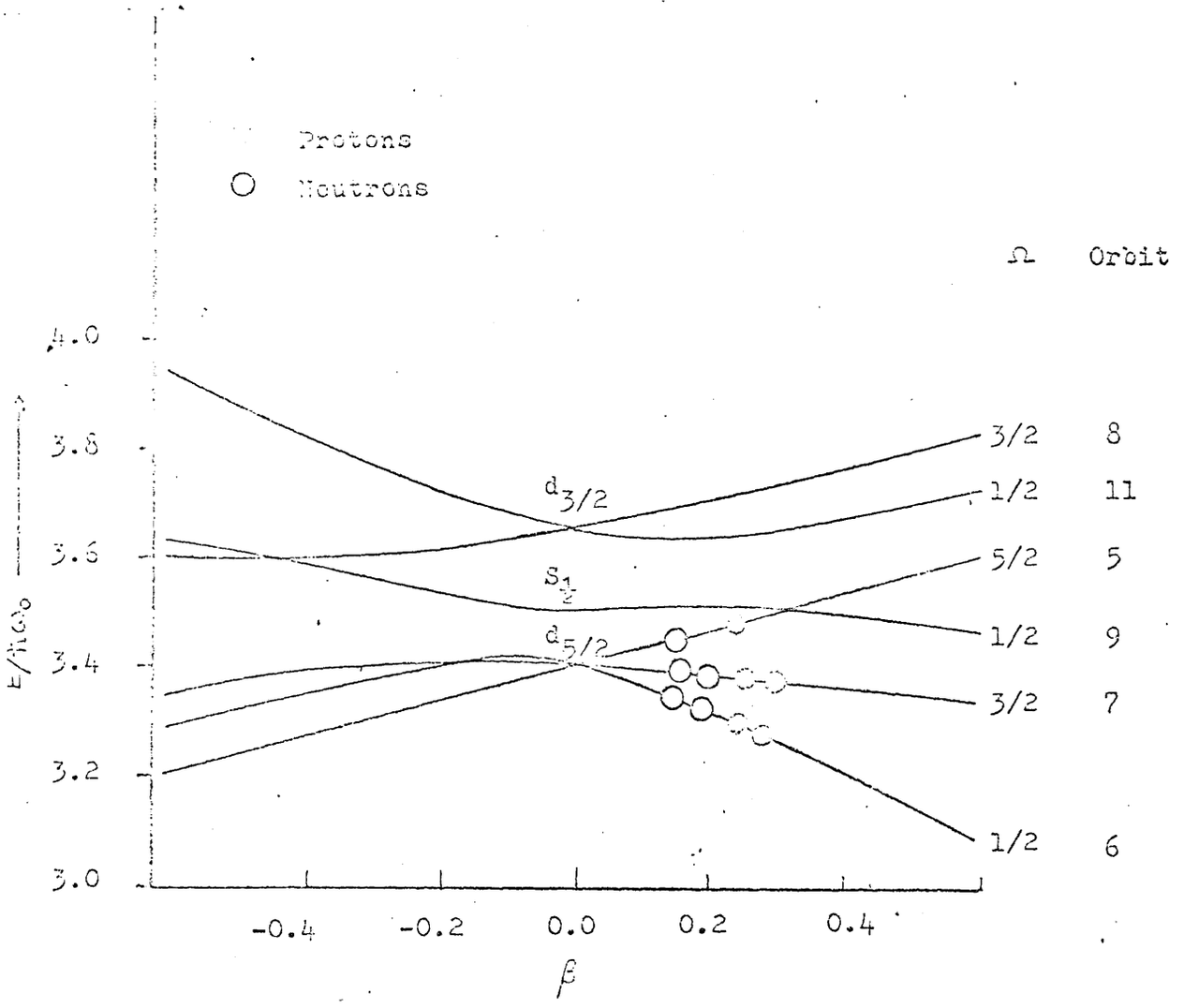

Fig: 7.3.3 Nilsson orbitals in s-d shell and schematic ground state configuration of ^{26}Al.

Table 7.3.3

Comparison between rotational model and experimental spectroscopic factors.

Level MeV	$j^{\pi};T$	Rotational Configuration Ω_1 , Ω_2	L Transfer	$[(2J_f+1)/(2J_i+1)]\,C^2S$					
				Expt. a)	Expt. b)	Rot. Model $\beta=0.1$	Rot. Model $\beta=0.2$	Rot. Model $\beta=0.3$	Rot. Model $\beta=0.4$
0.0	5^+	$\frac{5}{2}$(No5)$\uparrow$, $\frac{5}{2}$(No5) $\uparrow$	2	0.84	0.80	1.0			
0.23	$0^+,1$	$\frac{5}{2}$(No5)$\uparrow$, $\frac{5}{2}$(No5) $\downarrow$	2	0.21	0.21	0.17			
0.42	3^+	$\frac{5}{2}$(No5)$\uparrow$, $\frac{1}{2}$(No9) $\uparrow$	0	0.37	0.32	0.4	0.26	0.19	0.15
			2	0.12	0.0±0.3	0.06	0.14	0.17	0.20
1.06	1^+	$\frac{5}{2}$(No5)$\uparrow$, $\frac{5}{2}$(No5)$\downarrow$	2	0.36	0.35	0.36			
1.76	2^+	$\frac{5}{2}$(No5)$\uparrow$, $\frac{1}{2}$(No9)$\downarrow$	0	0.096	0.11	0.33	0.22	0.16	0.13
			2	0.17	0.27±0.1	0.05	0.11	0.14	0.17

a) This work

b) [We68]

does not necessarily prove that the Nilsson model is applicable in the ^{26}Al case because the calculated spectroscopic factors for these states are independent of deformation.

The relative value of the spectroscopic factor for the 0.23 MeV state is rather high compared to the model value.

For the 0.42 and 1.76 MeV states configurations of $[\frac{5}{2}(\text{No5})\uparrow,\frac{1}{2}(\text{No9})\uparrow]$ and $[\frac{5}{2}(\text{No5})\uparrow,\frac{1}{2}(\text{No9})\downarrow]$ were proposed [Ho63]. The calculated spectroscopic factors for these two states for β=0.1, 0,2, 0.3, and 0.4 are shown in the table 7.3.3 along with the experimental values. It can be seen that ratio of the experimental spectroscopic factors between the two states is ~4 compared to the theoretical value of 1.2 which is almost independent of the deformation. It has been pointed out by Weidinger et al. that this disagreement might either be due to incorrect treatment of the rotation particle coupling or failure of the unified model to explain the properties of ^{26}Al nucleus.

The configuration $[\frac{5}{2}(\text{No5})\uparrow,\frac{1}{2}(\text{No11})\uparrow]$ by Horvat et al. for the 1.85 MeV state is incompatible with the (^{3}He,d) results because of the absence of a predicted strong ℓ=0 transition. The alternative proposal to assign the above configuration to 3^+ state of the 2.07 MeV triplet togather with the interpretation of the 2^+, T=1 state as rotational number of K=0 band (in analogy with ^{26}Mg) also gives too large a ℓ=0 strength for the 2.07 MeV triplet even without considering its third member.

No attempt was made to assign Nilsson configurations for the remaining states due to the difficulties arising from the following

reasons [We68] (1) the presence of a very large number of configurations, (2) absence of any reasonable procedure for obtaining level ordering and, (3) possible strong band mixing due to rotation particle coupling.

Comparison of (^{3}He,d),(d,n) and (d,p) spectroscopic factors.

A comparison of the relative spectroscopic factors for three states from ^{25}Mg(d,n)^{26}Al and ^{25}Mg(^{3}He,d)^{26}Al is shown in the table 7.3.4. It can be seen that the discrepancy reported by Siemssen et al. [Si66] and Weidinger et al. [We68] for the 0.23 MeV, T=1 state is also seen in this work.

Table 7.3.4

Comparison between relative spectroscopic factors from ^{25}Mg(d,n)^{26}Al and ^{35}Mg(^{3}He,d)^{26}Al reactions

Ex MeV	$j^\pi;T$	S_{rel} (d,n) E=5.5 MeV [a]	S_{rel} (^{3}He,d) E = 14.0 MeV [b]	E=12.0 MeV [c]
0.0	$5^+;0$	1.0	1.0	1.0
0.23	$0^+,1$	1.8	2.8	2.7
1.06	$1^+,0$	1.55	1.6	1.6

a) [Si66]

b) This work

c) [We68]

It has been shown by Tamura [Ta68] that the discrepancy between the (^{3}He,d) and (d,n) spectroscopic factors in the case of T=1 final states in ^{10}B, can be removed to a certain extent by including a correction term in the DWBA amplitude derived by using Lanes t.T interaction [La62]. This interaction effects the entrance channel in the (^{3}He,d) reaction and the exit channel in the (d,n) reaction. However it still remains to be seen how far this type of calculation can explain individual cases. The table 7.3.5 shows the comparison of the spectroscopic factors for T=1 states observed in this work with the (d,p) spectroscopic factors leading to analogue states in ^{26}Mg. From accuracy considerations the following discussions are limited to ℓ=0 spectroscopic factors for the 1.81 and 3.16 MeV states.

Table 7.3.5

Excitation MeV ^{26}Al	Excitation MeV ^{26}Mg	L	Spectroscopic factors (d,p)[a]	(d,p)[b]	(^{3}He,d)[c]	(^{3}He,d)[d]
0.23	0.0	2	1.90	1.80	2.55	2.5
2.07	1.81	0	0.02	0.018	0.047[e]*	0.044
		2	0.40	0.44	0.52	0.55
3.16	2.96	0	>0.12	0.15	0.14	0.34
		2	<0.18	0.32	0.064	0.65

a) [Cu64]
b) [Lu66]
c) This work (c.f. table 7.3.2)
d) [We68] (c.f. table 7.3.2)
e) *All strength of 2.07 state has been attributed to T=1 state.

The discrepancy seen in the spectroscopic factors for the 0.23 MeV state between the $(^3He,d)$ and (d,p) reactions, as pointed out by Weidinger et al, may arise from different bound state form factors used in DWBA calculations. If however, the ground state value is normalised to the (d,p) value, the value of the spectroscopic factor (~0.1) for the 3.16 MeV state from this work agrees with the (d,p) values, contrary to the results by Weidinger et al. The normalized value (~ 0.33) for the 2.07 MeV state is about twice the value from (d,p) reaction. The source of this difference can not be identified with any degree of reliability, due to the triplet nature of the 2.07 MeV state.

7.3.5 Conclusion

The reaction $^{25}Mg(^3He,d)^{26}Al$ was studied at an incident energy of 14.0 MeV. All the known states upto an excitation of 3.16 MeV were seen, the 2.07 MeV triplet was not resolved. Angular distributions for all the 14 transitions were measured and spectroscopic factors for the transitions were extracted using DWBA.

From the conservation of angular momentum and parity alternative assignments of $(2^+,3^+)$ were made for the 2.66 and 3.07 MeV states for which there were no previous assignments. The parity for the 2.74 MeV state was determined to be positive.

The spectroscopic factors from this work were found to be in excellent agreement with the work of Weidinger et al [We68] except in the cases of 2.91 and 3.16 MeV states. The spectroscopic factors were compared with the rotational model predictions.

The discrepancy in the relative spectroscopic factor for the 0.23 MeV state between the (^{3}He,d) and (d,n) reactions reported earlier was also observed in this work.

No discrepancy in the spectroscopic factor for the 3.16 MeV state relative to the 0.23 MeV state was found between the (^{3}He,d) and the (d,p) reactions. The larger value of relative spectroscopic factor in the case of 2.07 MeV level could not be attributed to a single cause, due to the triplet nature of the state.

7.4 The ^{29}Si(d,n)^{30}P reaction

7.4.1 Introduction

One study of this reaction at 1.4 MeV has previously been reported [Ma52]. This study was concerned with the location of energy levels of ^{30}P. The reported states were at 0.0; 0.75±0.06; 1.46±0.06 and 2.0±0.06 MeV. No spectroscopic information about the states of ^{30}P has so far been reported using the (d,n) reaction.

As information regarding the energy levels of ^{30}P has already been considered in connection with the (^{3}He,d) reaction studies (c.f. section 7.2), it is not included here. The main concern of the (d,n) study is the comparison of the spectroscopic factors obtained with the spectroscopic factors from (^{3}He,d) work reported in section 7.2

7.4.2 Data

The reaction ^{29}Si(d,n)^{30}P was studied at an incident energy of 3.0 MeV using the time of flight system. The time of flight system has been described in the section 4. The details of the experiments and treatment of data have been described in section 4.6. A spectrum

of neutrons from the reaction at 0^{o} is shown in the figure 4.6.3. Angular distributions for six cases were determined. These included the distributions for the unresolved states 0.678 and 0.709 MeV and the states 2.94 and 3.02 MeV. The angular distributions covered the region from 0^{o} to 120^{o} (Lab.).

It was not possible to determine the absolute normalization of the experimental data due to the non-availability of the absolute efficiency of the neutron detector used in the experiments and the thickness of the target. The ground state (d,n) cross-section at 0^{o} was normalized to yield the same spectroscopic factors as the (^{3}He,d) ground state transition. This is illustrated in figure 7.4.1(a). Attempt was also made to take into account the compound nucleus contributions in the ground state cross-section, using Hauser-Feshbach (HF) calculations, in order to find absolute normalization of the data. This is illustrated in the figure 7.4.1(b). However, this procedure was not adopted finally because the comparison of the shape of the angular distribution including the HF contribution with the experimental angular distribution indicated that the compound nucleus contribution was over estimated by the HF calculation. The HF calculations are discussed in detail in the next section.

The angular distributions along with the DWBA curves are shown in the figures 7.4.1.

7.4.3 Hauser-Feshbach and DWBA Calculations.

A Hauser-Feshbach calculation using the programme of Wilmore [Wi66,Wi69] with the correction for level width fluctuations was carried out for the reaction ^{29}Si(d,n)^{30}P. The channels included in

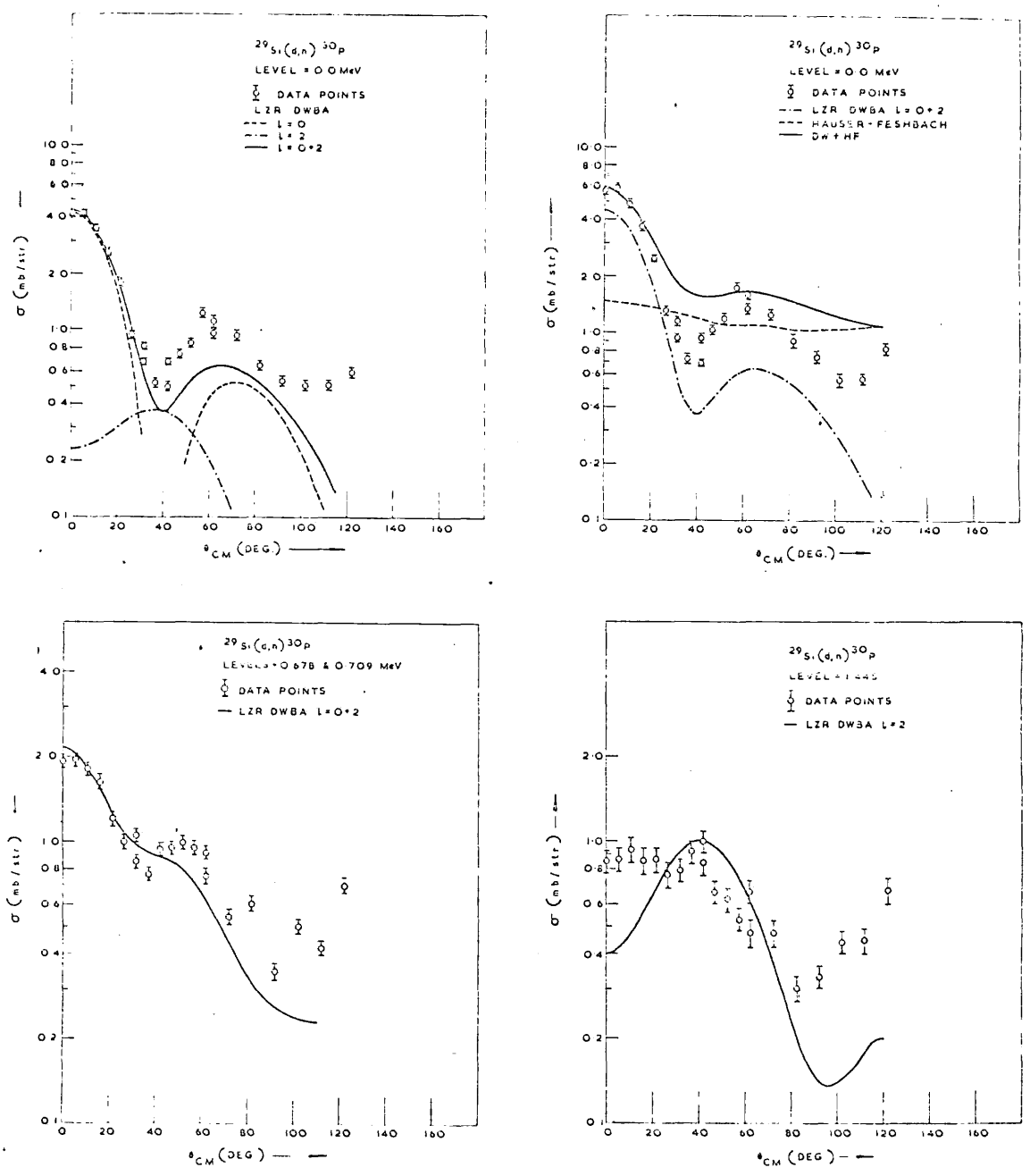

Fig: 7.4.1 (d,n) angular distributions along with DWBA fit.

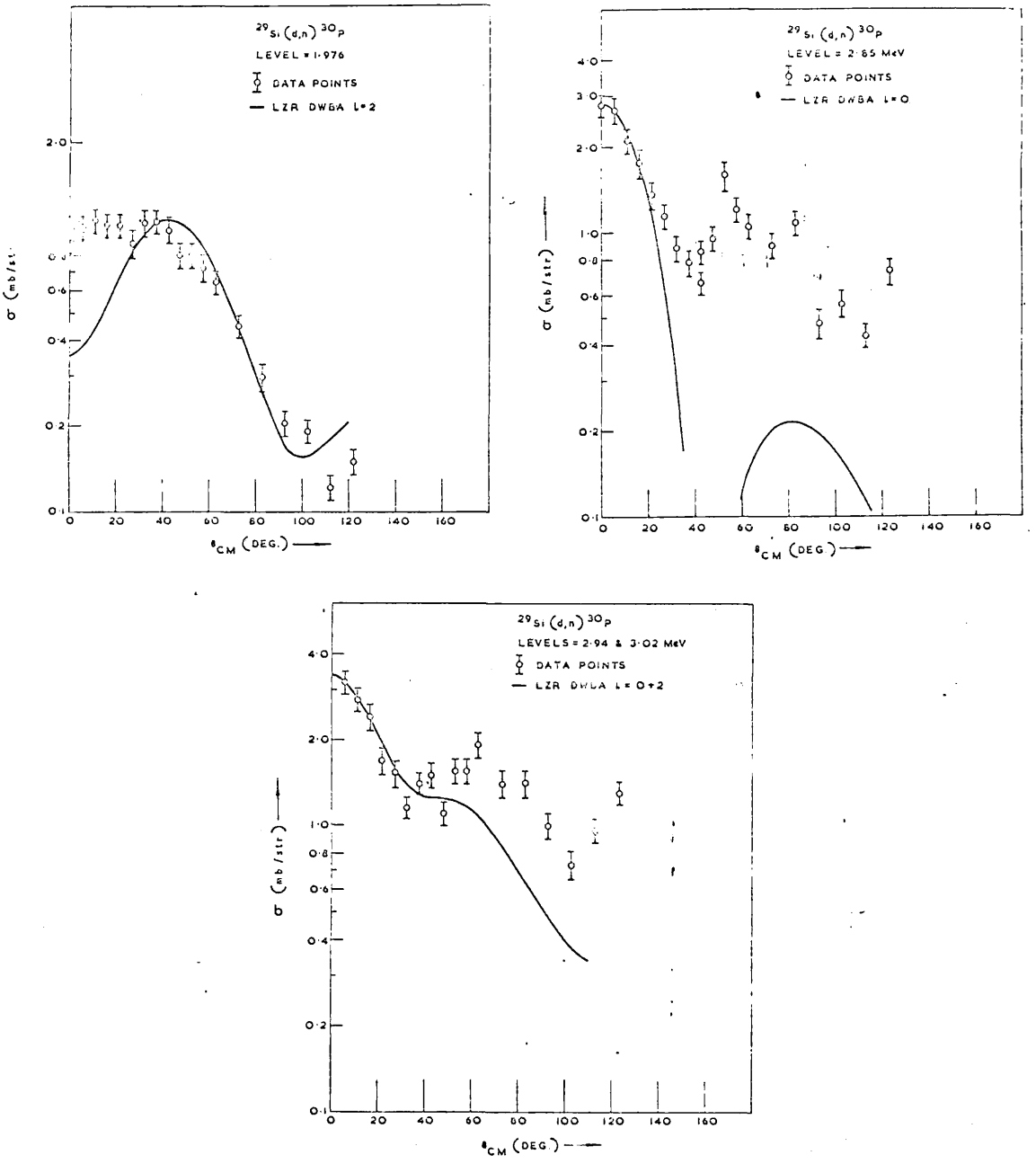

Fig: 7.4.1 continued.

the calculations were (d,d);(d,p);(d,α);(d,T) are (d,n). The optical potential parameters used are shown in table 7.4.1.

Table 7.4.1

Optical potential parameters used in Hauser-Feshbach and DWBA calculations

Channel	U MeV	R_u fm	A_u fm	W MeV	R_w fm	a_w fm	R_c fm
$^{29}Si + d$ a)	101.7	1.10	0.815	21.22D	1.376	0.556	1.3
$^{30}Si + p$ b)	42.03	1.32	0.62	3.65D	1.32	0.65	1.3
$^{30}p + n$ c)	37.21	1.32	0.62	3.55D	1.32	0.65	1.3
$^{27}Al + ^{4}He$ d)	100.0	1.570	0.6	15.0 S	1.57	0.6	1.3
$^{28}Sl + c$ e)	188.99	1.25	0.601	22.27S	1.327	0.813	1.3

a) (^{31}P +d) parameters at 11.5 MeV. Found by fitting data by Denortier et al [De61].

b) [Pe62]

c) (^{29}Si + n) parameters at 4.1 MeV [Pe67]

d) (^{27}Al + ^{4}He) parameters at 18.0 MeV [Ig59]

e) (^{29}Si + ^{3}He) parameters at 14.0 MeV. This work [c.f. table 5.5.2]

Most of the relevant final states given by Endt and Van der Leun [En67] were included. Some of the states had to be left out because no spin assignments were available for them. For ^{29}Si the states were 0.0($\frac{1}{2}^+$); 1.273 ($\frac{3}{2}^+$); 2.032 ($5/2^+$) and 2.427 MeV($\frac{3}{2}^+$). For ^{30}Si the states were: 0.0(0^+); 2.232 (2^+);3.507(2^+); 3.767(1^+);(3.786(0^+);4.408(2^+);5.222(3^-); 5.222(3^-); 5.274(4^+); 5.480(3^-);5.611(2^+); 6.528(2^+); 6.630(0^+) and 6.735 MeV (1^-). The states of ^{27}Al were: 0.0($5/2^+$), 0.842($\frac{1}{2}^+$);1.013($\frac{3}{2}^+$); 2.209($7/2^+$); 2.732($5/2^+$);2.979($\frac{3}{2}^+$); 3.0($9/2^+$) and 3.678 MeV ($\frac{1}{2}^+$). Only the ground state was included for ^{28}Si because of the large negative Q-value (-2.218) of the (d,T) reaction. For ^{30}P the states were: 0.0(1^+);0.678(0^+); 1.455(2^+);1.976(3^+); 2.539(3^+);2.72(2^+),2.84(1^+), 2.94(2^+);3.02(1^+), 3.73(1^+); 3.84(2^+); 4.14(1^+),4.18(2^+) and 4.23 MeV (2^+).

As has already been pointed in section 7.4.2, the HF calculations over-estimated the compound nucleus contributions to the (d,n) cross-sections. This was most likely to be due to the facts that (d,p) reaction had very high positive Q-value (8.4 MeV) and all the open channels in (d,p) i.e. upto an excitation of ~11 MeV were not included. They could not be incorporated in the calculations due to the non-availability of energy level data for ^{30}Si upto such a high excitation.

The DWBA calculations were done also using the optical potential parameters in table 7.4.1 for the (^{29}Si+d) and (^{30}P+n) channels. In the extraction of the spectroscopic factors, subtraction of the compound nucleus contributions were not done because of the problems in the HF calculations mentioned earlier. The agreement between the distributions from the DWBA calculations and the experiments is poor. The ℓ values

transferred in the (d,n) reaction were the same as in (^{3}He,d) case i.e. as to be in section 7.2. For the 2.84 MeV level the transition should be pure ℓ=0 from (^{3}He,d) considerations but the fit with the DWBA shows very poor agreement for $\theta \geq 20^{\circ}$. For the 1.445 and 1.85 MeV states only ℓ=2 transitions are allowed. The angular distributions for these two states also show poor agreement with the DWBA distributions. For the above three states the spectroscopic factors were found by matching the principal maxima in the experimental angular distributions with the DWBA distributions.

For the remaining two distributions i.e. for the unresolved 0.678 and 0.709 MeV and 2.94 and 3.02 MeV states, the spectroscopic factors were calculated using the least square fitting procedure described in section 4.8. The consequences of the fitting procedure was also pointed out in the section 4.8. However, we note here that due to poor agreement even the pure transitions and the DWBA distributions and the small magnitude of ℓ=2 cross-sections compared to ℓ=0 cross-sections, the spectroscopic factors for the ℓ=2 components extracted by using the fitting procedure are unreliable and possibly correct only within a factor of 3 or so. The spectroscopic factors from the (d,n) studies multiplied by $(2J_f+1)$ are shown in table 7.4.2 along with the values from (^{3}He,d) studies.

Table 7.4.2

Spectroscopic factors from (d,n) and (^{3}He,d) reactions leading to ^{30}P.

Level	$j^\pi;T$	(d,n) $(2J_f+1)\ C^2S$ $\ell = 0$	(d,n) $(2J_f+1)\ C^2S$ $\ell = 2$	(^{3}He,d) a) $(2J_f+1)\ C^2S$ $\ell = 0$	(^{3}He,d) a) $(2J_f+1)\ C^2S$ $\ell = 2$
0.0	1^+	1.65	1.97	1.65	1.97
0.678	$0^+;1$	0.45	4.2	0.952	0.97
0.709	1^+				
1.445	2^+	–	3.81	–	2.47
1.98	3^+	–	3.4		0.585
2.84	$(0^+;1^+)$	0.19	–	0.45	–
2.94	$2^+,1$	0.19	2.6	0.18	2.34
3.02	1^+				

a) This work (c.f. table 7.2.2)

7.4.4 Discussions

The discussions here are limited to the comparison between the spectroscopic factors from (^{3}He,d) and (d,n) studies as the other aspects have already been considered in section 7.2. The comparisons are only meaningful for ℓ=0 spectroscopic factors, in cases where the angular distributions are due to combinations of ℓ=0 and ℓ=2 distributions, and as the (d,n) ground state spectroscopic factors were normalised to the (^{3}He,d) ground state value (e.g. table 7.4.2), only the relative (d,n) spectroscopic factors are of importance.

A comparison of the spectroscopic factors in the table 7.4.2 shows that the spectroscopic factor for the unresolved 0.678 and 0.709 MeV states in (d,n) case is smaller by a factor of ~2 from the (^{3}He,d) case. This is most probably the same effect as observed in the 0.23 MeV state in the ^{26}Al case. Of course residual doubt as to whether to attribute the whole decrease to the 0.678 MeV (0^+; T=1) state still remains. For the other T=1 state at 2.94 MeV, no significant difference is seen between the (d,n) and (^{3}He,d) spectroscopic factors. However things are uncertain for this case because the 2.94 MeV (2^+;T=1) and 3.02 MeV (1^+; T=0) states are not resolved and the spectroscopic factor involved is due to ℓ=2 transfer. As has been pointed out in section 7.3, the discrepancy between spectroscopic factors from (^{3}He,d) and (d,n) reactions for $T_>$ states can be removed to some extent by considering isospin coupling in the incident channel for (^{3}He,d) and in the out going channel for the (d,n) reaction [Ta68].

For the 1.445 MeV (2^+; T=0) state the (d,n) and (^{3}He,d) spectroscopic factors are in agreement considering that the compound nucleus effect has not been taken into consideration in the extraction of (d,n) spectroscopic factors. For the 1.98 MeV (3^+; T=0) state the (d,n) spectroscopic factor is too large even if some allowance is made for [illegible] effect. For the 2.84 MeV state the (d,n) spectroscopic factor is smaller by a factor of 2 from the (^{3}He,d) value.

7.4.5 Conclusions

The ^{29}Si(d,n)^{30}P reaction was studied at an incident energy of 3.0 MeV using the time of flight technique. The reaction proceeded mainly through a direct process. Angular distributions for transitions to 8 levels (6 groups) upto an excitation of 3.02 MeV were determined and the spectroscopic factors were extracted for the transitions using the DWBA theory. The spectroscopic factors were compared with those obtained from the (^{3}He,d) reaction. The discrepancy of spectroscopic factors for the T=1 states between the (d,n) and (^{3}He,d) is most probably present.

APPENDIX A

Kinematics of two body nuclear reactions.

Kinematical quantities of the two body nuclear reactions which were useful in the work are given below. Masses, Q-value and the angles for such a two body reaction are defined in the figure: A1. The formulae were mostly taken from the compilation by Marion et al. [Ma68].

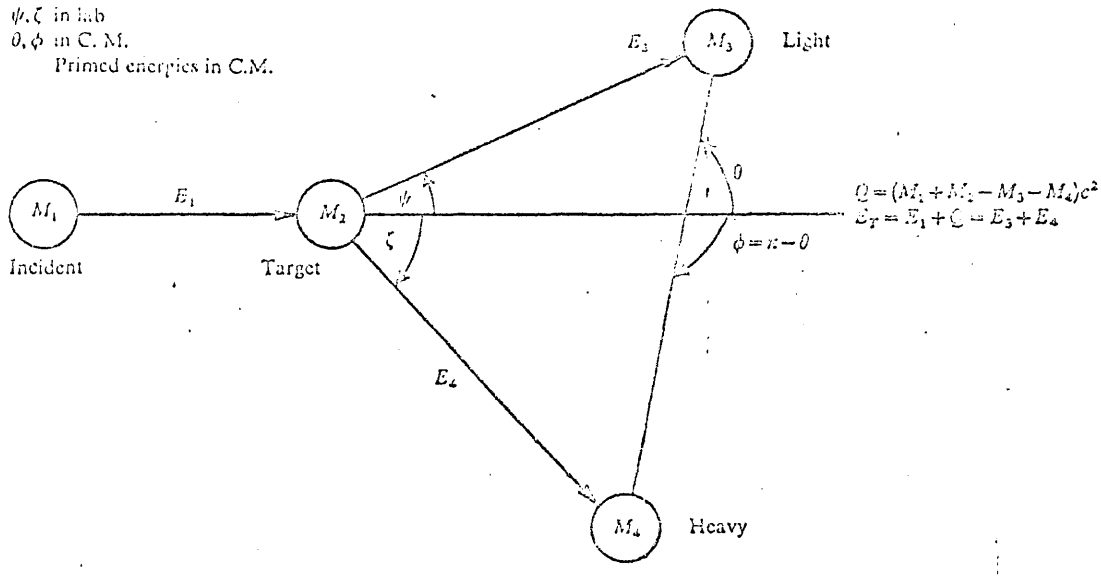

Figure: A1 – Schematic diagram of a two body reaction.

We define:

$$A = \frac{M_1 M_4 (E_1/E_T)}{(M_1+M_2)(M_3+M_4)} \quad , \quad C = \frac{M_2 M_3}{(M_1+M_2)(M_3+M_4)} \left(1 + \frac{M_1 Q}{M_2 E_T}\right) = \frac{E_4}{E_T}$$

$$B = \frac{M_1 M_3 (E_1/E_T)}{(M_1+M_2)(M_3+M_4)} \quad , \quad D = \frac{M_2 M_4}{(M_1+M_2)(M_3+M_4)} \left(1 + \frac{M_1 Q}{M_2 E_T}\right) = \frac{E_3}{E_T}$$

The above definitions lead to identities:

$$A+B+C+D = 1 \text{ and } AC=BD$$

Using the above definitions we have for the kinematical quantities:

1) CM angle of light product:

$$\sin\theta = \left(\frac{E_3/E_T}{D}\right)^{1/2} \sin\psi \qquad (A.1)$$

2) Lab angle of heavy product:

$$\sin\zeta = \left(\frac{M_3 E_3}{M_4 E_4}\right)^{1/2} \sin\psi \qquad (A.2)$$

3) Lab. energy of light product:

$$\frac{E_3}{E_T} = B + D + 2(AC)^{1/2}\cos\theta$$

$$= B\left[\cos\psi \pm (D/B - \sin^2\psi)^{1/2}\right]^2 \qquad (A.3)$$

Only the positive sign is to be used unless $B > D$ in which case

$$\psi_{max} = \sin^{-1}(D/B)^{1/2} \qquad (A.4)$$

4) Lab. energy of heavy product:

$$\frac{E_4}{E_T} = A + C + 2(AC)^{1/2}\cos\phi$$

$$= A\left[\cos\zeta \pm (C/A - \sin^2\zeta)^{1/2}\right]^2 \qquad (A.5)$$

Only the positive sign is to be used unless A > C in which case

$$\zeta_{max} = \sin^{-1} (C/A)^{\frac{1}{2}} \qquad (A.6)$$

5) Solid angle ratio for the light product:

$$\frac{\sigma(\theta)}{\sigma(\psi)} = \frac{\sin^2\psi}{\sin^2\theta} \text{ Cos } (\theta-\psi) = \frac{(AC)^{\frac{1}{2}}(D/B - \sin^2\psi)^{\frac{1}{2}}}{E_3/E_T} \qquad (A.7)$$

6) Time of flight of light particle when it is a neutron:

$$\tau(\text{ns/m}) = \frac{E_3 + 939.526}{0.2997929\ (E_3^2 + 1879.052\ E_3)} \qquad (A.8)$$

In the above equations all the masses are in amu and all the energies are in MeV.

APPENDIX B

The Computer Programs.

B.1 Kinematics program:

This program was essentially the coding of the equations in appendix A. For a given reaction A(a,b)B specified by reaction masses, incident energy, ground state Q-value and the excitation energies of the final nucleus, the programme calculated the kinematical quantities specified in appendix A. The program was written in two versions, one version was for the neutron producing reactions when time of flights were computed in addition to other quantities and the second version was for all the other reactions where time of flight data were not necessary. Upto eight incident energies and eight levels in the residual nucleus could be included in a single set of data.

B.2 Cross-section Program:

This program calculated centre of mass cross-section from the reaction yields and the yield from a Rutherford scattering experiment as explained in section 4.7 using the equation 4.7.3. The Rutherford cross-sections were calculated from the equation

$$(\sigma_R(\psi))_{Lab} = 1.296 \left(\frac{Z_1 Z_2}{E_1} \right)^2 \left[\text{Csc}^4 (\tfrac{1}{2}\psi) - 2\left(\frac{M_1}{M_2} \right)^2 \right] \text{ mb/str.} \qquad (B.2.1)$$

where Z_1 and Z_2 are the atomic numbers of the incident and the target nucleus respectively. The other quantities have the same meaning as in Appendix A.

The transformation of the cross-sections to CM system was achieved by using the equation A.7. The CM angles were calculated by using the equation A.1. The program also calculated the statistical errors in the cross-sections. It also calculated the Q-values of the reactions if E_3 was fed in or vice versa calculated E_3 if the Q-values were fed in.

B.3 Multigap spectrograph data analysis program:

This program was originally written at AWRE, Aldermaston [Ch69] and was modified to run on the Harwell IBM 360/75 machine for our purpose. The programme required in addition to the scanned data, the masses of the incident particle, out going particle and the target nucleus and the nuclear magnetic resonance frequency for the field setting of the spectrograph.

The program located the peaks in the scanned data and from the position of the peaks along the focal plane, the program calculated the energy of the particles in the peak and the absolute Q-values.

The program also integrated the peaks after straight line background subtraction if necessary, corrected the peak areas for the solid angle variation along the focal plane and also carried out the transformation to the CM system. The program also plotted the particle spectra.

B.4 Angular distribution decomposition program

This program was used to find the best mixture of two to four theoretical angular distributions to a given experimental angular distribution. For this program both the experimental and the theoretical cross-sections were required at the same set of angles. The experimental and the theoretical cross-sections are denoted below as σ (exp) and σ(Th)

Respectively. A weight was associated with each experimental point using the formula

$$W_i = \frac{\Delta\sigma_i \text{ (exp)}}{\sum_{i=1}^{m} \Delta\sigma_i} \qquad \text{(B.4.1)}$$

so that

$$\sum W_i = 1 \qquad \text{(B.4.2)}$$

where 'm' is the number of points in the angular distribution. The program minimised the function

$$S = \sum W_i(\sigma_i \text{ (exp)} - \bar{\sigma}_i) \qquad \text{(B.4.3)}$$

where

$$\bar{\sigma}_i = \sum_{n=1}^{n_{max}} a_n \sigma_n \text{ (Th)} \qquad \text{(B.4.4)}$$

where n_{max} is the number of theoretical angular distributions. The minimisation was done by using a Harwell library routine by Powell [Po65]. The quantities 'a_n' obtained in the minimisation procedure, are the required fractions of the theoretical angular distributions, for the best fit to the experimental angular distribution.

B.5 Spectrum analysis program.

The program was originally written at Hamburg University by Tapel [Te65]. It was modified to run on the Harwell IBM 360/75 computer for our purpose.

The program was capable of dealing with spectra up to 4000 channels. Various input media such as paper tape, cards, magnetic tape etc. could be used for the data. The initial step consisted in breaking off a given spectrum into regions less than 512 channels which could be done automatically or by feeding in breaking off channels. The regions were so chosen that at both ends there were a few points through which a background could be fitted using the least square method. Three options were available for choice of background i.e. linear, parabolic and cubic.

After the background subtraction the program fitted a given line shape to single or overlapping peaks using least square technique. The number and the position of the peaks in a region of overlapping peaks could be decided by the program. However in complex cases there were also provision for feeding in the approximate peak positions and other parameters which resulted in considerable saving in computer time.

The program gave areas of the peaks analysed and also the χ^2 of fit to the experimental spectrum. The program also plotted on top of each other the experimental and the fitted peaks and the background points, so that a quick eye estimation of the goodness of the fit could be done.

B.6 Legendre polynomial fitting program.

The purpose of this program was to interpolate values of the differential cross-sections at regular angular intervals as the experimental cross-sections were normally available at irregular intervals. For the fitting purpose a weighing factor was attached to each experimental point $\sigma_i(\theta)$ according to the formula,

$$W_i = \frac{\Delta\sigma_i}{\sum_{i=1}^{n} \Delta\sigma_i} \qquad \text{(B.6.1)}$$

so that

$$\sum W_i = 1 \qquad \text{(B.6.2)}$$

where 'n' is the number of points in the angular distributions. The program minimised the function

$$S = \sum_{i=1}^{n} W_i \left(\sigma_i(\theta) - \bar{\sigma}(\theta)\right) \qquad \text{(B.6.3)}$$

where $\bar{\sigma}(\theta)$ are given by

$$\bar{\sigma}(\theta) = \sum_{\ell=1}^{m} a_\ell \, P_\ell (\cos\theta) \qquad \text{(B.6.4)}$$

where 'm' is the degree of fit required. The Legendre Polynomials were calculated using the relations

$$P_o = 1$$

$$P_1 (\cos\theta) = \cos\theta \qquad \text{(B.6.5)}$$

$$P_\ell(\cos\theta) = (2 - \tfrac{1}{\ell}) \cos\theta \; P_{\ell-1}(\cos\theta) - (1 - \tfrac{1}{\ell}) P_{\ell-2}(\cos\theta)$$

The minimisation procedure yielded the best values of the coefficients 'a'. Using these values in the equation B.6.4 interpolated cross-sections at required angles were computed.

B.7 Optical Model Programme

This program was due to Wilmore [Wi69] . Discussions on Optical model are included in chapters II and V, so they are not considered here. The program could either be used for calculation of the cross-sections for a given set of potential parameters (including spin orbit) or could be used to fit a given set of data by varying the potential parameters using the least square method.

The program was capable of including a compound elastic cross-section in the fitting procedure either by assuming it to be isotropic or to have a specified shape. If necessary it was possible to vary the magnitude of the compound nucleus cross-section to obtain the best fit to the experimental data.

The programme had also the option for using non local potential parameters.

B.8 Hauser-Feshbach programme

This programme was due to Wilmore [Wi66, Wi69]. Some comments on Hauser-Feshbach calculations are included here as Hauser-Feshbach theory has not been discussed in the text.

When a nuclear projectile is incident at low energies on a target nucleus it is either elastically scattered or absorbed to form a compound nucleus. The compound nucleus subsequently decays into one or other of the energetically allowed channels. The optical model can be conveniently used to calculate the elastic scattering angular distribution and the absorption or the compound nuclear cross-section, which is the total cross-section for all the channels.

Hauser and Feshbach [Ha52] showed that if the process of formation and decay of the compound nucleus are assumed to be independent, the use of reciprocity theorem allows the differential cross-sections in all reaction channels to be calculated as well. This calculation required the transmission coefficients of all the inverse reactions and these may be calculated using optical potentials appropriate to these reactions.

The program could calculate the Hauser-Feshbach cross-sections for any mass, charge and spins of the incident particle and target nucleus. The transmission coefficients for the incoming and all the out going channels could be fed in if they were known or they could be calculated from optical potentials. The program then calculated differential cross-section in all the two body reaction channels, including the compound elastic scattering cross-sections. The cross-sections were all symmetric about 90^{o}. Spin orbit forces were not taken into consideration in the programme.

The program had the option for the correction of the Hauser-Feshbach cross-sections because of the fluctuations of the widths of the compound levels. The fluctuations arises due to the fact that the assumption of the independence of the formation and decay of the compound nucleus is not accurate enough [La57].

B.9 DWBA program:

This program was the University of Colorado version of the program DWAKE. The program was adopted to run on the Harwell IBM 360/75 machine for our purpose. The DWBA formalism and other aspects of DWBA

calculations have already been discussed in Chapter II. We describe here only the characteristics of the program.

The program could be used DWBA calculations of cross-sections for any single nucleon transfer reaction either stripping or pickup and as well as inelastic scattering.

The potentials in all the channels (i.e. the in going, the out going and the bound) could be built up by super position so that a mixture of shapes could be used if necessary. The form factor options available were Saxon-Wood, Saxon-Wood derivative and Saxon-Wood second derivative.

There were options available for using spin orbit potential in all the channels. There were also provision for using finite range interaction and non-local potentials.

A maximum of 51 partial waves could be included in the calculations and several angular momentum transfers could be calculated in a single occasion.

Intermediate steps in the calculations such as bound state form factors, elastic scattering amplitude (cross-sections) etc. could be printed out for checking purpose. The cross-sections calculated by the program were in Fermi squared. The definition of the cross-section calculated by the program (referred to as $\sigma_{DW}(\theta)$ below) were related to actual cross-sections by the following relations for the reactions reported in this work.

Reaction	$\frac{d\sigma}{d\Omega}(\theta)(fm^2)$
(d,n)	$1.53\left[\frac{2J_f+1}{2J_i+1}\right] S\left[\frac{2s+1}{2} \quad \frac{\sigma_{DW}(\theta)}{2J+1}\right]$
(^{3}He,d)	$4.42\left[\frac{2J_f+1}{2J_i+1}\right] S\left[\frac{2s+1}{2} \quad \frac{\sigma_{DW}(\theta)}{2J+1}\right]$
(d,^{3}He)	$2.95 \quad S\left[\frac{2s+1}{2} \quad \frac{\sigma_{DW}(\theta)}{2J+1}\right]$

where

s = spin angular momentum of the transferred particle used in the calculation

J = Total angular momentum of transferred particle used in the calculation

S = Spectroscopic factor

J_i = Target spin

J_f = Spin of the residual nucleus.

The normalization of 4.42 by Bassel [Ba66] have been used in the above relations for (d,^{3}He) and (^{3}He,d) reactions.

BIBLIOGRAPHY

[Ab66] A.Y. Abul-Magd and M. El-Nadi, Prog. Th. Phys. 35(1966) 798.

[Ad67] J.M. Adams, Thesis, Manchester Univ., 1967.

[Ad69] J.M. Adams, Private Communications.

[Al60] E. Almqvist et al, Nucl. Phys. 19(1960) 1.

[Al68] D.L. Allan et al, AERE, report R.5897 (1968).

[An67] G. Anderson-Lindstrom, Bull. Am. Phys. Soc. 12(1967) 461. and Pittsburg University report, 1967.

[Ar66] D.D. Armstrong and A.G. Blair, Phys. Rev. 140(1966) B1226.

[As68] R.J. Ascuitto et al. Phys. Rev. 176 (1968), 1323.

[Ba62] E.E. Baart et al., Proc. Phys. Soc. 79 (1962) 237.

[Ba66] R.H. Bassel, Phys. Rev. 149 (1966) 791.

[Bj64] J.H. Bjerregaard et al. Phys. Rev. 136 (1964)B1348.

[Bl65] L.M. Blau et al. Nucl. Phys. 76 (1965) 45.

[Bo67] M.C. Bouten et al. Nucl. Phys. A97 (1967) 113.

[Br65] C.P. Browne and W.W. Buechner, Rev. Sc. Instr. 27 (1956) 899.

[Ch66] B.E. Chi, Nucl. Phys. 83 (1966) 97.

[Ch69] R. Chapman, Private Communications.

[Co66] A.A. Cowley et al., Nucl. Phys. 86 (1966) 363.

[Cr65] G.M. Crawley and G.T. Garvey, Phys. Lett 19(1965) 228.

[Cu62] B. Cujec, Phys. Rev. 128(1962) 2303.

[Cu64] B. Cujec, Phys. Rev. 136B (1964) 1305

[Da68] T. Daniels et al. Nucl. Phys. A110 (1968) 339.

[Dh67] D. Dehnhard and C. Mayer-Boricke, Nucl. Phys. 97 (1967) 164.

[Di65] J.K. Dickens and F.G. Perey, Phys. Rev. 138 (1965)B1080, B1083.

[Do67] W.E. Dorenbuch et al. Nucl. Phys. A102, (1967) 681.

[El65] M. El-Nadi et al. Nucl. Phys. 65 (1965) 90.

[En58] P.M. Endt and C.H. Paris, Phys. Rev. 110 (1958) 89

[En63] H.A. Enge and W.W. Buechner, Rev. Sci. Instr. 34 (1963) 155.

[En67] P.M. Endt and C. van der Leun, Nucl. Phys. A105 (1967) 1.

[Er66] J.R. Erskine et al. Phys. Rev. 142 (1966), 633.

[Fi67] P.S. Fisher, and D.K. Scott, Nucl. Instr. Meth. 49 (1967) 301.

[Fr60] J.B. French and M.H. MacFarlane, Rev. Mod. Phys. 32 (1960) 567.

[Ga62] A. Garcia et al. Nucl. Phys. 38 (1962) 372.

[Gi67] V. Gillet and E.A. Sanderson, Nucl. Phys. A54 (1964) 472.

[Go60] H.E. Gove, Proc. Int. Conf. Nucl. Struct., Kingston (1960) 438.

[Gl61] R.N. Glover and E. Weigold, Nucl. Phys. 24 (1961) 630.

[Gl64] P.W.M. Glaudman et al. Nucl. Phys. 56 (1964), 529, 548.

[Gl65] R.N. Glover et al. Phys. Lett. 19(1965) 493.

[Go64] F.S. Goulding, Nucl. Instr. Meth. 31 (1964) 1.

[Go68] H.E. Gove, Paper Gordon Conf. Nucl. Struct., Tilton, New Hampshire, (1968), UR-NSRL-7.

[Gr64] H.D. Garber, Thesis, Kansas Univ. (1964) (quoted in We68).

[Ha52] W. Hauser and H. Feshbach, Phys. Rev. 87 (1952) 366.

[Ha64] E.C. Halbert, Nucl. Phys. 50 (1964) 353.

[Ha66a] G.I. Harris et al., Bull. Am. Phys. Soc. 11 (1966) 65.

[Ha66b] G.I. Harris et al., Bull. Am. Phys. Soc. 11 (1966) 65.

[Ha67] J.C. Hafele et al. Phys. Rev. 155 (1967) 1238.

[Ha67a] G.I. Harris et al. Phys. Rev. 157 (1967) 958.

[Ha68] O. Hansen et al. Nucl. Phys. A118 (1968) 41.

[Ha68a] O. Hausser et al. Can. J. Phys. 46 (1968) 2809.

[Hi59] S. Hinds and R. Middleton, Proc. Phys. Soc. 73 (1968) 547.

[Hi67] J.C. Hiebert et al Phys. Rev. 154 (1967) 898.

[Ho63] P. Horvat et al., Nucl. Phys. 45 (1963) 341.

[Ho66] P.E. Hodgson, Adv. Phys. 15 (1966) 329.

[Ho67] A.J. Howard et al. Phys. Rev. 139,(1965) B1135.

[Ho68] P.E. Hodgson, Adv. Phys. 17 (1968) 563.

[Ig59] G. Igo et al., Phys. Rev. 115 (1959) 1665.

[Il62] K. Illakovac et al. Phys. Rev. 128 (1962) 2739.

[Ke64] I. Kelson and C. Levinson, Phys. Rev. 134 (1964) B269.

[La57] A.M. Lane et al. Proc. Phys. Soc. A70 (1957) 557.

[La62] A.M. Lane, Nucl. Phys. 35 (1962) 676.

[Li69] T.K. Lim, Nucl. Phys. A129 (1969) 259.

[Ma52] C.E. Mandeville, et al. Phys. Rev. 85 (1952) 193.

[Ma68] J.B. Marion and F.C. Young, Nuclear Reaction Analysis, North Holland, 1968.

[Ma69] G. Mairle et al. Nucl. Phys. A134 (1969) 180.

[Mo63] R.A. Moore- Thesis, Univ. of Kansas (quoted in Ve69).

[Ne62] D.R. Neher, et al., Nucl. Phys. 31 (1963) 231.

[Ni55] S.G. Nilsson, Dan. Mat. Phys. Medd., 29 (1955) No.16.

[Ow67] R.B. Owen and M.L. Awcock, AERE report R.5393 (1967).

[Pe62] F. Perey and B. Buck, Nucl. Phys. 32 (1962) 353.

[Pe63] C.M. Perey and F.G. Perey, Phys. Rev. 132 (1963) 755.

[Pe63a] E. Pelliegrini and W.S. Wiktor, Nucl. Phys 40 (1963) 412.

[Pe67] G.A. Pettit et al. Nucl. Phys. 79 (1967) 231.

[Pi65] W.T. Pinkston and G.R. Satchler, Nucl. Phys. 72 (1965) 641.

[Pi66] J. Picard and A.G. De Pinho, Nuovo Cim. 41 (1966) 239.

[Po65] M.J.D. Powell, Computer Journal 7(1965) 1965.

[Pr68] A. Prakash, Phys. Lett., 20 No.10 (1968) 864.

[Pr69] A. Prakash and N. Austern, Ann. Phys. 51, (1969) 418.

[Pu69] N.G. Puttaswamy and J.L. Yntema, Phys. Rev. 177 (1969) 1624.

[Ro65] J.R. Rook, Nucl. Phys. 61 (1965) 219.

[Ro67] J.R. Rook, Nucl. Phys. A97 (1967) 217.

[Ro67a] B. Rosener et al. Phys. Rev. 154 (1967) 1080.

[Ry63] J. Rynal, Phys. Lett. 7(1964) 281.

[Sa58] G.R. Satchler, Ann. Phys. 3(1958) 275.

[Sa64] G.R. Satchler, Nucl. Phys. 55 (1964) 1.

[Sa65] G.R. Satchler, Private communication (quoted in Ho66).

[Sh52] W. Shockley, Proc. IRE. 40 (1952) 1365.

[Sh64] R. Sheer et al. Phys. Rev. Lett. 12 (1964) 420.

[Si66] R.H. Siemssen et al. Phys. Rev. Lett 16 No.23 (1966) 1050.

[St67] R.N. Stover, Nucl. Phys. A92 (1967) 209.

[Ta66] P. Taras, Can. J. Phys. 44(1966) 1563.

[Ta68] T. Tamura, Phys. Rev. 165 (1968) 1123.

[Te65] J.W. Tepel, Nucl. Instr. Meth. 40 (1966) 100.

[Te66] S.N. Tewari and M.J. Banarjee, Nucl. Phys. 82 (1966) 337.

[Th70] W.J. Thompson and W.R. Hering, Phys. Rev. Lett. 24 No.6 (1970) 272.

[Va58] C. Van der Leun and P.M. Endt, Phys. Rev. 110 (1958) 96.

[Ve69] C.W. Vernett, Univ. Alberta, report, 1969.

[Wa69] G.J. Wagner et al. Nucl. Phys. A125 (1969) 80.

[We68] A. Weidinger et al. Nucl. Phys. A108 (1968) 547.

[Wi66] D. Wilmore, A.E.R.E. Report, R.5053, 1966.

[Wi67] B.H. Wildenthal et al. Bull. Am. Phys. Soc. 11 (1967) 48.

[Wi68] B.H. Wildenthal and E. Newman, Phys. Rev. 175 (1968) 1431.

[Wi68b] B.H. Wildenthal et al. Phys. Lett. 26B (1968) 692.

[Wi69] D. Wilmore, Private communications.

[Yn63] J.L. Yntema, Phys. Rev. 131 (1963) 811.

[Yn64] J.L. Yntema and G.R. Satchler, Phys. Rev. 134 (1964) B976.

[Zh69] R.W. Zurmuhle, Private communications (quoted in Ho68).